uOttawa

L'Université canadienne
Canada's university

FACULTÉ DES ÉTUDES SUPÉRIEURES ET POSTOCTORALES

uOttawa

L'Université canadienne
Canada's university

FACULTY OF GRADUATE AND POSDOCTORAL STUDIES

Micheal E. Reimer
AUTEUR DE LA THÈSE / AUTHOR OF THESIS

Ph.D. (Physics)
GRADE / DEGREE

Department of Physics
FACULTÉ, ÉCOLE, DÉPARTEMENT / FACULTY, SCHOOL, DEPARTMENT

Electrostatic Gating of Deterministically Positioned InAs/InP Quantum Dots
TITRE DE LA THÈSE / TITLE OF THESIS

Robin Williams
DIRECTEUR (DIRECTRICE) DE LA THÈSE / THESIS SUPERVISOR

CO-DIRECTEUR (CO-DIRECTRICE) DE LA THÈSE / THESIS CO-SUPERVISOR

Paul Finnie

Boguslaw Jarosz

Athos Petrou (SUNY Buffalo)

Nikolay Shtinkov

Gary W. Slater
Le Doyen de la Faculté des études supérieures et postdoctorales / Dean of the Faculty of Graduate and Postdoctoral Studies

Electrostatic Gating of Deterministically Positioned InAs/InP Quantum Dots

Michael E. Reimer

Thesis Submitted to the
Faculty of Graduate and Postdoctoral Studies
In partial fulfillment of requirements
For the Doctor of Philosophy degree in Physics

Department of Physics
Faculty of Sciences
University of Ottawa

Your file Votre référence
ISBN: 978-0-494-65573-3
Our file Notre référence
ISBN: 978-0-494-65573-3

I dedicate this thesis to my lovely wife, Elissa Hines Reimer, who encouraged the successful completion of this thesis.

"Most people say that is it is the intellect which makes a great scientist. They are wrong: it is character."

– Albert Einstein

Table of Contents

List of Figures

Abstract

Recent advances in nanofabrication technology have made it possible to develop novel quantum opto-electronic devices at the nanometre scale. This thesis demonstrates the ability to precisely position electrostatic gates around the periphery of a deterministically positioned semiconductor quantum dot. This work also demonstrates the first published results of InAs/InP quantum dots subject to electric fields. The InAs/InP material system is particularly attractive for fiber-based quantum cryptography since the ground-state transition can be tuned to the telecommunications wavelength of 1.55 μm. Together, this approach and material system offers a fully scalable route to sources of single photon and entangled photon pairs at telecom wavelengths or arrays of initialized single spins for applications in quantum information science.

This thesis presents a detailed study of the electronic and optical properties resulting from electrostatic gating of an individual InAs quantum dot embedded in an InP nanotemplate. The unique device geometry studied here is unprecedented and allows the application of a vertical and an in-plane lateral electric field on the same quantum dot. The results show that application of a vertical electric field along the growth direction precisely controls the charge state or number of electrostatically induced electrons. Important information on the dot morphology is obtained, implying that the InAs dot composition is uniform. In contrast, application of an in-plane lateral electric field across a single quantum dot is shown to strongly modify electron-hole wavefunction overlaps and Coulomb interactions of single excitons and biexcitons while allowing a new optically forbidden transition to appear at finite field involving an s-shell electron and p-shell hole.

Of particular significance to the scientific community is the finding that application of the lateral electric field resulted in a crossing of the exciton and biexciton optical transitions, and thus removal of the biexciton binding energy. Theoretical calculations are presented demonstrating that removal of the biexciton binding energy leads to the generation of entangled photon pairs without the need to enforce degeneracy of the two intermediate, single exciton states in the biexciton-exciton radiative cascade. The nanotemplate dimensions are also shown to directly control the biexciton binding energy. A new regime of the biexciton binding energy is studied in larger dots, demonstrating the possibility of entangled photon generation through an 'unbound' biexciton state without the requirement of post-growth tuning.

Statement of Originality

This thesis presents an original study of the optical and electronic properties of a single InAs/InP quantum dot subject to vertical and lateral electric fields. I performed optical spectroscopy for all the single, gated quantum dots as a function of electric field. I built the electric field setup and programmed the Labview software to facilitate the electric field measurements. In addition, I carried out all of the analysis that pertains to the obtained optical spectra including comparison to theory. I performed and analyzed the electrostatic modeling for the gated pyramids in order to estimate the feasibility of my project and to understand the voltages required in experiment for such a complex geometry.

The growth of the single quantum dots in ridge and pyramidal nanotemplates was done by Dr. Philip Poole and Dr. Dan Dalacu in the group of Dr. Robin L. Williams at the Institute for Microstructural Sciences, National Research Council (IMS-NRC). In collaboration with Dr. Jean Lapointe and Dr. Dan Dalacu at the IMS-NRC, a process was developed in this thesis to precisely position electrostatic gates around an InAs quantum dot embedded in an InP nanotemplate. I was responsible for designing the layout of the gated dots and preparing some of the samples for e-beam lithography and evaporation.

All of the theoretical calculations in Chapter 5 for a single quantum dot in a lateral electric field were carried out by Dr. Marek Korkusiński from the Quantum Theory Group at the IMS-NRC. These calculations were performed to understand the effects of the applied lateral electric field across a single quantum dot and observed crossing of the exciton and biexciton transitions.

List of Publications

1. M. E. Reimer, W. R. McKinnon, J. Lapointe, D. Dalacu, P. J. Poole, G. C. Aers, D. Kim, M. Korkusiński, P. Hawrylak, and R. L. Williams. Towards scalable gated quantum dots for quantum information applications. *Physica E (Amsterdam)* **40**, 1790-1793 (2008).

2. M. E. Reimer, M. Korkusiński, D. Dalacu, J. Lefebvre, J. Lapointe, P. J. Poole, G. C. Aers, W. R. McKinnon, P. Hawrylak, and R. L. Williams. Prepositioned single quantum dot in a lateral electric field. *Phys. Rev. B* **78**, 195301 (2008).

3. M. E. Reimer, D. Dalacu, J. Lapointe, P. J. Poole, D. Kim, G. C. Aers, W. R. McKinnon, and R. L. Williams. Single electron charging in deterministically positioned InAs/InP quantum dots. *Appl. Phys. Lett.* **94**, 011108 (2009).

4. M. E. Reimer, D. Dalacu, J. Lapointe, P. J. Poole, W. R. McKinnon, and R. L. Williams. Non-inverted electron-hole alignment in InAs/InP self-assembled quantum dots. *Phys. Status Solidi B* **246**, 828-831 (2009).

5. M. E. Reimer, D. Dalacu, P. J. Poole, and R. L. Williams. Biexciton binding energy control in site-selected quantum dots. *J. Phys. Conf. Ser.*, Accepted for publication (2009).

6. M. E. Reimer, M. Korkusiński, J. Lefebvre, J. Lapointe, P. J. Poole, G. C. Aers, D. Dalacu, W. R. McKinnon, S. Frédérick, P. Hawrylak, and R. L. Williams.

Voltage induced hidden symmetry and photon entanglement generation in a single, site-selected quantum dot. Submitted to Phys. Rev. Lett., arXiv:0706.1075 (unpublished).

7. P. J. Poole, D. Dalacu, M. E. Reimer, S. Frédérick, R. L. Williams, G. C. Aers, M. Korkusiński, P. Hawrylak, and J. Lapointe. Placing single quantum dots in InP photonic crystal microcavities - A route to single and entangled photon pair sources. *Proc. IEEE*, Indium Phosphide and Related Materials, 2008. IPRM 2008. 20th International Conference on, Page(s): 1-6 (2008). doi: 10.1109/ICIPRM.2008.4703048.

8. D. Kim, J. Lefebvre, J. Lapointe, M. E. Reimer, J. Mckee, P. J. Poole, and R. L. Williams. Optical spectroscopy of single, planar, self-assembled InAs/InP quantum dots. *Phys. Status Solidi C* **3**, 3840-3843 (2006).

9. M. Korkusiński, M. E. Reimer, R. L. Williams, and P. Hawrylak. Engineering photon cascades from multiexciton complexes in a self-assembled quantum dot by a lateral electric field. *Phys. Rev. B* **79**, 035309 (2009).

10. D. Dalacu, M. E. Reimer, S. Frédérick, D. Kim, J. Lapointe, P. J. Poole, G. C. Aers, R. L. Williams, W. R. McKinnon, M. Korkusiński, and P. Hawrylak. Directed self-assembly of single quantum dots for telecommunication wavelength optical devices. *Laser Photonics Rev.*, 1-17 (2009). doi: 10.1002/lpor.200810077.

11. D. Kim, W. Sheng, P. J. Poole, D. Dalacu, J. Lefebvre, J. Lapointe, M. E. Reimer, G. C. Aers, and R. L. Williams. Tuning the exciton g factor in single InAs/InP quantum dots. *Phys. Rev. B* **79**, 045310 (2009).

Acknowledgements

I would like to acknowledge the contributions and assistance of the following individuals: Geof C. Aers, Guy Austing, Dan Dalacu, Simon Frédérick, Louis Gaudreau, Pawel Hawrylak, Danny Kim, Marek Korkusiński, Jean Lapointe, Jacques Lefebvre, Joe McKee, W. Ross McKinnon, Philip J. Poole, Andy Sachradja, Sergei Studenikin, Robin L. Williams, and Peter Zawadzki.

Special thanks goes to my supervisor Robin L. Williams for giving me the opportunity to perform leading-edge research in his lab and always being available to discuss exciting new results. I would also like to thank my wife, family and friends for all of their encouragement and support. Finally, I would like to thank my 'lunchmates' and all of my fellow students down in the 'dungeon' at the NRC for their companionship and stimulating and often amusing conversations.

Chapter 1

Overview

The discrete energy level structure and capacity to spatially isolate individual electrons and holes of semiconductor self-assembled quantum dots makes them a promising candidate for the basic element within quantum information processing systems [1]. Quantum dots can be embedded within the active area of a device, allowing precise control of the numbers of both electrons and holes [2–10], such that coherent spin manipulation can be performed [11–15]. In addition to coherent control of the spin state, the electronic coupling between individual dots can be manipulated [16–22] and the exciton-photon interaction can be tuned for single photon or entangled photon emission applications, making the long distance transfer of quantum information a possibility [23, 24]. Since the aforementioned experiments were based on randomly grown self-assembled quantum dots, the device architecture was not scalable. To bring such experiments closer to large scale implementation, it is necessary to develop routine ways to control the nucleation site of individual dots and embed them within active devices.

This thesis addresses this issue of scalability by developing a process to electrically contact a single, deterministically positioned InAs quantum dot, where the nucleation

site is controlled directly by a nano-scale InP template (nanotemplate). To the best of my knowledge, this work is the first to electrostatically gate such a deterministically positioned quantum dot. This work resulted in several publications in high quality journals and can be found in Refs. [8–10,25–28], to be described in more detail throughout this thesis. The experimental results and electrostatic gating simulations presented in this thesis are my own. The theoretical calculations in Chapter 5 for a single quantum dot in a lateral electric field was carried out by Dr. Marek Korkusiński from the Quantum Theory Group at the Institute for Microstructural Sciences, National Research Council. Theoretical calculations were performed to understand the effects of the applied lateral electric field across a single quantum dot and observed crossing of the exciton and biexciton transitions, making the generation of entangled photon pairs a possibility [25, 27].

Prior to the start of this work, the group of Dr. Robin L. Williams at the Institute for Microstructural Sciences, National Research Council, developed a unique preparation strategy to achieve the necessary control through a nanotemplate deposition technique where the nucleation site of individual InAs quantum dots embedded in an InP nanotemplate can be precisely controlled [29, 30]. In contrast to the work of other groups [31–39], this technique provides an atomically smooth surface available for quantum dot growth without affecting its optical quality [25, 40]. The benefit of knowing the quantum dot location with nanometres of precision is that electrostatic gates or photonic crystals can be precisely constructed around them [8]. In collaboration with Dr. Jean Lapointe and Dr. Dan Dalacu at the Institute for Microstructural Sciences, National Research Council, a process was developed in this thesis to precisely position electrostatic gates around an InAs quantum dot embedded in the InP

nanotemplate. The ability to functionalize a single quantum dot in this way provides a scalable route to sources of single photons and entangled photon pairs. The InAs/InP dots grown for this thesis have the added benefit of being tunable to the telecommunications band around 1.55 μm making them excellent candidates for fibre based quantum information processing [41].

Since these InAs dots embedded in an InP nanotemplate are the first of its kind, this thesis presents a detailed study of the electronic and optical properties of a deterministically positioned, gated, single quantum dot as a function of an applied electric field along the growth and in-plane directions of the quantum dot. A vertical electric field (growth direction) is shown to precisely control the number of electrostatically induced electrons. In contrast, an in-plane lateral electric field exhibits stronger control of the electron-hole wavefunctions and Coulomb interactions and introduces a new optical transition that appears at finite bias, which involves an s-shell electron and p-shell hole. The strong modification of Coulomb interactions of the confined exciton and biexciton results in their degeneracy and thus removal of the biexciton binding energy. Of particular significance resulting from this work is a new proposal for the generation of entangled photon pairs that circumvents the major problem in existing devices which the scientific community has been struggling to overcome – the need to remove the intermediate exciton states in the biexciton-exciton radiative cascade [42–51]. Instead, the proposal discussed in this thesis relies on the removal of the biexciton binding energy and degeneracy of the cross colour transitions in the cascade and is possible by simply tuning a voltage without resorting to large external magnetic fields [44], spectral filtering [45], quantum dot size and composition engineering through various growth techiques [43,46,51], or application of in-plane electric

fields [42, 47–49] in which oscillator strengths of the optical transitions involved are significantly diminished, making the entangled photon source very inefficient. Additionally, these efforts have been limited to only randomly located quantum dots, a constraint which is addressed in this thesis.

In addition to the pyramidal nanotemplate geometry providing an atomically smooth facet available for dot growth, the side-facets also allow integration of four top Schottky gates that can be precisely positioned around the single quantum dot. This unique device geometry promises the ability to apply a lateral electric field in any crystal orientation, which may be an important step in the next generation of devices for entangled photon pair generation. By adding a doped back contact to the same device, I show single electron charging experiments on the same quantum dot. In the past few years, electron number control has been shown to be an important step for quantum information applications in which complete quantum control is required [11–15] to be discussed in more detail in the introduction of Chapter 8.

Since the gated pyramidal nanotemplate device geometry containing a single quantum dot is very complex (4 top gates and 1 back gate) and different than that studied in literature, two- and three-dimensional calculations of the electrostatics is investigated. The results of these calculations provide analytical data regarding the charging mechanism for precise single electron control and the voltages required on each gate for applied electric fields in any in-plane field direction on the same quantum dot. The ability to apply an in-plane field in any crystal orientation is shown to be an important step for entangled photon generation. Moreover, the results show that a built-in electric field is produced due to small misalignments of the top four Schottky gates with respect to the prepositioned quantum dot (a common situation which

occurs in practice due to the resolution of the e-beam writer $\sim 30\,\text{nm}$).

1.1 Organization of thesis

Each chapter begins with a detailed introduction, including an overview of the current literature and how the research in this thesis attempts to overcome current scientific problems in the field of quantum information science. Specifically for the experimental chapters, the introduction is followed by details of the device, presentation of main results and discussion, and ending with main conclusions. The only exceptions to this basic format is Chapter 2, which presents a basic overview of quantum dots and provides a scientific foundation for the results presented in this thesis aimed at new scientists in the field.

This thesis is organized into chapters as follows. In Chapter 2, the fundamental electronic and optical properties of self-assembled quantum dots are presented. Optical selection rules are introduced for single quantum dots, which are shown to have analogies in atomic physics. Here, many people draw conclusions and call quantum dots 'artificial atoms', although some significant differences are briefly discussed. The idea of few particle interactions is also introduced which directly influences the recombination energy of the exciton observed in experiment due to Coulomb interactions and many-body effects. Additionally, the two-dimensional harmonic oscillator is described, which is used to approximate the quantum dots in-plane confinement potential for the theoretical calculations presented in Chapter 5. In Chapter 3, the most common growth method used for self-assembled dots is described (Stranski-Krastanow growth mode). The Stranski-Krastanow growth mode is utilized for directed self-assembled growth to precisely position the InAs quantum dot at the apex

of an InP nanotemplate by directing the dot material to known locations on the substrate. Thus, by appropriate control of the growth conditions, the top apex dimensions control the quantum dot lateral dot dimensions, while the amount of dot material supplied controls the dot height and therefore the emission energy. In this way, the dot emission can be controlled towards the telecommunications wavelength band around $1.55\,\mu m$. Additionally, the method of reaching the single dot regime and selecting single dots for electrostatic gating is described for the two types of device structures studied in this thesis: 1) gated ridges of 'stripe' geometry and 2) gated pyramids containing four Schottky gates around the periphery of the quantum dot and a doped back gate for single charging experiments. In Chapter 4, the experimental methodology is described.

Theoretical calculations are presented in Chapter 5 and are used to understand the effects of the applied lateral electric field for single dots on ridge nanotemplates to be presented in Chapter 6 and Chapter 7. The model described here utilizes an in-plane 2D parabolic potential to describe the quantum dot's confinement potential. The results of the calculations, which include Coulomb interactions and many-body effects, qualitatively explain the observed experimental results for an in-plane lateral electric field. Of particular significance is the finding that the exciton transition redshifts and the biexciton blueshifts as a function of lateral electric field. At a critical value of the electric field, the biexciton binding energy is removed and thus entangled photon pairs are generated.

In Chapter 7, the current method for generating entangled photon pairs is presented that utilizes the biexciton-exciton-vacuum radiative cascade in semiconductor

quantum dots. Next, a new proposed scheme is introduced that circumvents the major problem in existing devices; that is, enforcing the degeneracy of the intermediate exciton states. Instead, the new proposal relies on the removal of the biexciton binding energy which is demonstrated experimentally. Alternatively, the biexciton binding energy is shown to be controllably tuned via the ridge nanotemplate. For dots exhibiting an unbound biexciton state, it is suggested that entangled photon pairs are possible without post-manipulation. This regime to obtain an unbound biexciton for large dots was not possible until this work. The mechanisms to obtain unbound biexcitons for large dots such as piezoelectric fields is discussed, which lead to the removal of the fine-structure splitting of the intermediate states in the biexciton-exciton radiative cascade and therefore generation of entangled photon pairs.

In Chapter 8, a deterministically positioned InAs quantum dot is presented on an InP pyramidal nanotemplate which demonstrates single electron charging and the possibility of generating entangled photon pairs on the same quantum dot. Two-dimensional and three-dimensional calculations for solutions of the Poisson equation are also presented, which explain the current charging mechanism in this device since the InP pyramidal nanotemplate device geometry is unique and not planar as the single electron charging devices cited in literature. Moreover, the three dimensional calculations show that it is also possible to use metal-oxide-semiconductor devices for charging experiments. Counter-intuitively, single electron charging is shown to be more efficient for the metal-oxide-semiconductor device presented in this thesis compared to the metal-semiconductor devices. Finally, in Chapter 9, the main conclusions are summarized along with a brief discussion of future work.

Chapter 2

Fundamental properties of quantum dots

The density of electronic states of semiconductor nanostructures can be altered in useful ways by introducing one, two, or three directions of quantization. This quantization is achieved by fabricating quantum well (2-dimensional), quantum wire (1-dimensional), or quantum dot (0-dimensional) heterostructures that are nanometer in size [52]. Semiconductor quantum dots are very attractive 0-dimensional systems due to their δ-function (discrete like) density of states, which allow the motion of electrons and holes to be quantized in all three spatial directions. Due to this quantization, the energy levels in a quantum dot form a discrete energy spectrum with well separated "shells", making them very attractive for optoelectronic devices and quantum information science applications [1]. This appeal arises in semiconductor quantum dots since their optical and electronic properties can be modified in a controlled manner either by growth conditions, or external perturbations such as an electric field as demonstrated in this thesis.

Since quantum dots exhibit well separated "shells", they are often referred to as artificial atoms [1]. Such analogies between quantum dots and atoms are often made;

however, there are several fundamental differences between them. First, quantum dots are composed of thousands of atoms instead of only one. This leads to a much smaller energy level spacing for quantum dots compared to that of atoms. The energy level spacing for quantum dots is on the order of meV, whereas the energy level spacing for atoms is on the order of eV. Second, the confining potential produced by the positive potential of the nucleus for an atom only confines electrons, whereas a semiconductor quantum dot has the ability to confine both electrons and holes. Third, the lateral confining potential of a quantum dot is weaker in the lateral direction as compared to the vertical growth direction and in most cases can be approximated by a two-dimensional (2D) parabolic potential. This is in contrast to the Coulomb potential produced by atoms which possesses a singularity at the nucleus. Fourth, the number of electrons (total confined charge) in a quantum dot can be precisely controlled by a vertical electric field applied along the growth direction advantageous for applications in quantum information science [2,5–9]. In contrast, the confinement potential produced in atoms by the nucleus is fixed and more difficult to manipulate; however, experimental schemes still exist to achieve long-distance quantum communication [53–57]. Finally, a single quantum dot is embedded in a host semiconductor matrix which is very stable for device applications, whereas atoms stored in a dipole trap have been reported to escape after about ten seconds [56].

The remainder of this chapter introduces the basic electronic and optical properties of semiconductor quantum dots. The fundamental quantum dot properties presented here are crucial in understanding the optoelectronic properties of single, gated quantum dots studied later in this thesis. For a more detailed introduction to

quantum dots, the following books are recommended: "Single Quantum Dots: Fundamentals, Application and New Concepts", edited by P. Michler [1], and "Quantum Dot Heterostructures", by D. Bimberg *et al.* [52].

This chapter is organized as follows: In Section 2.1, quantum effects resulting from the three-dimensional confinement potential of a single quantum dot is described. In Section 2.2, the two-dimensional harmonic oscillator is introduced in order to approximate the much weaker lateral confinement potential of the quantum dot compared to that of the vertical growth direction. This lateral confinement potential is used in this thesis to model a single quantum dot in a lateral electric field. In Section 2.3, the optical selection rules of a single quantum dot is provided at zero electric field. Finally, in Section 2.4, few particle states in single quantum dots are introduced, which directly influences the recombination energy of single excitonic states following their optical selection rules.

2.1 Three-dimensional confinement

Typical dimensions of a quantum dot range from a few to tens of nanometres. At this length scale, the effects of quantum confinement become important since the wavefunction of a confined electron or hole has similar dimensions to that of the quantum dot confining potential. Therefore, to calculate the electronic properties of the quantum dot, these quantum effects should be taken into consideration. As an example, by considering the crystal momentum, the length scale at which quantum confinement effects are important can be estimated by the Heisenberg uncertainty relation, $\Delta x \Delta p \sim \hbar$, where Δx and Δp are the uncertainties in length and momentum, respectively. By using the energy dispersion relation in terms of wavevector, k, for an

electron in an isotropic, parabolic band ($E(k) = \hbar^2 k^2/2m^*$), the crystal momentum ($p = \hbar k$) is $p = \sqrt{2m^*E}$, and Δx becomes $\Delta x \approx \hbar/\sqrt{2m^*E}$. By substituting typical values for the conduction band electrons into this equation ($m^* \sim 0.1m_0, E = k_BT = 25\,\text{meV}$), a length scale Δx of 4 nm is obtained at room temperature. Here, k_B is Boltzmann's constant, T is the temperature, and m_0 is the mass of the free electron. At room temperature, quantum confinement effects should start to become important on the nanometer scale. Thus, it is expected that decreasing the temperature results in an increased length scale to observe quantum effects (hundreds of nanometres).

The bandgap engineering required to trap both electrons and holes simultaneously for optoelectronic applications can be met by fabricating self-assembled quantum dots. Self-assembled quantum dots can be fabricated by a strain driven epitaxial growth technique of III-V semiconductor materials [1] as described in Chapter 3.1. The three-dimensional (3D) confining potential of a self-assembled quantum dot is produced by surrounding the dot material with a higher bandgap semiconductor, as shown schematically in Figure 2.1(a). For example, by embedding InAs ($E_g = 0.36\,\text{eV}$) within InP ($E_g = 1.27\,\text{eV}$), where E_g is the energy gap of the semiconductor at 300 K [58], a potential well is produced for the InAs/InP heterointerface. The energy band diagram profile for the InAs/InP heterointerface is shown schematically in Figure 2.1(b) for one of the crystal directions of the "quantum box" from 2.1(a) (*i.e.*, growth direction). Here, the wider bandgap material (InP) completely encloses the narrower bandgap material (InAs), which traps both electrons and holes in 3D. It should be noted that the valence band (VB) potential for holes is much more complicated than the one shown here and is discussed in more detail in Section 2.3: Optical selection rules for single quantum dots.

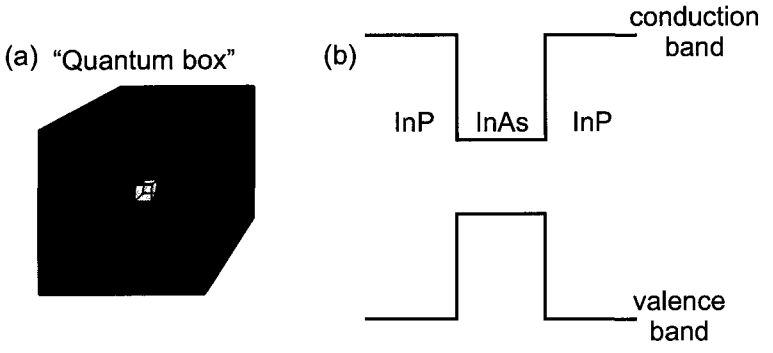

Figure 2.1: (a) Quantum box representation of single quantum dot. (b) Energy band diagram of InAs/InP heterointerface for one of the crystal directions of the "quantum box" in (a). The smaller bandgap of InAs localizes electrons and holes for 3D confinement.

2.1.1 Band offsets and alignment

The energy difference in the bandgap, E_g, of the two materials is not the only important parameter in forming a 3D confinement potential of the quantum dot. The band alignment and band offsets of the conduction and valence band edges of the two semiconductor materials of the heterointerface determines which layer the electrons and holes are confined, as well the strength of the confinement for each particle. If the narrower bandgap material is completely enclosed by the wider bandgap material as in the case of the InAs/InP heterointerface, then both electrons and holes will be trapped in the narrow bandgap InAs layer. This type of alignment for the band offset is called type-I alignment.

The band offsets and alignment are determined by the electron affinity, χ, of the two semiconductor materials, and their alignment with respect to the vacuum level. The electron affinity, characteristic of a material, is defined as the energy required to take an electron from the bottom of the conduction band to the vacuum level where it can escape from the crystal. Anderson's rule states that the vacuum level of these

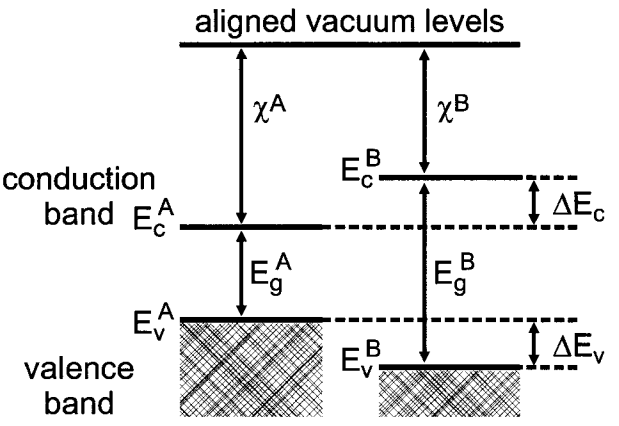

Figure 2.2: Schematic representation of band offsets and alignment of semiconductor heterointerface using Anderson's rule. The two different semiconductor materials are labeled with subscripts A and B, respectively.

two materials should line up on an absolute energy scale [59]. The alignment of the conduction and valence band edges utilizing Anderson's rule is summarized in Figure 2.2. Here, a heterointerface made of two materials labeled A and B, with different energy gaps (*i.e.*, $E_g^A < E_g^B$) are considered. The difference in the corresponding electron affinities, χ_A and χ_B of the two materials corresponds to a band offset for the conduction and valance bands, denoted ΔE_c and ΔE_v, respectively. The convention is that both ΔE_c and ΔE_v are both positive for type-I band alignment. Other examples of type-I band alignment occur in the GaAs/AlGaAs and InAs/GaAs heterointerface.

Different types of band alignments are summarized in Figure 2.3. For type-I alignment, electrons and holes are confined spatially within the same layer (*i.e.*, within the potential well), advantageous for optoelectronic applications. However, for other types of alignment, electrons can be confined in one layer, while holes are confined in another. For example, in the InP/InAlAs heterointerface, the electrons are localized in the InP layer, while holes settle in the InAlAs layer. This type of alignment is known as type-II alignment or staggered band alignment. Finally type-III alignment

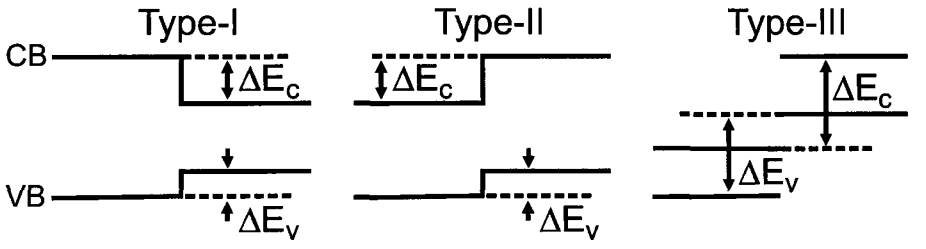

Figure 2.3: Types of band alignment for semiconductor heterointerface. CB: conduction band, VB: valence band. Type I: lower bandgap semiconductor is completely enclosed within larger bandgap semiconductor useful for optoelectronic applications (e.g. InAs/InP, InAs/GaAs). Type II: staggered band alignment (e.g. InP/InAlAs). Type-III: broken band alignment (e.g. InAs/GaSb).

or broken gap alignment occurs when the bandgaps of the heterointerface do not overlap, such as in the InAs/GaSb interface. In this type of broken gap alignment, electrons from the valence band of the InAs flow to the conduction band states of GaSb until a built-in electric field is produced as to oppose this electron flow.

2.1.2 Solutions of three-dimensional confining potential

The electronic properties of a quantum dot are frequently estimated through modeling with a square well confining potential of finite height in three dimensions (3D), also known as a "quantum box". The solutions are obtained by solving the 3D Schrödinger equation. However, it is not possible to solve the Schrödinger equation exactly in real quantum dots since they have more complex geometries than a "quantum box" and are also highly strained. In some cases, there is a compositional profile of the dot material (as in InAs/GaAs self-assembled dots), thus adding to the complexity of the confining potential. In such cases, the Schrödinger equation must be solved by numerical techniques [60, 61].

To simplify the problem of calculating the electronic properties of semiconductor

quantum dots, the effective mass approximation can be utilized. In this approximation, the more complex bandstructure of each constituent layer making up the nanostructure is ignored. Instead, the effective potential that is created by the band edge profile can be described by an effective mass. The effective mass takes into account the semiconductor bandstructure and is different for electrons and holes. This approach essentially describes how electrons and holes move under their band edge profiles as if they were free, but with a different dispersion relation. The free electron mass in the Schrödinger equation can now be replaced by the effective mass and the electrons and holes are treated as "quantum particles". This method makes it possible to apply elementary quantum mechanics and in most cases the one-dimensional (1D) Schrödinger equation can be utilized for calculating the single particle wavefunctions and estimating the single particle energies for carriers moving in the localized potential of the quantum dot. Note that the calculated wavefunction in the effective mass approximation is known as an envelope wavefunction since it does not include the Bloch wavefunction which depends on the periodic potential of the semiconductor lattice. For the effective mass approximation to be valid, the Bloch wavefunctions in the two adjacent materials of the heterointerface must be similar [52].

To illustrate the discrete quantization of energy levels resulting from the 3D confinement potential of quantum dots, an analytic solution for a particle in a box with infinite barrier height is presented. Using a quantum dot with rectangular symmetry and sides of length L_x, L_y, L_z, along the three Cartesian coordinates (x, y, z), the Schrödinger equation is separable and the total energy is the sum of the eigenenergies along each of the three different axes. To determine the eigenenergies along one quantization direction for either the electron or hole, the Schrödinger equation can

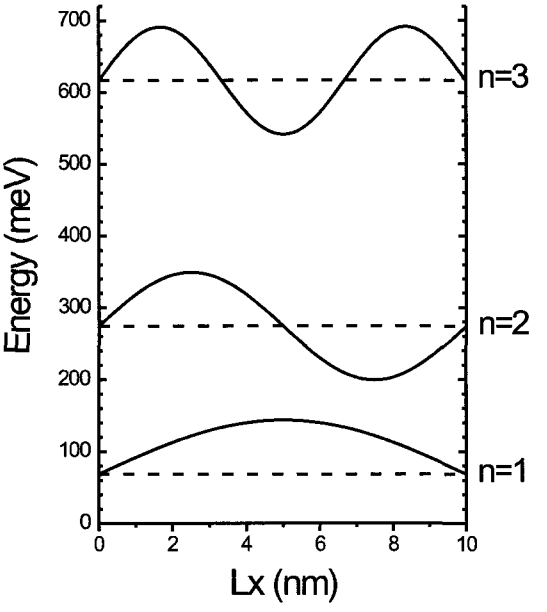

Figure 2.4: Solutions to the 1D Schrödinger equation of the "quantum box" potential along the x-direction of the "quantum box", which exhibits quantized energy levels. For the "quantum box" in Figure 2.1(a), the y- and z- directions are quantized identically to x.

be solved in one-dimension (1D). The time-independent Schrödinger equation in 1D is

$$-\frac{\hbar^2}{2m^*}\frac{\partial^2}{\partial x^2}\psi(x) + V(x)\psi(x) = E_x\psi(x) \tag{2.1}$$

where m^* is the effective mass, $\psi(x)$ is the wavefunction of the confined carrier (electron or hole), $V(x)$ is the potential, and E_x is the eigenenergy. This problem is identical to a bound particle in a square well potential and the solutions are very familiar from elementary quantum mechanics (shown in Figure 2.4). Here, $V(x) = 0$ inside the well, and $V(x) = \infty$ outside. The envelope wavefunctions in this case are:

$$\psi(x) = \sqrt{\frac{2}{L_x}} sin\left(\frac{(n+1)\pi x}{L_x}\right) \tag{2.2}$$

with eigenenergies given by

$$E_n = \frac{\hbar^2\pi^2}{2m^*}\left(\frac{(n+1)^2}{L_x^2}\right) \tag{2.3}$$

Since the energy levels are quantized, the quantum number, $n = 0, 1, 2\ldots$ is introduced, where $n = 0$ represents the ground state. The envelope wavefunctions and eigenenergies from Equation (2.2) and (2.3), respectively, for the 1D step-like confinement potential are shown in Figure 2.4. In the calculation presented here, the following parameters were used: $L_x = 10\,\text{nm}$, and $m^* = 0.055m_0$. These solutions illustrate the restriction of allowed energies that results from the boundary conditions of the confined carrier being constrained by the 1D potential. If the potential were only in 1D, the carrier would be free to move along the 2D plane for the allowed energies in the x-direction. However, in a quantum dot, the confinement potential in other crystal directions (y, z) also constrains the particle such that the carrier is 'trapped' in 3D. Since the Schrödinger equation is separable for the "quantum box" potential in 3D, the 1D Schrödinger equation can be applied along the y-, and z-direction similarly to that of the solution along the the x-direction. Adding the sum of the eigenenergies along all three crystal directions provides the solution in 3D. Now, the single particle quantized energy levels in 3D are

$$E_{nml} = \frac{\hbar^2\pi^2}{2m^*}\left\{\frac{(n+1)^2}{L_x^2} + \frac{(m+1)^2}{L_y^2} + \frac{(l+1)^2}{L_z^2}\right\} \tag{2.4}$$

with quantum numbers $n, m, l = 0, 1, 2\ldots$. The allowed energies resulting from the quantum dot's 3D confinement potential depends strongly on the size of the "quantum box" and the effective mass. For the special case when $L_x = L_y = L_z$, (*i.e.*, a quantum dot with high symmetry), the energy levels form shells of increasing degeneracy, where the shell separation increases with incrementing quantum number. Normally

however, the quantum dot does not have high symmetry and the growth direction (z-direction) is much smaller than the the lateral dimensions (*i.e.*, $L_z < L_x, Ly$). From Equation (2.4), the energy scale introduced by the stronger, vertical confinement is larger than the contribution by the lateral confinement. Here, widely spaced energy levels are expected due to the vertical confinement and more closely spaced energy levels due to the lateral confinement. In other words, the many closely spaced quantized levels resulting from the lateral confinement are integrated within each vertical subband. If the quantum dot height is made sufficiently small, as is the case for most quantum dot systems, then the bound states only contain the lowest vertical subband. Higher subbands are above the barrier, in the continuum of states resulting from the finite barrier height of the quantum dots confining potential. The band offsets for the conduction and valence bands in InAs/InP quantum dots including strain are $\Delta E_c = 320\,\text{meV}$ and $\Delta E_v = 530\,\text{meV}$, respectively [61].

Due to the fact that the confinement potential is stronger in the vertical direction than the lateral direction in quantum dot nanostructures, the confining potential can be approximated by a step-like quantum well potential in the growth direction as discussed previously, and a weaker 2D lateral confining potential. For certain types of dot shapes, such as a lens-shaped self-assembled quantum dot (Figure 2.5(a)), the in-plane confining potential can be approximated by a 2D parabolic potential [62–66] (Figure 2.5(b)). Such a confining potential arises due to the varying thickness of the dot layer as a function of dot radius [62]. The confinement is largest when the dot layer is the thickest (*i.e.*, $x = y = 0$) and smallest when closest to the wetting layer. The 2D parabolic potential proves to be quite useful to represent the lateral confining potential of a single quantum dot since the single particle energies of such a dot can be obtained

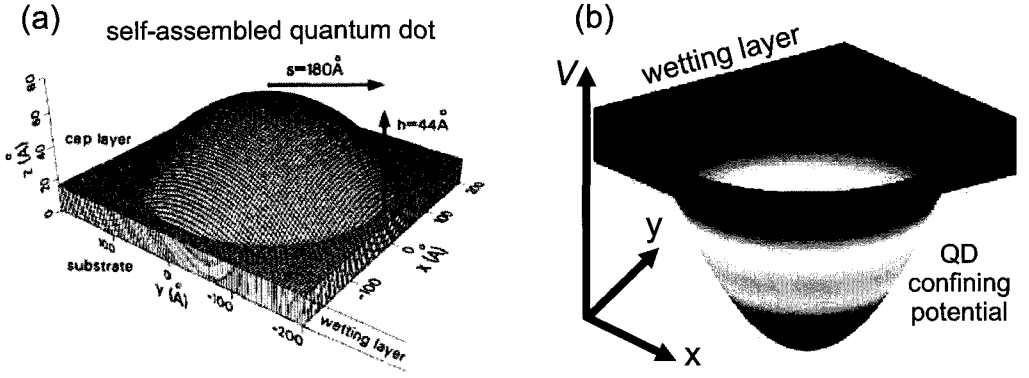

Figure 2.5: (a) Schematic representation of lens-shaped InGaAs self-assembled quantum dot [62]. (b) The confining potential, V, of a lens-shaped self-assembled quantum dot is represented by a 2D parabolic potential. The 2D parabolic potential in the plane of the quantum dot arises for certain dot shapes, such as a lens-shaped quantum dot. The single particle energies can be obtained by solutions of the 2D harmonic oscillator in the effective mass approximation.

analytically from the solutions of the 2D harmonic oscillator. Moreover, the solutions of the 2D confining potential qualitatively portray the essential physics of a single quantum dot including optical selection rules and energy shell separation, as well as providing a simple picture for understanding interactions of external perturbations within the single quantum dot, such as an applied magnetic field [65, 66] or applied lateral electric field as demonstrated in this thesis.

Detailed calculations have been performed for more sophisticated confining potentials that take into account the various shapes and sizes of quantum dots, including strain. However, these calculations are very complicated, require large computational effort [67] and do not always allow one to understand the physical picture. The 2D parabolic potential is much simpler to calculate and is not far from the true potential of a single quantum dot as revealed by the demonstration of state-filling spectroscopy in a single quantum dot [64] and the Fock-Darwin spectra observed in a magnetic

field [65,66]. In these experimental studies, the assumption of a 2D harmonic oscillator potential was used to describe the observed shell-structure and evolution of shells with magnetic field for both ensembles of quantum dots and that of a single quantum dot. More recently, the calculated energy level spacing for InAs/InP quantum dots using an atomistic pseudopotential method was found to be nearly equal, which is in rough agreement with the effective mass approximation utilizing a 2D harmonic oscillator confining potential [61].

2.2 Two-dimensional harmonic oscillator

As discussed in the previous section, the solutions of the 2D harmonic oscillator prove to be a very good approximation for the weaker lateral confining potential of the quantum dot [62–66]. For a semiconductor quantum dot in which the height is much smaller than the lateral dimensions, the lateral confining potential can be decoupled from the vertical confinement. This is the case for the single quantum dots studied in this thesis, as the ratio of the quantum dot height to lateral dimensions is typically 1:10 [68]. In addition, typical quantum dot heights fabricated in this thesis (~3-5 nm), only contain one vertical subband for the depth of the well in the growth direction. In such circumstances, the much weaker lateral confining potential can be represented by a 2D parabolic potential, of which the solutions to the single particle energies can be obtained analytically by the 2D harmonic oscillator.

The 2D parabolic potential representing the quantum dot in the x-y plane (lateral direction) is given by

$$V(x,y) = \frac{1}{2} m^*_\beta w^2_\beta (x^2 + y^2) \tag{2.5}$$

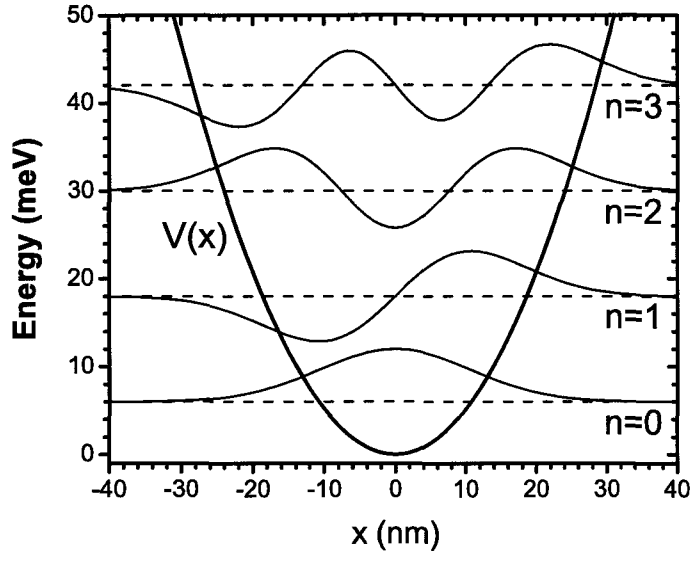

Figure 2.6: Parabolic potential, $V(x)$, of 1D harmonic oscillator. The energy levels and wavefunctions of the 1D harmonic oscillator for the lowest four levels is plotted. In 2D, this potential is rotationally symmetric about the z-axis (growth direction) and is found to be a good approximation to represent the confinement potential of a single quantum dot.

where (x,y) is the position of the particle subject to the confining potential, m^*_β is the effective mass of the particle, and $\hbar w_\beta$ is the characteristic harmonic oscillator energy, where $\beta = e, h$ identifies the carrier type (e for electron and h for hole). This parabolic potential for 1D (x-direction) is shown in Figure 2.6. For the case of the 2D parabolic potential given in Equation 2.5, this 1D potential is rotationally symmetric about the z-axis.

Next, the unperturbed single particle Hamiltonian of the confined carrier is

$$H_\beta = \frac{\hat{p}^2}{2m^*_\beta} + V(x,y) \tag{2.6}$$

Here, $\hat{p}^2/2m^*_\beta$ is the kinetic energy of the carrier, and $\hat{p}$ is the momentum ($\hat{p} = -i\hbar\left[\frac{\partial}{\partial x} + \frac{\partial}{\partial y}\right]$). The single particle Hamiltonian is separable in the x-, and y- dependent parts for the 2D parabolic potential which gives

$$H_\beta = H_\beta(x) + H_\beta(y) \tag{2.7}$$

Now, the time-independent Schrödinger equation can be solved for two uncoupled harmonic oscillators. In 1D, Equation (2.1) becomes

$$-\frac{\hbar^2}{2m^*_\beta}\frac{\partial^2}{\partial x^2}\psi(x) + \frac{1}{2}m^*_\beta w^2_\beta x^2\psi(x) = E\psi(x) \tag{2.8}$$

Next, the physical quantities of position and energy can be eliminated by introducing an effective length scale, x_0, and energy scale, E_0, such that the Schrödinger equation is dimensionless. Here, the derivation is similar to that presented in Ref. [69]. First, Equation (2.8) can be rearranged to obtain

$$\left[-\frac{\partial^2}{\partial x^2} + \left(\frac{m^*_\beta w_\beta}{\hbar}\right)^2 x^2\right]\psi(x) = \frac{2mE}{\hbar^2}\psi(x) \tag{2.9}$$

By inspection of the left hand side (LHS) of Equation (2.9), the dimensions of length can be eliminated by setting

$$\overline{x} = \frac{x}{x_0}, \qquad x_0 = \sqrt{\frac{\hbar}{m^*_\beta w_\beta}} \tag{2.10}$$

Carrying this out gives

$$\left[-\frac{\partial^2}{\partial \overline{x}^2} + \overline{x}^2\right]\psi(\overline{x}) = \frac{2E}{\hbar w_\beta}\psi(\overline{x}) \tag{2.11}$$

Similarly, the dimensions of energy can be eliminated by setting

$$\overline{E} = \frac{E}{E_0}, \qquad E_0 = \hbar w_\beta \tag{2.12}$$

Finally, a dimensionless Schrödinger equation is obtained with pure numbers $\overline{x}$ and $\overline{E}$:

$$\frac{\partial^2}{\partial \overline{x}^2}\psi(\overline{x}) + \left(2\overline{E} - \overline{x}^2\right)\psi(\overline{x}) = 0 \tag{2.13}$$

The solutions to the differential Equation (2.13) is well known and can be found in many quantum mechanics text books. Without going into detail, the allowed energy levels of the 1D harmonic oscillator are:

$$E_n = \hbar w_\beta \left(n + \frac{1}{2}\right) \tag{2.14}$$

with quantum numbers $n = 0, 1, ...,$ and corresponding normalized wavefunctions

$$\psi_n(x) = \frac{1}{\sqrt{2^n n!}} \left(\frac{1}{x_0^2 \pi}\right)^{1/4} H_n(x) \exp\left(\frac{-x^2}{2x_0^2}\right) \tag{2.15}$$

Here, the wavefunctions of the quantum harmonic oscillator contain the Hermite polynomials, $H_n(x)$ for a given quantum number, n. The first few Hermite polynomials are

$$\begin{aligned} H_0(x) &= 1, & H_2(x) &= 4\left(\frac{x}{x_0}\right)^2 - 2 \\ H_1(x) &= 2\frac{x}{x_0}, & H_3(x) &= 8\left(\frac{x}{x_0}\right)^3 - 12\frac{x}{x_0} \end{aligned} \tag{2.16}$$

The Hermite polynomials are multiplied by a Gaussian (last term in Equation 2.15) which allows the boundary conditions to be satisfied at $x = \pm\infty$. The solutions of the lowest four wavefunctions of the 1D harmonic oscillator are plotted in Figure 2.6. In contrast to the particle in a box with infinite boundary conditions, the wavefunctions

penetrate into the barrier before they decay. In addition, the energy levels are equally spaced for the quantum harmonic oscillator, whereas for the case of the particle in a box, they increase with larger quantum number, n. The potential, $V(x)$, shown in Figure 2.6 with corresponding solutions of eigenstates and eigenenergies uses a value of $\hbar w_e$ that is characteristic of electrons for the InAs/InP quantum dots studied in this thesis ($\hbar w_e = 12\,\text{meV}$, $m_e^* = 0.055 m_0$). The fundamental result of the 2D harmonic oscillator is that the Hamiltonian is separable in the x- and y directions, such that the solutions are obtained analytically. This proves to be very useful when understanding the effects of an applied lateral electric field studied later in Chapter's 5, 6, and 7. By including the solutions in the y-direction, the single particle harmonic oscillator energies in 2D are

$$\varepsilon_{nm}^{\beta} = \hbar w_{\beta}\,(n + m + 1) \tag{2.17}$$

with quantum numbers, $n, m = 0, 1, 2 \ldots$. Similar to the 1D case, the energy level separation of the harmonic oscillator states does not change with increasing quantum numbers. However, the energy of the ground state in the 2D case is twice that of the 1D case. In addition, the number of degenerate harmonic oscillator states in 2D increase for incrementing quantum numbers n and m (*i.e.*, for equal values of $n+m$). Here, the confinement potentials in the x- and y- directions of the harmonic oscillator are assumed to be identical (*i.e.*, the 2D parabolic potential is rotationally symmetric about the z-axis). The energy eigenstates of the 2D harmonic oscillator represents 'shells' analogous to that of an atom and forms the basis of the shell model for single quantum dots. The shell model provides an excellent framework for describing the fundamental physics in these nanostructures such as the optical selection rules of single quantum dots, as well as external perturbations applied to them [63]. The

shell model is used in describing the optical selection rules in the next section, as well as describing the gated InAs/InP quantum dots studied in this thesis.

2.3 Optical selection rules for single quantum dots

Thus far, I have treated holes in a single quantum dot as 'quantum particles' similar to electrons, but with opposite charge. The holes move in a quantum dot confining potential defined by their own effective mass m_h^*. Such an assumption is made in the effective mass approximation and is valid for dots in which there is minimal heavy-hole/light-hole mixing. This creates "clean" optical selection rules to describe the optical transitions observed in single quantum dots. These "clean" optical selection rules are used to explain the observed optical transitions throughout this thesis at zero electric field and as a basis when these optical transitions are manipulated with an external vertical or lateral electric field. However, this heavy-hole/light-hole mixing cannot be neglected in all cases and is found to become important for tall dots [70] or spherical dots [60] as determined by atomistic pseudopotential calculations. Once mixing of hole states becomes important in the valence band, the optical selection rules are modified in quantum dots and include very complex hole-hole interactions [63, 71]. In the case of strained InAs/InP quantum dots studied in this thesis, the splitting of the heavy and light holes is expected to remove these complications of hole-hole interactions and justifies the use of the one-band effective mass approximation [63]. First, there is an expected heavy-hole/light-hole splitting due to the different confinement energies for heavy and light holes (see Figure 2.7). Second, the strain of InAs/InP quantum dots further splits the heavy and light hole. In fact, the predominant character for lens-shaped InAs dots embedded in host materials of

GaAs or InP is heavy-hole like due to compressive strain as determined by atomistic pseudopotential calculations [60, 61]. In these calculations, the heavy-hole/light-hole splitting for InAs/InP quantum dots was determined to be smaller than InAs/GaAs quantum dots (120 meV compared to 180 meV). Outside of the quantum dot, the heavy-hole light hole splitting changes sign (*i.e.*, ground state is dominated by light-hole) [60]. As it turns out, the valence band ground state for flat self-assembled InGaAs/GaAs quantum dots was found to contain at least 95% heavy hole character [72]. Although InAs/GaAs quantum dots has a different host material than InAs/InP quantum dots, a large heavy-hole/light-hole splitting is expected as stated above (>100 meV) [61], thus validating the use of the one-band effective mass approximation in this thesis by assuming heavy holes only and no mixing with light holes.

2.3.1 Angular momentum of single particle electron and hole states

To determine the optically allowed transitions of a single quantum dot, the spin-orbit interaction should be included, which scales with the atomic number of the atom. Such an interaction describes the coupling of the electron spin to the orbital angular momentum and is necessary to understand how the single particle electron states in the conduction band and the hole states in the valence band of a quantum dot, couple to the light field.

In a bulk 3D semiconductor, the conduction and valence bands are constructed from the bonding of neighbouring atoms. For example, in silicon there are four valence electrons, two in a filled s orbital and two in a partially filled p orbital, which

can accommodate a total of six electrons. Each of the four neighbouring Si atoms contributes one valence electron to completely fill this outer shell, forming bonds which make the crystal lattice more stable. These orbitals of neighbouring atoms overlap and hybridize into sp^3 orbitals. The bonding combinations of the sp^3 orbitals form the valence band and the anti-bonding combinations form the conduction band. The valence band is completely filled since each of the four neighbouring Si atoms contributes one valence electron necessary to bond the crystal lattice. The splitting between these two bands is the forbidden energy gap, where no states are allowed. Now, by thermal or optical excitation with an energy greater than the energy gap, an electron can be excited to the empty conduction band, leaving behind a missing electron in the valence band; also known as a hole. This excitation process is only allowed by conserving energy and momentum (*i.e.*, for the same wavevector, k).

To understand the optical selection rules in single quantum dots, it is important to understand the nature of the wavefunction. In both InP, InAs, and GaAs for example, the bottom of the conduction band has s-like wavefunctions and the valence band has p-like wavefunctions. This simple picture does not work as well in the conduction band as the electrons spread out further in the crystal and retain less of their atomic character. Analogous to atomic physics, s-states have zero orbital angular momentum (*i.e.*, $l = 0$), while p-states correspond to $l = 1$. After including the spin, $s = \frac{1}{2}$ for an electron, the total angular momentum of the conduction band ground state is $j = l + s = \frac{1}{2}$, and $j = l - s = -\frac{1}{2}$. Similarly for the p-like valence band wavefunctions, they correspond to $l = 1$ with allowed eigenstates of $l_z = \{-1, 0, 1\}$. When including the spin of the hole, there is a total of six possible hole states for the ground state. For example, when $l = 1$ and $s = \frac{1}{2}$, the eigenvalues of j can take

on two possible values: $j = l + s = \frac{3}{2}$ and $j = l - s = \frac{1}{2}$. The eigenvalues of j_z now have a possibility of $2j + 1$ states with values $j, j-1, \ldots, -j$. When $j = \frac{3}{2}$, the possible values of j_z are $\{\frac{3}{2}, \frac{1}{2}, -\frac{1}{2}, -\frac{3}{2}\}$, and when $j = \frac{1}{2}$, the possible values of j_z are $\{\frac{1}{2}, -\frac{1}{2}\}$. The spin-orbit interaction in the valence band splits the $j = 3/2$ states from the $j = 1/2$ states. This splitting is referred to as the spin-orbit splitting where the states with $j = 1/2$ are the split-off hole bands and are typically 380 meV below the $j = 3/2$ states for bulk InAs [59] and therefore can be ignored. In bulk, the $j = 3/2$ states are degenerate where $j_z = \pm\frac{1}{2}$ is defined as the light-hole band and $j_z = \pm\frac{3}{2}$ as the heavy-hole band. This simplified picture of the band edge structure is summarized in Figure 2.7 for a direct gap semiconductor using typical values of bulk InAs, with corresponding dispersion relations ($E = \hbar^2 k^2 / 2m^*$) of their respective bands for electrons and holes in the effective mass approximation. As mentioned previously, the confinement and strain of the quantum dot splits the degeneracy of heavy-hole and light-hole states. For the InAs/InP quantum dots studied in this thesis, this splitting is large enough (>100 meV) [61] such that the light-hole band can be neglected. Therefore, the optically allowed transition for the quantum dot ground state occurs when the $j_z = \pm\frac{1}{2}$ single particle electron states recombine with the $j_z = \pm\frac{3}{2}$ heavy-hole single particle hole states.

To couple to the light field, the total angular momentum between the conversion of spin to light must be conserved. Since photons carry one unit of angular momentum (either $+1$ or -1), optically allowed transitions in a quantum dot must occur between energy levels where the difference in total angular momentum between the initial and final state is $|\Delta J\rangle = |\pm 1\rangle$. In addition, these optically allowed transitions must have total spin of zero (*i.e.*, an electron with spin up recombines with hole of spin down

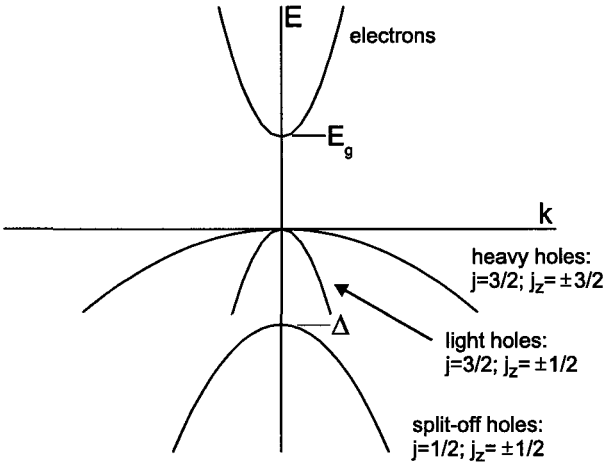

Figure 2.7: Simplified view of band edge structure of a direct gap semiconductor. The dispersion relations in the effective mass approximation for electrons, heavy holes, light holes, and split-off holes are shown. The spin-orbit splitting is represented by Δ, and E_g corresponds to the energy of the bandgap. Optical transitions occur when an electron in the conduction band recombines with a hole in the valence band with same wavevector, k.

and vice versa). In strongly confined systems (*e.g.*, quantum dot), an electron binds together with a hole to form an exciton. The exciton energy is lowered compared to the single particle energy of electron and hole by their mutual Coulomb attraction (see Section 2.4 for more details). By considering the heavy-hole and electron single particle states of the quantum dot ground state, there are four possible excitonic transitions; they are

$$|\Delta J\rangle = \pm \left|\frac{1}{2}\right\rangle_e \pm \left|\frac{3}{2}\right\rangle_h \tag{2.18}$$

which yield two optically bright exciton states with $|\Delta J\rangle = |\pm 1\rangle$ and two optically dark exciton states with $|\Delta J\rangle = |\pm 2\rangle$. For example, when a $|-1/2\rangle$ ($|+1/2\rangle$) electron recombines with a $|+3/2\rangle$ ($|-3/2\rangle$) heavy-hole, the angular momentum is +1 (-1). By the conservation of angular momentum, a photon is emitted with angular momentum

± 1, where light with angular momentum of +1 (-1) has right circular polarization (left circular polarization).

2.3.2 Shell model of single quantum dots

To extend the optical selection rules to the excited states of a single quantum dot, the shell model is utilized. The shell model of single quantum dots has demonstrated to be a very good approximation when describing their electronic properties and optical selection rules [63]. As discussed previously, this is the case when the lateral confining potential of the quantum dot is much weaker than the vertical confinement, as is the case for the single quantum dots studied in this thesis. For the dot heights considered in this thesis (~3-5 nm), only one vertical subband is occupied due to the strong vertical confinement. The weaker 2D confining potential is represented by the 2D harmonic oscillator, which can be solved exactly (see Section 2.2). The resulting eigenstates of the 2D harmonic oscillator represent the *s*-, *p*-, and *d*-shell, respectively for a single quantum dot that only contains one vertical subband from the stronger vertical confinement. For a symmetric dot, the single particle energies for electrons and holes correspond to the single particle energies of the 2D harmonic oscillator as in Equation (2.17). However, for asymmetric dots the single particle energies for electrons (or holes) correspond to two harmonic oscillators with different oscillator energies, $\hbar w_x^\beta$, and $\hbar w_y^\beta$ [63]:

$$E_{mn}^\beta = \hbar w_x^\beta \left(n + \frac{1}{2}\right) + \hbar w_y^\beta \left(m + \frac{1}{2}\right) \tag{2.19}$$

Note that the single particle energies for holes are described analogous to that of electrons, but with their own characteristic harmonic oscillator energy in Equation (2.19).

In addition, these single particle energies exclude the energy offset which includes the energy gap of the dot material and the shift created by the vertical confinement.

In this model, the optically allowed transitions from electrons in the conduction band and holes in the valence band are given for vanishing angular momentum, l, conservation of the total spin, s (*i.e.*, opposite spin for electron and hole), and for states within the same shell of the quantum dot. These allowed transitions, represented as arrows are summarized in Figure 2.8. The angular momentum for a particular electron state is given by:

$$l^e_{mn} = m - n \tag{2.20}$$

In contrast, the angular momentum for the hole state which can be treated as a positively charged particle in this model has angular momentum opposite to that of the electron:

$$l^h_{mn} = n - m \tag{2.21}$$

Now, the optically allowed transitions of a single quantum dot shown in Figure 2.8 can be described with shells analogously to that of atoms. For example, the lowest eigenstate is with both $n = m = 0$ ($(n, m) = (0, 0)$) and is the ground state of the system, which can therefore be referred to as the s-shell. When introducing spin, σ, to Equation (2.19), the s-shell is doubly degenerate due to the Pauli exclusion principle that requires two electrons (or holes) of opposite spin. The second degenerate shell is the p-shell and consists of the eigenstates $(n, m) = (0, 1)$, and $(n, m) = (1, 0)$, with angular momentum ± 1. The third shell, called the d-shell, consists of the eigenstates $(n, m) = (0, 2)$, $(1, 1)$, $(0, 2)$. Each of these eigenstates for the p-, and d-shell are also spin-degenerate. Thus, the total degeneracy is $2n^*$, where n^*, is the shell index $n^* = 1, 2, 3$ for the s-, p-, and d- shell, respectively. Note, that this degeneracy for the

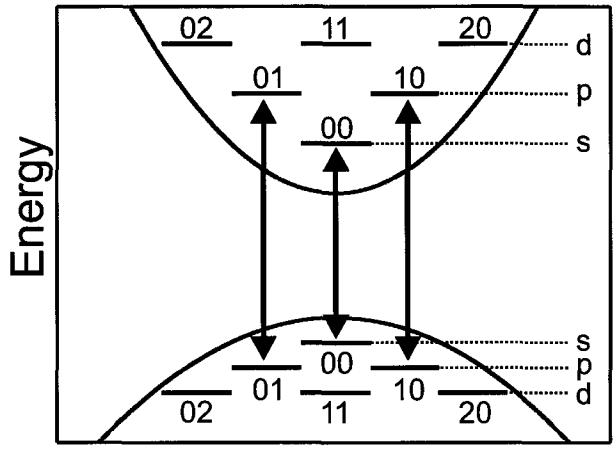

Figure 2.8: Shell model for single quantum dots represented by a 2D parabolic potential in the xy-plane and a step-like potential along the growth direction. The arrows represent the optically allowed transitions with vanishing angular momentum in the shell model and occurs from electrons in the conduction band and holes in the valence band within the same quantum dot shell (note that total spin must also be conserved).

s-, p-, and d-shells is broken if the dot shape is asymmetric (*i.e.*, $\hbar w_x^\beta \neq \hbar w_y^\beta$) as is the case for most real quantum dot systems and the quantum dots studied throughout this thesis.

2.4 Few particle interactions

Optical transitions in single quantum dots are subject to Coulomb interactions of strongly confined carriers, which modify the observed emission energy. Depending on the number of confined electrons or holes, the quantum dot is either electrically neutral or charged. Each optical transition involving a neutral or charged exciton has a unique optical signature in emission energy and number of observed spectral lines [5, 7, 63, 64]. It is these optical signatures of few particle interactions that allow

the observed single excitonic transitions to be identified in this thesis. This section excludes any fine-structure splitting arising in an asymmetric shaped dot which breaks the degeneracy of single excitonic states with opposite spin configuration [64]. The resolution of the fine-structure splitting for the ground state exciton is $\sim 10-100\,\mu$eV for InGaAs/GaAs dots [64,73] and $\sim 100-200\,\mu$eV for the InAs/InP quantum dots studied in this thesis. Details of the fine-structure splitting are discussed within the data analysis.

Few particle interactions are first illustrated for the neutral exciton, X^0, in Figure 2.9(a) with a single electron-hole pair occupying the quantum dot s-shell of opposite spin. Since the electron and hole are oppositely charged, Coulomb interactions attract and bind the pair together to form an exciton. Following the optical selection rules of single quantum dots using the shell model, the electron-hole pair with opposite spin and vanishing angular momentum recombine to emit a photon with polarization based on their spin configuration. After the photon is emitted, the quantum dot is empty. Therefore, the single exciton energy can be determined by optical experiments. The energy of the emitted photon is lower in comparison to recombination of a non-interacting electron-hole pair. The magnitude of reduction is determined by the exciton binding energy, which is considerably enhanced in quantum dots due to the stronger Coulomb interactions of electron and hole resulting from 3D confinement. The exciton binding energy is calculated using the single particle wavefunctions $|m,n\rangle$ from the 2D harmonic oscillator and Coulomb attraction of the electron and hole, V_{eh}, treated as a perturbation. The single exciton energy is therefore the single particle energies of the electron, E_e, and hole, E_h, and their mutual Coulomb attraction:

$$E_{X^0} = E_e + E_h - V_{eh} \tag{2.22}$$

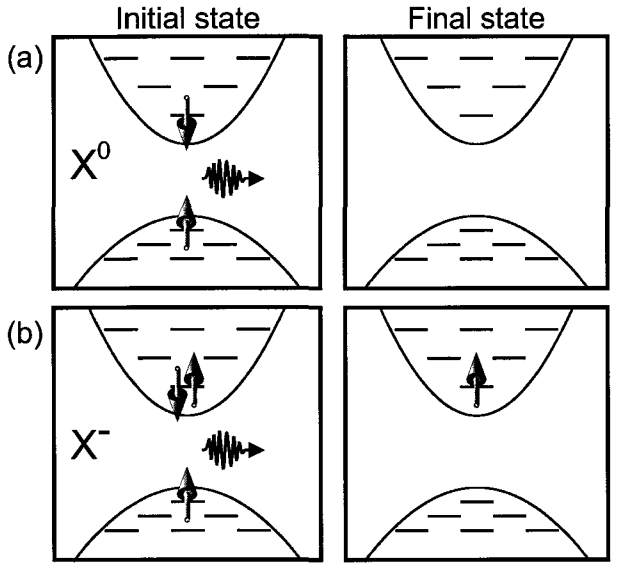

Figure 2.9: Few particle interactions of single excitonic states, X^0 and X^-. The initial state of the quantum dot is shown in the left panel and the final state is shown in the right panel.

The electron-hole interaction element, V_{eh}, in the quantum dot s-shell corresponds to [63]

$$V_{eh} = \langle 00,00|V_{eh}|00,00\rangle = \frac{e^2}{4\pi\epsilon\epsilon_0}\int d^3\vec{r}_1 d^3\vec{r}_2 \frac{\phi^*_{00}(\vec{r}_1)\phi^*_{00}(\vec{r}_2)\phi_{00}(\vec{r}_2)\phi_{00}(\vec{r}_1)}{|\vec{r}_1 - \vec{r}_2|} \quad (2.23)$$

for an electron at position $\vec{r}_1$, and hole at position $\vec{r}_2$. The recombination energy of the neutral exciton is modified by the presence of an additional electron in the quantum dot. This configuration with two electrons and one hole in the quantum dot s-shell is known as the singly charged exciton, X^-, and is shown in Figure 2.9(b). Here, the additional electron populates the quantum dot s-shell with opposite spin due to the Pauli exclusion principle. To calculate the energy required to bind an additional electron to the quantum dot, the Coulomb repulsion of the two electrons and exchange interaction of electron and hole is taken into account. This interplay of

the Coulomb interactions determines whether X^- is above or below X^0. Typically, the magnitude of the re-normalization energy for X^- in InAs/InP quantum dots is $\sim 4-5\,\text{meV}$ below X^0. Such charged exciton species are prepared experimentally in this thesis by a vertical electric field as described in Chapter 8. Similar to the neutral exciton, there is only one final state and therefore only one line is expected in the optical spectrum. In contrast to X^0, the final state of X^- is a single confined electron. The transition energy of X^- is given by,

$$E_{X^-} = E_X + V_{ee} - V_{eh} \tag{2.24}$$

where E_{X^0} is the transition energy of X^0 and V_{ee} is the electron-electron Coulomb repulsion and V_{eh} is the electron-hole Coulomb attraction (exchange interaction). In this expression, it is the electron-electron and electron-hole Coulomb interaction terms that differentiate the transition energy of X^- from that of X^0. Calculation details for the Coulomb matrix elements can be found in the work of P. Hawrylak [63]. An additional term that is neglected in Equation (2.22) and (2.24) is the correlation energy. The correlation energy is a small perturbation of the exciton energy that further redshifts the transition energy. See Chapter 5 for more details.

Thus far, there is only one line expected in the optical spectrum for X^- and X^0 since there is only one possible final state. The doubly charged exciton, X^{2-} is used to demonstrate that the number of spectral lines in the optical spectrum increases with the number of possible final states. X^{2-} contains three electrons and one hole. Since the quantum dot s-shell can only accommodate two electrons of opposite spin, the third electron populates the p-shell as shown in Figure 2.10. After X^{2-} decay, there are four possible spin configurations of the remaining electrons in the final state with one electron in the s-shell and one in the p-shell. The final spin configuration can

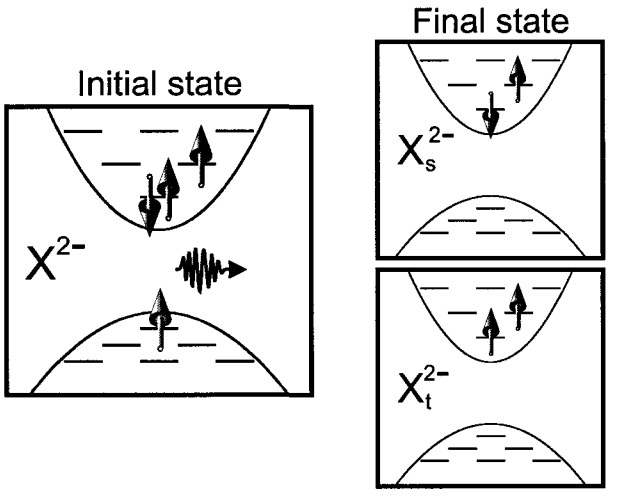

Figure 2.10: Few particle interactions of X^{2-}. There are two expected lines in the optical spectrum for X^{2-} due to the spin singlet (X_s^{2-}) and triplet (X_t^{2-}) energy splitting in the final state. Only one of the three possible spin configurations is shown for the triplet state (see Equation 2.25).

either be in a singlet state, X_s^{2-}, or one of three triplet states, X_t^{2-}, with corresponding wavefunctions, $|S\rangle$, and $|T\rangle$, respectively:

$$|S\rangle = \frac{1}{\sqrt{2}}(\uparrow\uparrow - \downarrow\uparrow)$$
$$|T\rangle = \begin{cases} \uparrow\uparrow \\ \downarrow\downarrow \\ \frac{1}{\sqrt{2}}(\uparrow\downarrow + \downarrow\uparrow) \end{cases} \tag{2.25}$$

Neglecting Coulomb interactions, the energy of the singlet and triplet spin configurations are degenerate. Taking Coulomb interactions into account, the energy levels of the singlet and triplet state are shifted to higher energy due to Coulomb repulsion of the two electrons. Finally, considering the exchange interaction of the two electrons, the triplet state is shifted to lower energy from the singlet state. The magnitude of the singlet-triplet state splitting is 2K, where K is the exchange interaction energy of

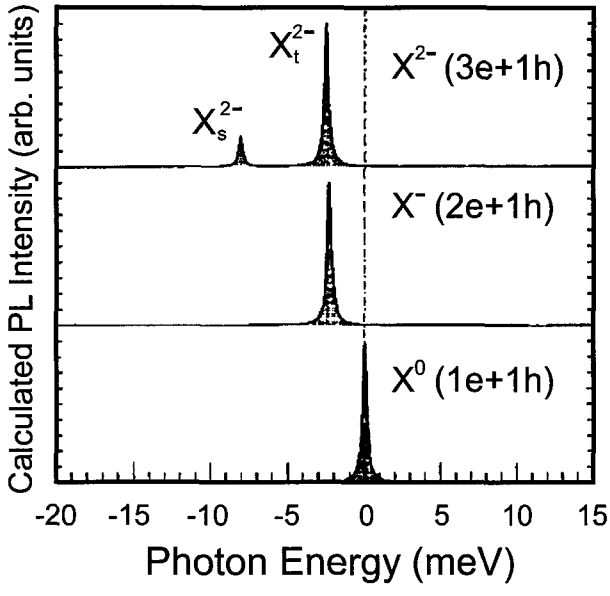

Figure 2.11: Calculated PL spectra of X^0, X^-, and X^{2-}. The number of spectral lines expected in the optical spectrum increases with the number of possible final states [74].

the two electrons [4,5]. Since there is an energy splitting of the singlet and triplet few particle states from X^{2-} decay, two optical transitions are expected in the observed optical spectrum [4,5].

To illustrate few particle effects on the resulting optical spectrum for single excitonic states, the calculated photoluminescence (PL) spectrum of X^0, X^-, and X^{2-} is depicted in Figure 2.11 [74]. The calculated PL spectra are based on model calculations assuming a quantum well like potential in the growth direction and 2D parabolic potential in the plane of the quantum dot. The calculations performed by U. Hohenester and E. Molinari [74] follows the approach presented in [63, 75] with an assumption that the confinement energy for electrons is twice that for holes (*i.e.*,

$\hbar\omega_e = 2\hbar\omega_h$). Such model calculations reproduce qualitatively important characteristics of self-assembled quantum dots (*i.e.*, measured inter-level spacing of the *s*- and *p*-shell and few particle interactions). As discussed previously, the X^- transition is renormalized by Coulomb interactions and found to be $\sim 2-3\,\text{meV}$ below that of the X^0 transition, with both of the optical transitions comprising of only one observed spectral line. As expected, the calculated optical spectrum for X^{2-} is found to have two spectral lines, the strongest of the two is slightly red shifted with respect to the X^0 line. Since the PL is the difference in energy of the initial and final states, the singlet state is at lower emission energy than the triplet state, but with reduced amplitude [74]. The reduced amplitude of the singlet state is attributed to the number of possible spin configurations in the final state, which is only one compared to the triplet state, which has three. Note that the renormalization energies of the single excitonic states presented here are strongly dependent on the spatial extent of the electron and hole wavefunctions which modify whether the charged exciton states are either above or below the neutral exciton. In contrast, the energy splitting of the singlet and triplet states is relatively constant for the range of electron and hole wavefunctions studied. In that work, the spatial extent of the wavefunction, L_e, for the electron to that of the hole, L_h, varied from $L_e : L_h$ of 1 : 2 to 2 : 1 [4]. The spatial extent of the wavefunction, also known as characteristic length of the parabolic confinement for electrons and holes, is defined by $L_e = (\hbar/m_e^* w_e)^{1/2}$ and $L_h = (\hbar/m_h^* w_h)^{1/2}$, respectively [69]. The calculations presented here are confirmed by experimental investigation for InGaAs quantum dots embedded in GaAs [4,5] and are in excellent qualitative agreement for the charge tunable InAs/InP quantum dots presented in this thesis (see Chapter 8).

Chapter 3

Single dot growth and isolation

Over a decade ago, experimental techniques were developed to isolate and probe a single quantum dot [76–81]. Probing individual quantum dots made studying their underlying electronic structure, as discussed in the previous chapter, a possibility. The spectral resolution of these experiments enabled the study of few particle interactions between carriers (electrons and holes) confined in the quantum dot as well as the demonstration of atom-like spectra from individual quantum dots [80, 81]. A clear signature of this atom-like behavior of individual quantum dots is the observation of sharp optical emission lines, resulting from the recombination of single electron-hole pairs that become spatially isolated in three dimensions due to the confining potential of the quantum dot. For high quality dots, the linewidths of the optical transitions are limited by the exciton recombination lifetime ($\sim 1\,\mu$eV) [82].

More recently, the ability to isolate a single quantum dot has enabled the study of quantum devices for application in quantum cryptography and quantum information processing systems [1]. To date, such devices have relied upon randomly nucleated quantum dots. Examples of device utilization include precisely controlling the number of both electrons and holes confined within the quantum dot, thus modifying the

total charge [2, 5, 7, 8]; performing coherent manipulation of a single electron spin on timescales ranging from nanoseconds down to picoseconds before the electron spin is lost due to decoherence [11–13, 15] and; tuning the optical transitions of a single quantum dot for single photon or entangled photon applications making the long distance transfer of quantum information a possibility [24].

Until recently, there were a limited number of experimental techniques for isolating and probing a single quantum dot to allow study of the aforementioned device applications. These experimental techniques included: high spatial resolution cathodoluminescence [76]; near field optics [79] and; micro-photoluminescence (μ-PL) [80, 81]. Cathodoluminescence can probe an area below 50 nm, much less than optical techniques can achieve due to the diffraction limited laser spot ($\sim 1\,\mu$m). These single dot spectroscopy techniques are useful to probe single quantum dots formed by quantum well interface fluctuations [77] since the dot density is sufficiently low. However, for self-assembled quantum dots formed by the Stranski-Krastanow growth mode, the surface density is typically higher ($10 - 100\,\mu\text{m}^{-2}$) and the limit of single dot spectroscopy is more difficult to achieve.

Present day technology now makes isolating single dots for optical spectroscopy relatively simple. The most common method being utilized around the world to study single dots is to combine both optical spectroscopy and post-growth processing techniques. With these optical methods, the resolution required to probe a single quantum dot can be achieved by etching sub-micron mesas [80, 83] or by processing sub-micron nano-apertures with metallic shadow masks [8, 81]. These techniques are summarized in Figure 3.1 along with a pair of scanning electron microscope images

of samples fabricated for single dot spectroscopy. In Figure 3.1(a), the necessary isolation is achieved by etching a pillar such that only a single quantum dot remains. In this isolation technique, the 1 μm laser spot only excites the single quantum dot since the surrounding material has been removed. In Figure 3.1(b), a nano-aperture is used to isolate a single quantum dot. The nano-aperture is fabricated by evaporating an opaque metal film (*e.g.*, gold) onto the sample surface containing self-assembled quantum dots, after which a sub-micron hole is made with e-beam lithography, followed by etching. After processing, the 1 μm laser spot only excites quantum dots below the nano-aperture. If the dot density is sufficiently low (*i.e.*, less than one dot per aperture), then it is possible to isolate a single quantum dot.

Although the fundamental physics of single dots can be studied with these methods, a major disadvantage is that the count rate of the single dot emission is significantly reduced by current processing methods. In the case of the metallic shadow mask, dot emission is reflected from the metallic surface and can only be collected through the nano-aperture. With etched mesas, the optical quality of the dot emission is degraded due to interactions with surface states of the etched pillars. To enhance the count rate and minimize non-radiative recombination pathways of single self-assembled quantum dots, it is possible to fabricate samples in which the average distance between neighbouring quantum dots is larger than the optical spatial resolution [82]. However, such dot growth is a completely random process, as is the case for both mesa and nano-apertures and is not favourable for device applications. In addition, only a very small percentage (a few percent) of nano-apertures or mesas contain a single quantum dot. In order to significantly increase the yield and bring such experiments closer to large scale implementation within devices, it is necessary

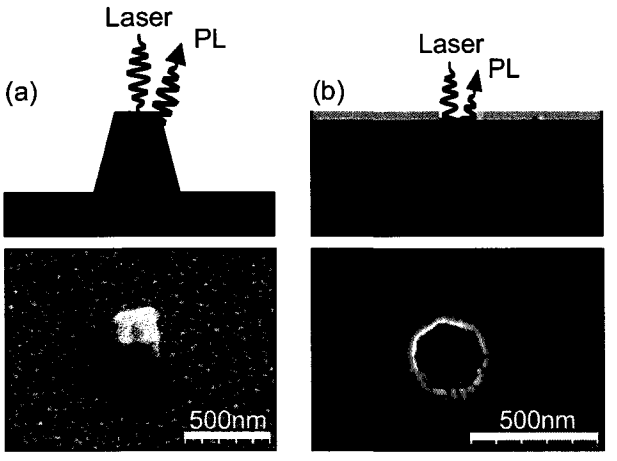

Figure 3.1: Current techniques for isolating conventionally grown single quantum dots for investigation: (a) sub-micron mesa (b) sub-micron nano-aperture.

to remove the random nature of the nucleation, so that individual quantum dots can be placed at known locations on the sample.

This chapter introduces a unique method, pioneered and developed at the Institute for Microstructural Sciences of the National Research Council, which overcomes the random nature of the nucleation process for self-assembled quantum dots and therefore achieves single quantum dot isolation without recourse to post-processing. The necessary control is achieved by utilizing a nanotemplate deposition technique, where the nucleation site of individual InAs/InP quantum dots can be precisely controlled. The advantage of knowing the exact location of each quantum dot is that control structures can be constructed around individual dots. In this thesis, the nanotemplate deposition technique is used to facilitate the construction of electrostatic gates around individual dots, so that vertical and lateral electric fields can be applied.

Two types of gated nanotemplate structures are studied, ridge nanotemplates and

pyramidal nanotemplates. Under the appropriate growth conditions, each ridge nanotemplate contains a linear array of individual dots, whilst each pyramidal nanotemplate contains a single quantum dot. Post processing is required to isolate a single quantum dot on a ridge, in a similar manner to nano-apertures utilizing a metallic mask, whereas on the pyramidal nanotemplate no post processing is required to isolate a single dot.

The remainder of this chapter is organized as follows. Section 3.1 introduces the standard, randomly driven growth process for conventionally grown, self-assembled quantum dots (Stranski-Krastanow mode). Section 3.2 discusses how the random nature of the nucleation site is removed by the nanotemplate deposition technique. Additional details about this dot growth are provided in the work of J. Lefebvre *et al.* [30]. In Section 3.3, the process of reaching the single dot regime on the nanotemplate is described, as well as the method of selecting individual quantum dots for electrostatic gating for both the ridge and pyramidal nanotemplates in this thesis. Finally, controlling the size and shape of the quantum dot utilizing the pyramidal nanotemplate technique is discussed in Section 3.4.

3.1 Growth of self-assembled quantum dots

It is important to understand self-assembled dot growth by strained layer epitaxy [52] in order to better describe the growth of deterministically positioned dots on the nanotemplate. Growth on the nanotemplate takes advantage of strained layer epitaxy. However, the nanotemplate removes the random nature of the nucleation process for quantum dot growth by directing the dot material to desired locations on the

semiconductor substrate. In semiconductor crystal growth both equilibrium and non-equilibrium, *i.e.*, kinetic and thermodynamic contributions are important. The kinetic component is concerned with the ability of atoms to move about on the crystal surface. In contrast, the thermodynamic component accounts for how these moving atoms on the crystal surface incorporate into the crystal structure. For example, each exposed crystallographic plane has a different surface energy associated with it due to the number and orientation of incomplete bonds. Atoms moving on the crystal surface during growth will tend to redistribute and incorporate into the crystal structure to minimize the total energy. This dynamic reordering of the crystal surface depends strongly on the type of epitaxy used, molecular beam epitaxy (MBE) or chemical beam epitaxy (CBE) for example, and also on the specific growth parameters used (*i.e.*, temperature, pressure, deposition rate, etc.).

The growth of self-assembled quantum dots on the semiconductor surface is a strain driven process. Strain is produced when attempting to grow a semiconductor material with a different lattice constant than that of the substrate (*e.g.*, for InAs on InP, the lattice mismatch is 3 %). That is, new material adjusts its lattice constant to fit the lattice constant of the underlying substrate. As the thickness, d, of the semiconductor overlayer increases, the strain between the two layers also increases. For growth on zincblende or diamond crystal structures on the (001) surface, the strain energy, E_{strain}, builds up as $E_{strain} = \varepsilon^2 d$ [84]. With increasing thickness of the strained layer, dislocations will occur if the lattice mismatch, ε, is too large [84]. However, under certain growth conditions, the 2D growth transitions to 3D growth and small 3D islands or dots are formed to minimize the strain preventing dislocations from occurring. This process is a tradeoff between the reduction in elastic energy and

increase in the surface energy due to 3D island growth and occurs when the energy cost to form the dots is the most favorable (*i.e.*, the reduction in elastic energy is larger than the increase in surface energy due to 3D island formation). The elastic energy is reduced in 3D island growth since the lattice constant of the material can relax somewhat and no dislocations form. In comparison, surface energy is proportional to growth surface area and increases when 2D growth switches to 3D growth. This transition from the original 2D growth (quantum well, known as the 2D wetting layer) to self-assembled quantum dot growth is known as the Stranski-Krastanow (SK) growth mode [85].

The process of strained layer epitaxy is summarized in Figure 3.2. Figure 3.2(a) gives a schematic view of the SK growth mode and Figure 3.2(b) depicts the corresponding total energy, E_{total}, as a function of the growth time, t_{growth}. The main components of the total energy consist of surface and elastic energy. Initiating growth with a semiconductor material that is lattice mismatched with the underlying substrate produces strain as the atoms attempt to match the lattice constant of the substrate. In this example, the lattice constant of the material being grown is larger than the substrate and leads to compressive strain. InAs on GaAs ($\varepsilon \sim 7$ %), and InAs on InP ($\varepsilon \sim 3\,\%$) are two examples of lattice mismatched materials for self-assembled quantum dot growth by strained layer epitaxy. This growth begins in two-dimensions as individual atomic layers are deposited and atoms redistribute about the surface to minimize the surface energy. This 2D growth is also known as the 2D wetting layer (WL). As each atomic layer is deposited (usually only a few atomic layers), the strain builds up in the semiconductor nanostructure, and the total energy increases with growth time. At a certain point, if another atomic layer were deposited, dislocations

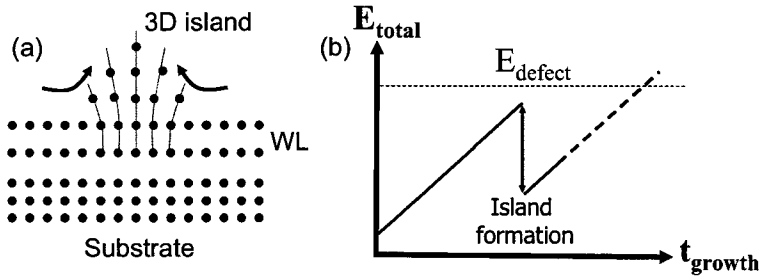

Figure 3.2: (a) Schematic view of single atoms in a single self-assembled quantum dot produced by the Stranski-Krastanow growth mode. In practice, a single quantum dot contains thousands of single atoms. (b) Total energy as a function of growth time, t_{growth}. The favourable configuration to minimize the total energy for lattice mismatched materials during epitaxial growth is the formation of 3D islands, which are known as self-assembled quantum dots.

would occur. Before this happens, however, the 2D WL growth makes a transition to 3D island growth and the lattice constant partially relaxes. This process marks an abrupt transition in the total energy as the elastic energy decreases. In addition, there is an increase in the surface energy due to 3D growth, which is the most favorable configuration as the increase in surface energy is less than the reduced elastic energy. The 3D islands are defect free and are known as self-assembled quantum dots. In practice, the quantum dot is capped with the substrate material for optical investigation.

An SEM micrograph of an uncapped sample of InAs self-assembled quantum dots grown by strained layer epitaxy on an InP substrate is shown in Figure 3.3(a). These dots were grown by chemical beam epitaxy. The dots that are formed present a major disadvantage for further investigation in that both the nucleation site and size of the quantum dot are completely random. These InAs quantum dots grown on InP (InAs/InP) are interesting, however, in that they can be tuned to emit in the telecommunications band around $1.55\,\mu$m ($\sim$ 800 meV). Figure 3.3(b) shows a

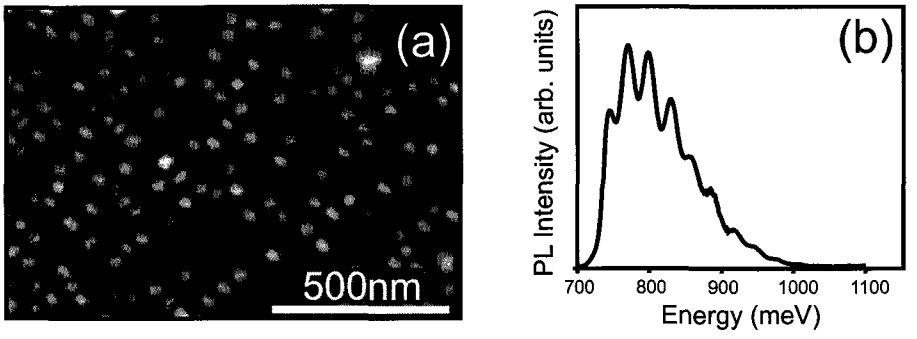

Figure 3.3: (a) Plan view SEM micrograph of InAs/InP quantum dots on a planar substrate grown by chemical beam epitaxy. The areal dot density is $\sim 100\,\mu\text{m}^{-2}$. (b) Typical PL from capped InAs/InP quantum dots on a planar substrate. The desired wavelength of $1.55\,\mu\text{m}$ ($\sim$ 800 meV) can be reached with this material system.

typical photoluminescence (PL) emission spectrum from InAs/InP quantum dots such as that shown in Figure 3.3(a). The observed PL spectrum is broad, reflecting the inhomogeneous broadening of the dot ensemble (*i.e.*, each quantum dot with different shape and size emitting at a different wavelength). On top of the inhomogeneous broadened PL signal are multiple peaks that correspond to single monolayer variations in the quantum dot height [83, 86]. Each peak represents a family of dots with the same quantum dot height. As the quantum dot height increases, the ground state emission of the dot redshifts (*i.e.*, moves to lower energy) allowing tuning in the vicinity of $1.55\,\mu\text{m}$, the desired wavelength for fiber based telecommunications.

3.2 Directed self-assembly

The directed self-assembly growth technique on the nanotemplate utilizes the Stranski-Krastanow growth mode as described in the previous section. However, in order to control the quantum dot nucleation site and parameters that affect the electronic structure such as the quantum dot size, it is preferable to direct the dot material to

desired locations on the substrate. Such control over the quantum dot position and electronic structure is crucial for scalability in any device application that employs quantum dots. Attempts to control the quantum dots size and nucleation site thus far have relied on some form of patterning prior to dot growth [31–39]. In most of these growth methods, the quantum dot is typically grown close to the etched regions of the patterned substrate, which therefore affects the optical quality of the dot emission [39]. The dot emission is broader and weaker than conventionally grown dots due to the presence of non-radiative pathways from defects at the growth interface and a fluctuating charge background when these defects trap additional carriers [39]. In contrast to these conventional growth methods, the nanotemplate deposition technique is unique in that the nanotemplate provides a clean, defect free surface for dot nucleation and therefore does not affect the optical quality of the dot as confirmed by both theoretical [40] and experimental investigations [8, 29].

The nanotemplate takes advantage of the facet-dependent surface migration of adatoms by directing the dot material to desired locations on the substrate [30, 68]. The deposited dot material therefore migrates off the facets with longer migration lengths and incorporates into facets with shorter ones. To produce the desired facets, it is necessary to select a pattern that produces edges in alignment with certain crystal directions. The size of the pattern then controls the dot lateral size, while the amount of deposited material controls the dot height [30].

The directed self-assembly process for InAs dots on InP for a ridge nanotemplate of 'stripe' geometry is illustrated schematically in Figure 3.4. In the first step, Figure 3.4(a), an oxide covered (SiO_2), (001)-oriented InP wafer is patterned by e-beam lithography and then wet etched to produce openings in the oxide that are aligned

with the [100] crystallographic direction and which expose the underlying substrate. Critical to nanotemplate fabrication is that the growth is selective and the deposited material only grows on the exposed areas of the underlying InP substrate and not on the SiO_2 mask. The selective growth is achieved by chemical beam epitaxy with trimethyl-indium and cracked AsH_3 and PH_3 sources. Growth begins when deposited InP material incorporates into exposed areas of the InP substrate and proceeds by migrating off the {110} side-facets and further incorporating into the top (001) surface. Such integration occurs since the higher index facets are known to have a longer migration length than the top (001) surface [30]. The result is high-quality, atomically clean {110} crystallographic side-facets and top (001) surface that can be used for InAs quantum dot growth. As growth proceeds, the top (001) diminishes until reaching the desired dimensions of width, w, for dot growth as shown in Figure 3.4(b). Immediately following the growth of the InP nanotemplate, InAs material is deposited for dot formation on top of the nanotemplate. The dot material migrates onto the top (001) surface in the same fashion as the InP and now dot nucleation proceeds according to the Stranski-Krastanow growth mode as described in the previous section (shown in Figure 3.4(c)), although now there is a smaller area available for growth on the nanotemplate. This method of directed self-assembly achieves the desired result since dot material is directed to known locations on the substrate as determined by the patterning. Typically, a sub-critical amount of InAs is required in comparison with conventionally grown dots on planar substrates, since the dot material is deposited on the top (001) surface of the nanotemplate in addition to being collected from the {110} sidewalls. Finally, the dots are capped with InP for optical characterization, as shown in Figure 3.4(d).

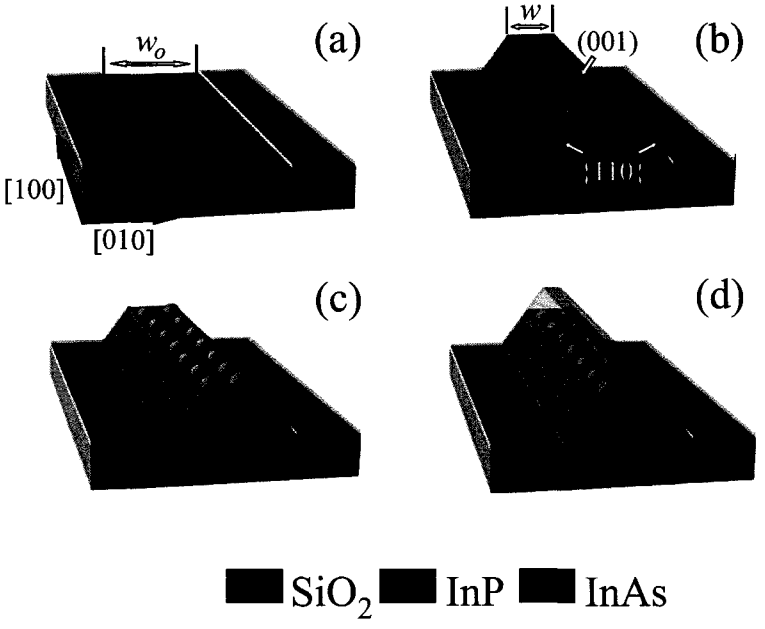

Figure 3.4: Schematic view of directed self-assembly process for InAs quantum dots on ridge nanotemplates: (a) patterned substrate with openings in the SiO_2 mask. (b) InP ridge nanotemplate with atomically smooth (001) top surface available for quantum dot growth. (c) InAs self-assembled quantum dots on the nanotemplate. (d) capped dots for optical characterization.

Structural characterization of uncapped quantum dots is performed to obtain the optimum growth conditions to reach the single dot regime on the nanotemplate. This step must be completed before optical characterization of InAs/InP quantum dots is carried out to select individual dots for electrostatic gating. For structural characterization, an InP substrate is patterned with varying starting base widths, w_0. The sample is then subjected to the directed self-assembly process. By selecting an appropriate base width in combination with the deposition of a sufficient amount of dot material, it is possible to achieve a single row of quantum dots at the apex of ridge nanotemplates. Once the optimal growth conditions necessary to obtain single quantum dots have been determined, a new wafer with identical growth conditions is

fabricated and then capped for optical characterization. Capping the quantum dot modifies its size and shape and directly affects its electronic structure and the optical properties of the dot emission. Optical spectroscopy is necessary to ascertain the single dot regime since the capping process modifies the dot size (see Section 3.3).

SEM images of real nanotemplate structures of ridge geometry with varying base widths, w_0, produced under identical growth conditions are shown in Figure 3.5. Since the ridge nanotemplates are subject to identical growth conditions, larger starting base widths will result in a wider area available for quantum dot growth. If the ridge is sufficiently wide, dots are randomly distributed on top of the ridge in a similar manner to conventionally grown dots on planar substrates, as shown in Figure 3.5(a). As the top (001) surface, w, of the nanotemplate narrows, the dot growth is affected in two ways. First, the top width of the nanotemplate confines the area for growth. When the lateral dimensions are significantly reduced, the quantum dots will order on the top apex as to minimize the strain. The randomly distributed flat dots as shown in Figure 3.5(a) will transition to a double ordered dot array as shown in Figure 3.5(b). By reducing the ridge base width further, the lateral dimensions of the ridge (001) apex can only support a single row of quantum dots as shown in Figure 3.5(c). The lateral dimensions of the dots shown in Figure 3.5(c) are approximately 30-40 nm. Second, the amount of dot material (InAs) deposited on the top (001) surface is enhanced as the ratio of w_0/w increases. This corresponds to an increase in the quantum dot height as inferred by the enhanced contrast of the SEM images from Figures 3.5(a)-(c).

The geometry of the ridge nanotemplate can be modified to square-based templates by varying the oxide patterning. Square based openings in the oxide aligned

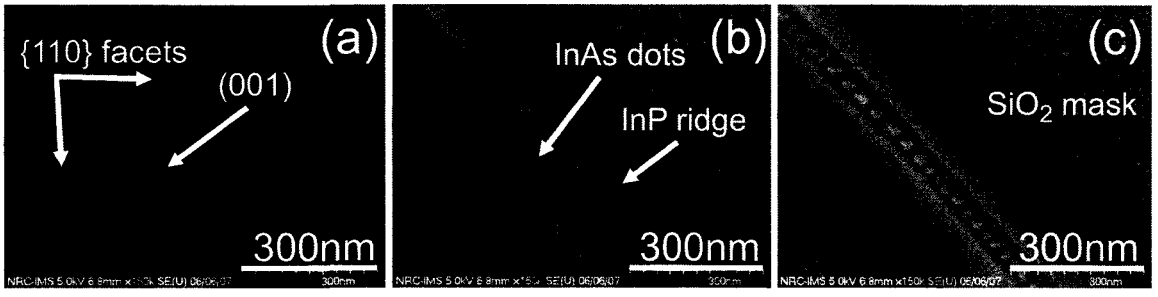

Figure 3.5: Plan view SEM images of uncapped ridge nanotemplates with varying base widths: (a) $w_0 = 390\,\text{nm}$, (b) $w_0 = 335\,\text{nm}$, and (c) $w_0 = 325\,\text{nm}$. The top (001) surface lateral dimensions reduces with decreasing ridge base width until only a single row of quantum dots is obtained. The top widths are: (a) $w_0 = 190\,\text{nm}$, (b) $w_0 = 90\,\text{nm}$, and (c) $w_0 = 50\,\text{nm}$, respectively.

along [100] and [0$\bar{1}$0] crystallographic directions produce a pyramid geometry with four dominant sidewalls comprised of {110} planes. Figure 3.6(a) shows the four dominant sidewalls that are produced for such a square-based nanotemplate, while in Figure 3.6(b), a side-view SEM image portrays the pyramid geometry that results from the square-based nanotemplate. The pyramid geometry is a direct result of the deposited material migrating off the four dominant {110} sidewalls onto the top (001) apex. Similarly to ridges, the starting base width of the pyramidal nanotemplate is modified incrementally until the single dot regime is reached. SEM images of pyramidal or square-based nanotemplates with varying base widths are shown in Figure 3.6(c)-(e). In larger square based pyramidal templates, the apex contains multiple dot clusters (Figure 3.6(c)). As the the top (001) apex is reduced, only a few dots (*i.e.*, four) are observed (Figure 3.6(d)). The apex is further reduced until its lateral dimensions support only a single quantum dot. A pyramidal nanotemplate, which has reached the single quantum dot regime, is shown in Figure 3.6(e). In contrast to

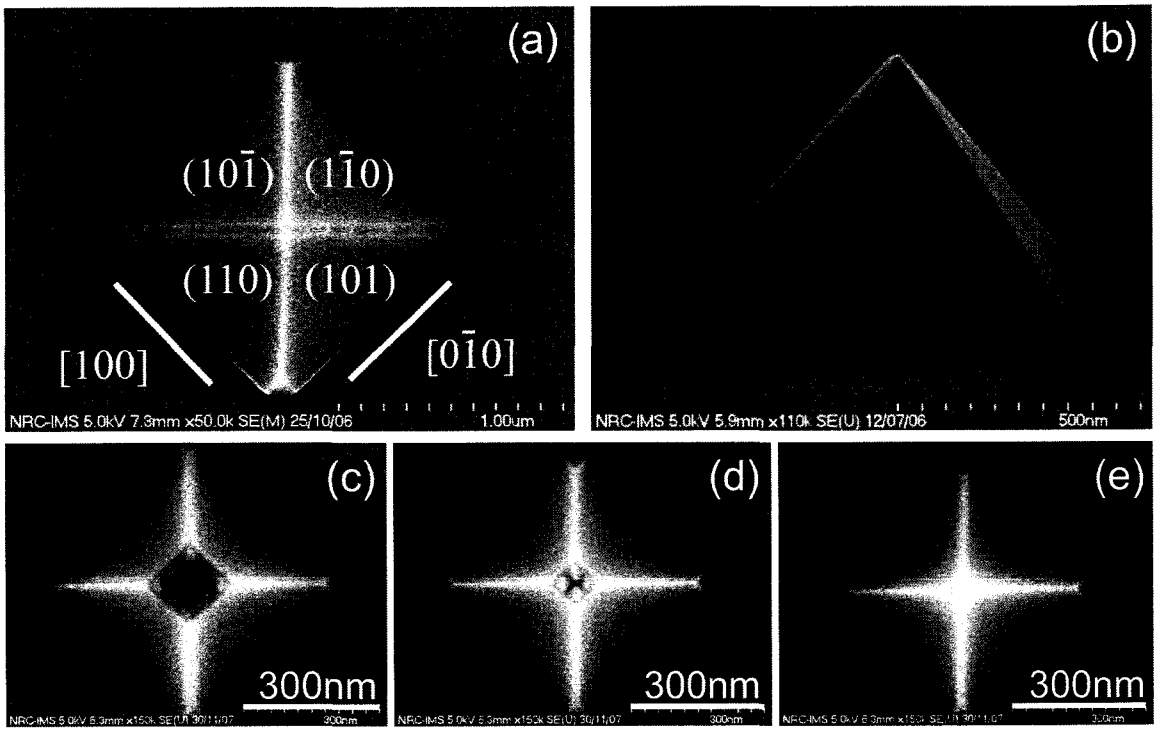

Figure 3.6: Upper panel SEM images of completed square-based pyramidal nanotemplates oriented along the [100] and [0$\bar{1}$0] crystallographic directions: (a) plan view and (b) cross-section. Lower panel plan view SEM images of uncapped pyramidal nanotemplates with varying base width: (c) $w_0 = 390\,\text{nm}$, (d) $w_0 = 370\,\text{nm}$, and (e) $w_0 = 358\,\text{nm}$. The single dot regime is obtained for the pyramidal nanotemplate in (e).

ridges, no further processing is required to isolate this single quantum dot for optical studies or device applications since the spacing of nanotemplates are completely selective and determined by the design layout.

The dot growth on pyramidal nanotemplates proceeds similarly to ridges, although the pyramid geometry provides an additional degree of lateral spatial confinement and control. Small increments in the square based opening ($\sim 2\,\text{nm}$ steps), enables control of the lateral dot dimensions, as evidenced from both structural studies shown here in Figure 3.7 and confirmed by optical characterization described in the following

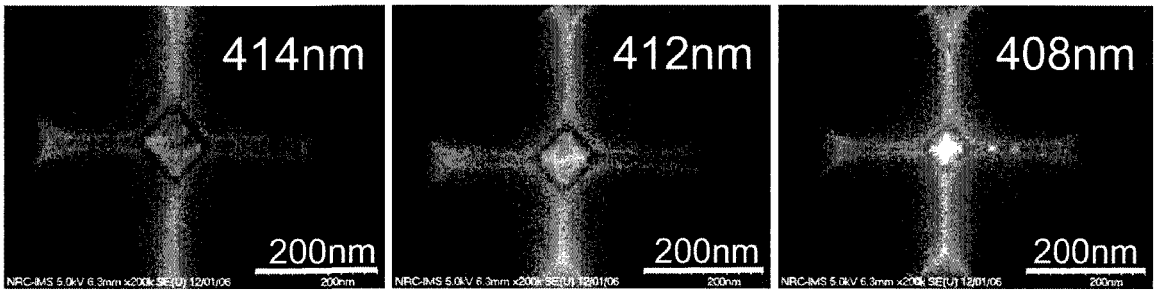

Figure 3.7: Quantum dot size control on pyramidal nanotemplates applying small decrements in the base width dimensions of the pyramid. The corresponding base width of the pyramids are shown in the inset of the SEM image.

section. A clear reduction in the quantum dot size is evident in the corresponding SEM images as the pyramid base width decreases.

3.3 Single dot isolation

This section describes the process of selecting individual dots on both ridge and pyramidal nanotemplates that are used for electrostatic gating in this thesis. Optical spectroscopy was chosen as the experimental method to select individual dots on the nanotemplate. Details of the optical spectroscopy methodology are provided in Chapter 4 in which the dots are studied in emission (*i.e.*, photoluminescence). The optical emission from individual dots provides important information such as emission energies and energy level spacings of the underlying electronic structure [63]. Moreover, the optical signature from an individual nanotemplate structure ascertains whether there is emission from only a single quantum dot or more than one. A clear indication of reaching the single dot regime on the nanotemplate is the observation of a single, sharp emission line under low excitation powers. The observed single emission peak results from recombination of a single exciton (bound electron-hole pair) which has populated the quantum dot s-shell during the excitation process. The linewidth

of the optical transition from a single dot is limited by the recombination lifetime of the exciton. Typical recombination lifetimes for the excitonic ground state of approximately 1 ns are observed [82], which corresponds to a linewidth in the order of 1 μeV. Observed lifetimes that are limited only by radiative recombination pathways is referred to as intrinsic broadening [1].

Optical spectroscopy is performed on capped dots with similar growth conditions to that as the uncapped samples, which have been determined to contain single dots. These optical measurements are necessary since the capping process is known to modify the shape and size of the dot for InAs/InP quantum dots due to As/P exchange processes [87]. Therefore, it is expected that the base width of the nanotemplate required to obtain single dots on capped samples will be different to that of uncapped samples. The selected dots are then sent for further processing to precisely position electrostatic gates around individual dots.

3.3.1 Ridge nanotemplate

Photoluminescence (PL) from ridge nanotemplates of varying base widths, grown under identical growth conditions, is shown in Figure 3.8(a). Large base widths (350 nm), which are expected to have many dots, exhibit broad PL emission centred about 1450 nm. This broad emission is caused by an ensemble of dots on top of the ridge with dissimilar shape and size resulting in different wavelength emissions. Decreasing the base width of the ridge shifts the dot emission towards the telecommunications wavelength of 1550 nm. The PL red shift with decreasing base width is expected due to an increase in quantum dot height. The quantum dot height increases since more dot material is available for growth on the top (001) apex of the ridge as the top width is reduced. In addition to the PL red shift, there is an

observed narrowing of the PL emission and strong reduction in the PL intensity since the number of dots probed is reduced with the decreasing ridge width. The narrowing of the quantum dot PL is also attributed to the dot uniformity as the dot material redistributes about the ridge apex to minimize the strain. This leads to ordered arrays of dots with similar lateral dimensions limited by the top width, and which emit at similar wavelengths. Further reduction in the ridge base width results in the loss of quantum dot emission (data not shown). At this point, the ridge is complete and the top apex is unable to accommodate any dots. PL from completed nanotemplates is discussed in further detail in the following section.

In order to isolate a single dot on a ridge structure, as shown in the lower panel of Figure 3.8(a), further processing is required. However, in contrast to the nanoapertures discussed previously, dot placement on ridge nanotemplates is deterministic and electrostatic gates can be precisely positioned around them. The metallic mask is created by depositing two Schottky gates, defined by e-beam lithography, on top of the ridge. Typical gate spacings fabricated for this thesis are of the order of 300 nm (see SEM image in the lower panel of Figure 3.8(b)). The metallic gates serve two purposes. First, the narrow gap allows the isolation of a single dot if the dot density on top of the ridge is sufficiently low. Second, by producing a potential difference between the two top Schottky gates, a lateral electric field may be applied along the ridge direction.

Figure 3.8(b) demonstrates the PL of gated ridges taken from the same sample as the ungated ridges (*i.e.*, ridges subject to identical growth conditions, but different location on the same wafer). The effect of the gates on the PL spectra is evident. Ungated ridges exhibit broad emission consisting of many peaks (Figure 3.8(a)), while

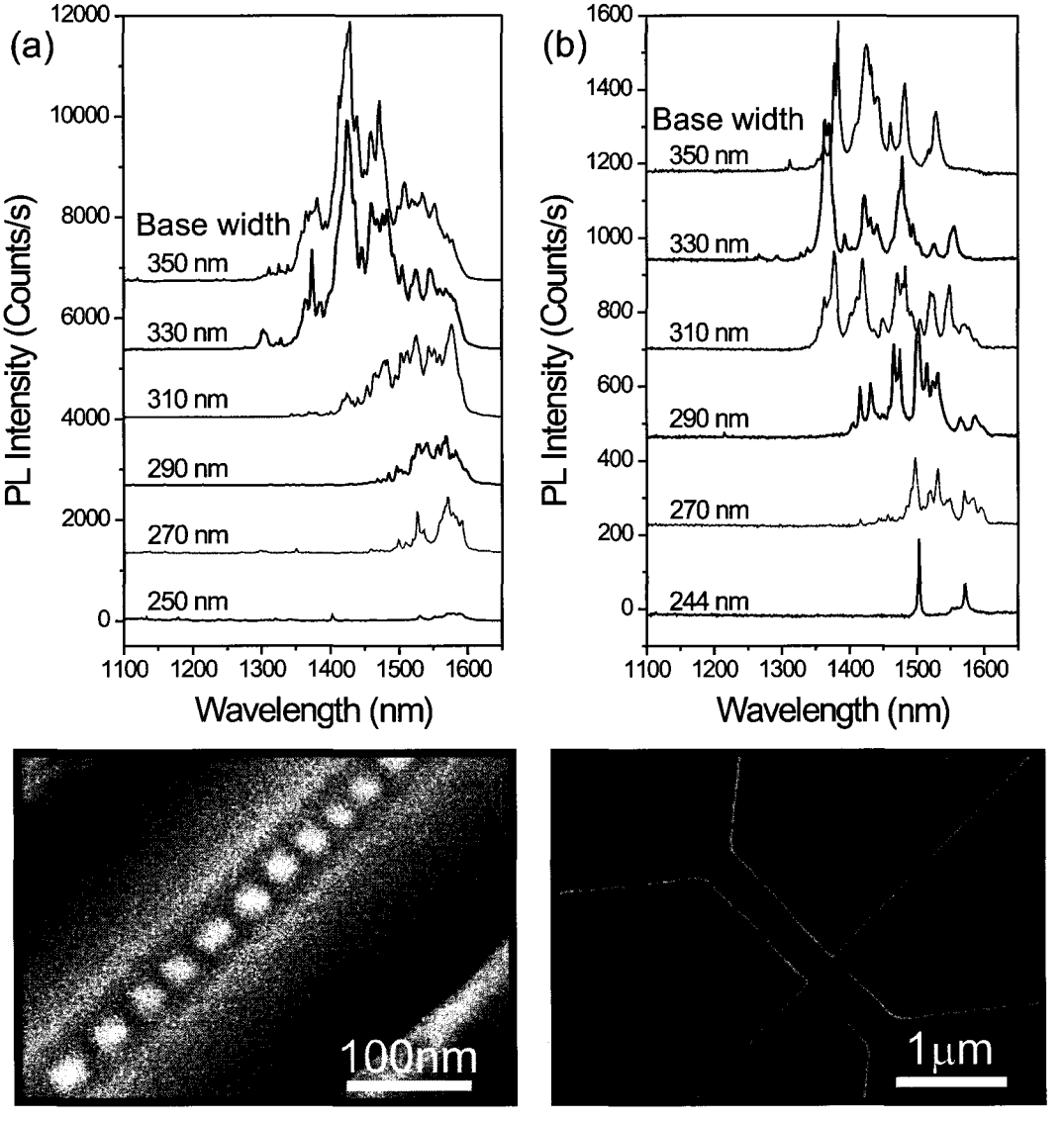

Figure 3.8: Upper panel: Quantum dot PL for series of ridge nanotemplates with varying base width for (a) ungated ridges, and (b) gated ridges. Note that the optical spectra is presented with an offset for clarity of presentation. Lower panel: Plan view SEM images of measured ridges corresponding to upper panel. The images shown here were selected with arbitrary ridge base width. The ungated ridges are capped for optical measurements.

gated ridges manifest as discrete emission peaks with reduced number (Figure 3.8(b)). The difference in the observed emissions results from a reduction in the number of dots probed in the narrow gap of the gated ridge as compared to the ungated ridge with identical base width. The reduction in dots probed also corresponds to an order in magnitude reduction in the PL intensity. In both gated and ungated ridges, the PL emission red shifts to higher wavelength with decreasing ridge base width. Note that the optical spectra presented here are offset along the y-axis with increasing ridge base width for clarity of presentation and is not due to an increasing background.

Study of smaller gated ridges (244 nm), in which only a single row of dots can be supported, reveals two sharp emission lines. Each emission peak corresponds to an individual dot and can be spectrally isolated with a higher resolution spectrometer. Single dot isolation is confirmed by performing state-filling spectroscopy on the observed individual emission peaks [8]. The optical signature of single quantum dot emission is the observation of multi-exciton states (two or more electron hole-pairs) with increasing pumping power [29, 40, 63, 80]. Such PL emission observed in Figure 3.8(b) is typical of the gated ridges studied in this thesis and is suitable for studying individual quantum dots as a function of lateral electric field.

3.3.2 Pyramidal nanotemplate

Pyramidal nanotemplates have an advantage over ridges since no further processing is required to isolate a single quantum dot. For device applications, the additional lateral constraint added to the pyramid apex provides the ability to control the shape and size of the dot and therefore the emission energy. The single dot isolation technique presented here is unprecedented since control of the quantum dot nucleation site is deterministic and defined by the location of the nanotemplate. In addition, the

high optical quality of the dot is maintained while emitting in the telecommunications band of 1.55 μm. The yield of quantum dot emission for pyramidal nanotemplates is a significant improvement over random-based methods. Approximately 80 % of the pyramids studied in this thesis exhibit single excitonic emission, of which about 20 % were suitable for further study in electric fields due to insufficient yield of the processed electrical gates.

The excellent optical quality of dots on pyramid nanotemplates is demonstrated by the high signal to noise ratios obtained for a single excitonic emission in Figure 3.9(a). The reproducibility of single dot isolation for square-based templates is evident in Figure 3.9(a), as eleven dots emitting in the wavelength range from 1500 nm to 1600 nm are shown. Typical count rates for the single dots shown here are approximately 1000 counts per second for the excitonic ground state. This data is compared with other gated individual dots in III-V materials in which count rates of 1000 counts per minute are possible for the quantum dot ground state [7]. Count rates for gated pyramids containing individual quantum dots are unaffected if the gates are sufficiently spaced. The PL emission of the single dots shown here are representative of those selected for electrostatic gating.

To select individual dots on pyramid nanotemplates, it is important to identify single pyramids which exhibit only a single excitonic emission. Single dots are identified by measuring the PL of a series of pyramids with varying base widths of the template (opening in the oxide). Similar to ridges, the PL red shifts with decreasing pyramid base width corresponding to an increase in quantum dot height. In contrast however, no further processing is required to observe sharp emission lines in the PL due to individual dots.

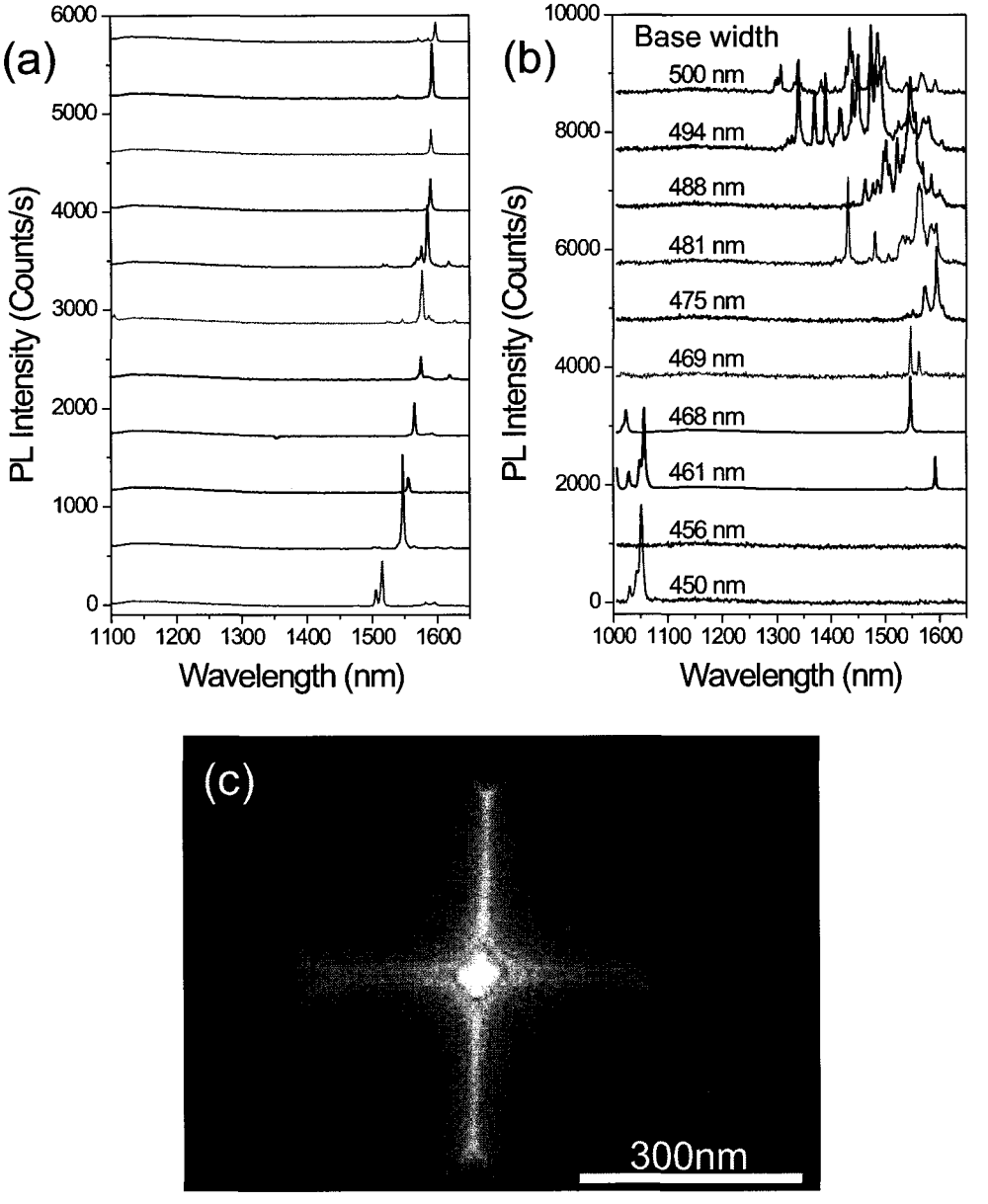

Figure 3.9: (a) Typical PL of selected individual InAs/InP quantum dots for electrostatic gating. Count rates for a single quantum dot shown here under low power excitation conditions (1 μW) range from approximately 200 counts per second to approximately 1000 counts per second. (b) Quantum dot PL for series of pyramid nanotemplates. Single dots are ascertained by the observation of a single, resolution limited peak in PL, immediately before the pyramid completes where no PL is observed. PL spectra are offset along the y-axis for clarity of presentation. (c) Plan view SEM image of uncapped pyramid nanotemplate containing an individual InAs/InP quantum dot. The sample is capped for PL measurements.

PL from pyramid nanotemplates as a function of decreasing base width is shown in Figure 3.9(b). Beginning with the largest base width of the pyramid nanotemplate (500 nm), multiple dot clusters are expected due to the previously studied uncapped dots characterized by structural analysis. Here, a series of sharp emission lines ($\sim$10) are observed and are attributed to single exciton emission lines from individual dots of the nanotemplate. For small decrements in the pyramid base width, the number of observed emission lines is reduced, corresponding to a smaller number of individual dots on the nanotemplate. In pyramid base widths of 475 nm and 469 nm, pairs of emission lines are observed, which is attributed to pairs of dots on the nanotemplate. Decreasing the pyramid base width further results in the observation of a single, resolution limited peak (0.25 meV linewidth), a clear optical signature of isolating a single quantum dot. In the data presented here, single dot emission is observed for nanotemplates with base widths of 468 nm and 461 nm, respectively.

After single dot isolation has been achieved, a small decrease in the pyramid base width to 456 nm results in no observed PL emission. Here, the pyramid apex closes and the deposited dot material incorporates into the larger surface area of the {110} sidewalls as a thin wetting layer. Thus, the PL emission is not detected over the wavelength range of the InGaAs detector. For pyramid base widths smaller than 456 nm, wetting layer emission appears once again. The reappearance of the wetting layer emission in the detector range may be due to the incorporation of deposited dot material into the {111} sidewalls as overgrowth of the pyramid occurs (overgrowth not shown here).

3.4 Quantum dot size control on the nanotemplate

Square-based pyramidal nanotemplates allow the possibility to control the size of the quantum dot in addition to controlling its nucleation site. The height of the dot is controlled by the amount of material deposited while the lateral dot dimensions are determined by the apex of the nanotemplate. Lateral size control of quantum dots on pyramidal nanotemplates is demonstrated by studying very small increments in the pyramid base width ($\sim$2 nm) in which the single dot regime has been reached. Following the procedure for selecting individual dots on pyramid-based nanotemplates as described in the previous section, the best dot was selected out of a series of ten pyramid repeats with nominally identical base widths as determined by the oxide patterning.

Results of the PL from selected dots as a function of small increments in the pyramid base width are shown in Figure 3.10(a). The observed PL emission shifts to higher energy for decreasing pyramid base width, in contrast to the red shift (lower energy) obtained previously. The observed red shift was due to large decrements in the pyramid base width corresponding to an increase in quantum dot height. Here, the corresponding shift to higher energy with decreasing pyramid base width can be explained by a decrease in the lateral dimensions of the dot as the top apex is reduced. This effect of the lateral dot dimensions that influence the lateral confining potential and therefore the dot emission energy is shown schematically in the inset of 3.10(b). Figure 3.10(b) exhibits the extracted peak positions of the observed single exciton emission from Figure 3.10(a) as a function of the pyramid base width. A correlated dependence of dot emission energy with decreasing base width is obtained

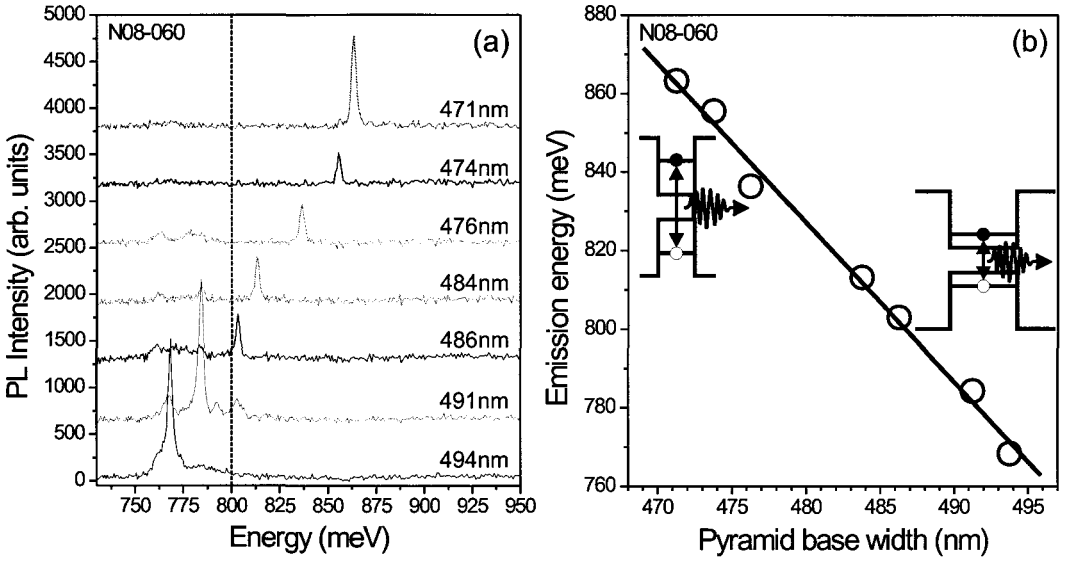

Figure 3.10: (a) PL of individual InAs/InP quantum dots as a function of small increments in the pyramid base width. The PL is tuned through the telecommunications wavelength of 1.55 μm (dotted line at 800 meV). PL spectra are offset along the y-axis for clarity of presentation. (b) Extracted peak positions of single exciton emission from (a) as a function of the pyramid base width. Small increments in the pyramid base width leads to a corresponding shift of the observed PL to lower energy. In this case, the correlated shift of the PL with pyramid base width is attributed to control of the lateral size of the dot. The effect of lateral dot dimensions on the emission energy is shown in the inset (represented schematically by a quantum well).

suggesting that it is possible to control the lateral dimensions of the dot with appropriate choice of patterning in the oxide. For this particular sample, it was possible to tune the emission energy over a wide energy range from 760 meV to 860 meV for only a 20 nm change in the pyramid's base width dimensions. Of particular importance for fibre based applications is the ability to tune the quantum dot emission through the telecommunications wavelength of 1.55 μm (800 meV). The telecommunications wavelength of 1.55 μm is achieved for a pyramid base width of approximately 487 nm. Control of the lateral dot dimensions that affect the dot emission energy is confirmed

by structural analysis for small decrements in the pyramid base width as shown previously in Figure 3.7 (samples constructed under similar growth conditions as the ones presented here). Here, SEM images show that small decrements in the pyramid base width correspond to a decrease in lateral dot dimensions.

Chapter 4

Experimental methodology

This thesis utilized micro-photoluminescence (micro-PL) as the main optical spectroscopy method used to characterize the gated, single InAs/InP quantum dots. Micro-PL provides important information on the electronic structure and optical properties of a single quantum dot. Comparison to theoretical calculations in an applied electric field and varying excitation power and polarization provides the ability to identify all of the observed spectral lines in PL since each exciton complex corresponds to a unique optical spectrum (*i.e.*, Stark shift, fine-structure, life time, power and polarization dependence *etc.*). As an example, identification of spectral lines in a micro-PL experiment is crucial for the practical implementation of entangled photon pairs based on the biexciton-exciton radiative cascade [27] (see Chapter 7) or identification of charge states in an applied vertical electric field (see Chapter 8).

4.1 Photoluminescence spectroscopy

A schematic view of the micro-PL setup utilized in this thesis is shown in Figure 4.1. A series of mirrors (M1, M2, MC) are used to direct the laser light to the sample residing

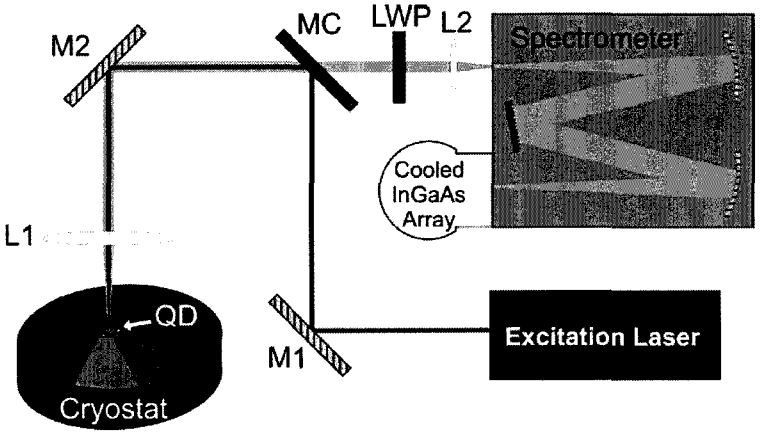

Figure 4.1: Schematic view of micro-photoluminescence setup used for characterization of gated, single quantum dots in this thesis (see text for details). Taken from [88].

in a continuous flow He-cryostat. The setup used a cold MC (MC) mirror to reflect visible light and transmit photons in the infrared. To excite only a single quantum dot, a high numerical aperture (NA) microscope objective (labeled L1 in Figure 4.1) focuses the laser light onto the sample. The current setup is designed such that the laser spot approaches the diffraction limit of the Helium-Neon laser ($\sim 1\,\mu$m) ensuring only a single quantum dot is subject to light illumination. The emitted photons from the quantum dot are collected through the same microscope objective and directed towards a single grating spectrometer for analysis of the emission spectrum. Along the optical path to the spectrometer is a long wave-pass (LWP) filter used to filter out the excitation laser from detection. The lens in front of the spectrometer (L2) is utilized to increase collection efficiency of the optical setup through NA matching of the spectrometer.

Detection of the emitted photons is achieved using a liquid Nitrogen cooled InGaAs diode array after spectral dispersion in a 0.25 m single grating spectrometer with a 600 grooves/mm grating that provides a spectral resolution of approximately 0.25 meV.

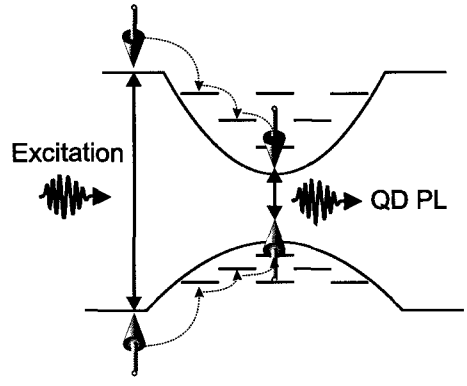

Figure 4.2: Schematic view of photoluminescence spectroscopy measurement process.

With this current setup, fine-structure splittings of $\sim 40\,\mu$eV could be resolved by polarization dependent spectroscopy when using a Lorentzian line fitting procedure as presented in the work of Geradot et al. [47]. The polarization of the emitted photons was analyzed by rotating a half-wave plate in front of a fixed Glan Thompson polarizer at the input of the spectrometer [42]. When better spectral resolution than 0.25 meV was required, a double grating spectrometer providing $\sim 50\,\mu$eV resolution was utilized. Unless otherwise stated, all measurements in this thesis were performed at a temperature of 4.2 K using non-resonant, above bandgap excitation (633 nm) and the PL was collected for an integration time of 10 s with the InGaAs detector. Note that for clarity of presentation throughout the thesis, optical spectra are presented with a constant offset along the vertical axis as in Figure 4.3 or as a contour plot.

The excitation source used in the measurements of this thesis is non-resonant, above bandgap excitation (633 nm). Electron-hole pairs are generated in the bulk InP surrounding the quantum dot (see Figure 4.2). The excited electron-hole pairs quickly relax (picosecond timescale) to the lowest energy of the system where they bind together to form an exciton due to their mutual Coulomb attraction. After

approximately $\sim 1\,\text{ns}$, the exciton recombines radiatively emitting a photon at lower energy than that of the excitation photon. Thus, PL probes the ground state emission of the quantum dot. In order to probe higher energy level states in the dot, power-dependent PL spectroscopy is utilized [80]. Here, higher excitation power leads to an increasing number of electron-hole pairs (excitons) confined in the quantum dot. The excitons recombine in a cascade process with each photon emitting a unique energy spectrum due to strong Coulomb interactions of the confined carriers in the quantum dot.

4.1.1 Power dependent photoluminescence spectroscopy

Power dependent PL spectroscopy using non-resonant excitation provides information about average number of excitons in the dot [80, 89–91] while polarization of the emission is used to confirm assigned excitonic transitions [44, 45, 89–91]. Typical single dot PL as a function of increasing excitation power at zero electric field for an InAs/InP dot on a nanotemplate is shown in the left panel of Figure 4.3. At low excitation power, only a single emission peak is observed attributed to recombination of a single exciton X involving a single electron-hole pair in the quantum dot s-shell. Increasing the excitation power modifies the average exciton occupancy of the dot. The biexciton (XX) corresponds to recombination of an exciton in the quantum dot s-shell in the presence of an additional electron-hole pair. Finally, p-shell emission is observed when the s-shell is completely filled. Recombination from the p-shell corresponds to on average of three or four excitons confined in the quantum dot. Concomitant with observation of p-shell emission are satellite peaks about the X and XX line due to s-shell recombination perturbed by the presence of excitons occupying higher lying states in the the p-shell [92].

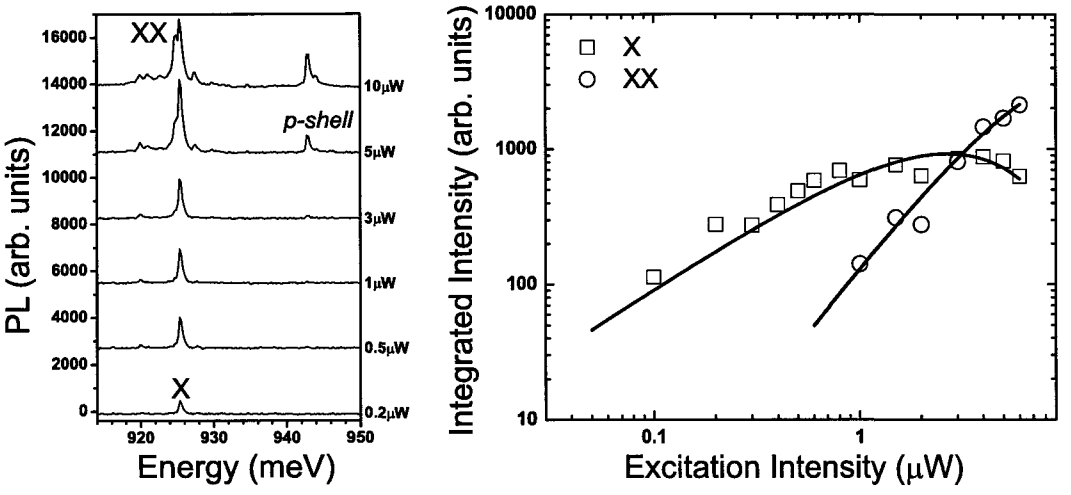

Figure 4.3: Left panel: Typical state-shell filling spectroscopy of single quantum dot on a ridge nanotemplate at zero electric field. Right panel: Fit to the data using Equation 4.1 (solid lines). Evidence of exciton and biexciton are inferred from the resulting linear and superlinear power dependence of integrated intensity on excitation power. The saturation of the observed emission peaks are well reproduced within the random capture model.

The assignments of X and XX transitions in Figure 4.3 are determined within the random capture model by fitting the integrated intensity of the emission peaks as a function of excitation power, N, which is then proportional to $P(\mu, N)$ as described in Equation 4.1. This fit of the data is carried out in the right panel of Figure 4.3 on a log-log plot. Excellent fits are obtained when assuming an average exciton occupation in the dot of $\mu = 1$ (black line) and $\mu = 2$ (blue line) corresponding to X, and XX, respectively. Thus on a log-log scale the dependence of the integrated intensity on excitation power is expected to be linear for the X line while quadratic for the XX line. Moreover, the saturation of both X and XX observed in experiment is well described by the exponential decay term in Equation 4.1 for increasing power, N.

Due to the random nature of the excitation and capture process into the dot under non-resonant excitation, the probability $P(\mu)$ to have a configuration with μ excitons

is given by a Poisson distribution [92, 93]:

$$P(\mu, N) = \frac{N^{\mu} exp(-N)}{\mu!}, \tag{4.1}$$

where N is the average exciton occupation in the quantum dot. Experimentally, N corresponds to the applied excitation power (*i.e.*, $Power \propto N$). With increasing excitation power, the probability that the number of excitons captured in the dot also increases. From Equation 4.1, the maximum probability to have exactly one exciton ($\mu = 1$) corresponds to on average, an occupation number of $N = 1$. In addition, however, for identical excitation power ($N = 1$), there is also finite probability of finding two excitons ($\mu = 2$) of almost 20 % and an even smaller probability (less than 1 %) to obtain three excitons ($\mu = 3$). This statistical nature of the quantum dot occupation using non-resonant excitation makes it possible to identify the exciton and biexciton transitions since more than one excitonic state can be observed in emission at a given excitation power. The excitons consequently recombine in a cascade process and emit a unique optical spectrum dependent on the dot occupancy [63]. Thus, in experiment, the average number of excitons occupied in the dot is probed by power dependent PL spectroscopy using above bandgap, non-resonant excitation. Here, the integrated intensity of the observed emission peak is proportional to $P(\mu, N)$ [93]. Within this simple model, also known as the random capture model, the intensity of the exciton (X) and the biexciton (XX) peak is proportional to $P(1, N)$ and $P(2, N)$, respectively which allows these optical transitions (X and XX) to be readily determined [93, 94].

This dependence on integrated intensity as a function of increasing excitation power is consistent with solutions of the coupled rate equations which takes into account the formation rate of exciton and biexciton and their relative lifetimes [92].

The rate equation model predicts a linear and and quadratic dependence for X and XX, respectively, when the ratio of the exciton lifetime, τ_1, to biexciton lifetime, τ_2, is $\tau_1/\tau_2 = 2$. Although the scientific community commonly accepts the value of $\tau_1/\tau_2 = 2$, deviations from the accepted value of 2 have been calculated and measured [94,95]. One possibility for deviation from the accepted value of 2 occurs for increasing dot diameter [94,95]. As an example, in the InGaAs/GaAs quantum dot material system, a dot diameter of 30-40 nm corresponds to an expected superlinear dependence for the XX of somewhere between 1.6 and 1.8. Such a dependence for the XX peak is usually measured for the experimentally investigated InAs/InP quantum dots studied in this thesis with similar lateral dot dimensions. In certain cases, however, a quadratic dependence of XX is measured which implies a smaller dot diameter; a parameter which is directly controlled by the top apex of the pyramidal nanotemplate (see Chapter 3). Further details of the rate equations based on a four level exciton-biexciton model are found in Refs. [96,97].

4.2 Electrostatic gating

To apply electric fields at cryogenic temperatures, a He continuous-flow cryostat was modified for electrical access. The left panel of Figure 4.4 shows the design of the cold finger for easy loading and un-loading of samples. To form devices for application of electric field at low temperature, the sample consisting of individual, gated InAs/InP dots was processed further by attaching the sample to a standard 8-pin ceramic carrier. Electrically conductive, silver epoxy (Epotek H31) was used to attach the sample to the ceramic carrier while the contacts were bonded ultrasonically with low-impedance gold wire. The back contact is electrically isolated from the cold finger

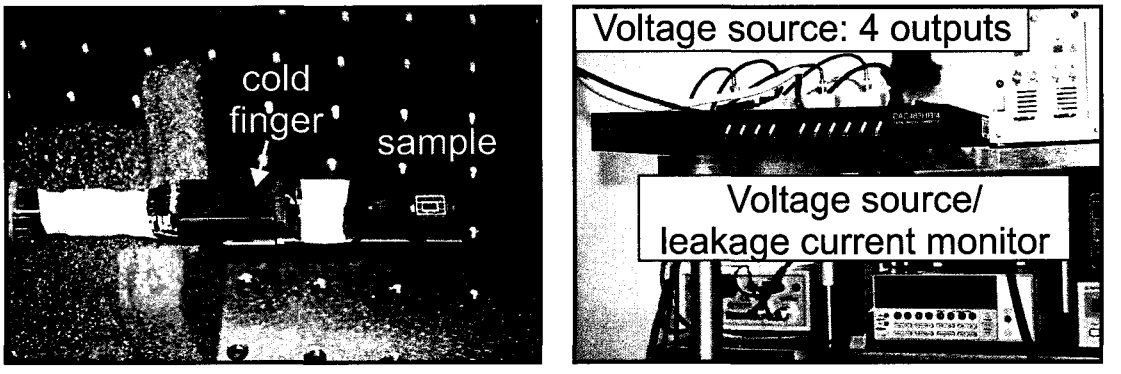

Figure 4.4: Left panel: Electrical access to individual dot on cold finger used to reach 4.2 K in a He continuous-flow cryostat. The spacing between holes in the optical table is one inch. Right panel: IOTECH voltage source with four outputs. A Keithley 6517 high resistance electrometer was used to monitor the leakage current during device operation.

via the ceramic package.

Additionally, a Labview data acquisition program was designed and written to control the voltage sources for this thesis facilitating the electric field measurements. The voltage sources used in the present experiments is shown in the right panel of Figure 4.4.

4.2.1 Sample schematic

Two types of gated, individual dots were studied in this thesis: (1) dots in ridges and (2) dots in pyramids. The design of a gated ridge and pyramid comprising of an individual InAs/InP quantum dot (QD) is shown in Figure 4.5. In the case of a gated ridge (Figure 4.5(a)), pairs of metallic Schottky gates deposited across the InP nanotemplate with narrow (300 nm) gaps allow an in-plane electric field to be applied along the stripe direction of the ridge and serve to isolate the luminescence from individual quantum dots if the dot density is made sufficiently low (see Chapter 3). Figure 4.5(c) shows a sample schematic of a gated ridge with an applied bias, V,

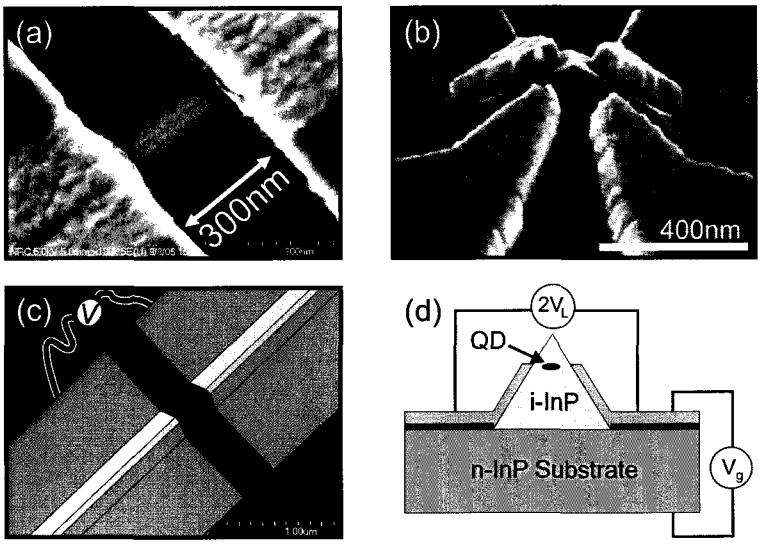

Figure 4.5: (a) SEM image of gated ridge comprising of buried individual quantum dots. (b) SEM image of gated pyramid containing buried individual InAs/InP quantum dot. (c) Schematic view of applied lateral electric field for gated ridges. (d) Schematic view of gated pyramid enabling application of electric field in any crystal orientation. A thin layer of SiO_2 is present to prevent electrical shorts between the four top Schottky contacts and n-doped InP substrate.

across the two Schottky contacts enabling the application of a lateral electric field.

In the case of a gated pyramid (Figure 4.5(b)), four top Schottky gates are precisely positioned around the periphery of a single quantum dot. This geometry allows an in-plane electric field to be applied across the quantum dot, or in conjunction with an ohmic back gate, an applied electric field along the growth direction for single electron charging experiments (Chapter 8). A schematic view of the gated pyramid is shown in Figure 4.5(d) depicting the position of the single quantum dot with respect to the surrounding gates. Note that the exact position of the quantum dot with respect to the electrodes in the case of gated ridges is not known.

4.2.2 Current-voltage characteristics

To ensure application of electric fields, devices were selected with very low leakage currents for the voltage ranges utilized in the experiments. Typical current-voltage (IV) characteristics are shown for gated ridges (lateral field) in Figure 4.6(a) and gated pyramids (vertical field) in Figure 4.6(c). Magnification of the dark current is shown in Figure 4.6(b) for the gated ridge, exhibiting very low leakage currents $\sim 10\,\text{pA}$. If the gated ridge is illuminated, the IV characteristics are typical of two reverse biased Schottky barriers. The IV characteristics for the gated pyramids in Figure 4.6(c)

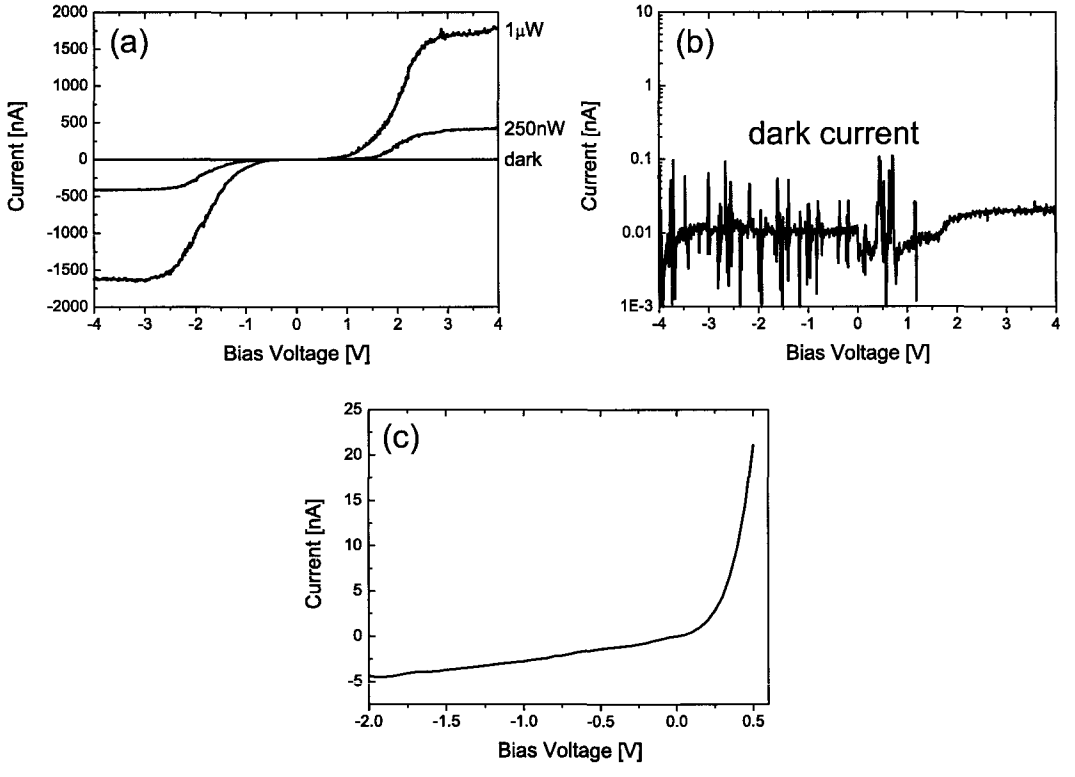

Figure 4.6: Typical IV characteristics for (a) gated ridges - lateral field and (c) gated pyramids - vertical field. (b) Magnification of the dark current for the gated ridge, exhibiting very low leakage currents $\sim 10\,\text{pA}$. In experiment, the voltages applied are limited to the low current regime to ensure application of an electric field.

are typical of n-i Schottky diodes used for single electron charging experiments in Chapter 8.

Electric field screening is evident in these experiments for higher excitation powers (Figure 4.6(a)). Here, a higher excitation power leads to a larger leakage current which screens the applied electric field. Thus, for the electric field measurements presented in thesis, the incident pump intensity was chosen to excite only the ground state transition from the single quantum dot at zero applied electric field such that only a single excitonic emission was observed and leakage current was minimized. More specifically, the single quantum dot emission was maximized, while observing only a single emission peak. This ensured that electric field screening was minimized for the present samples investigated.

Chapter 5

Theoretical model of single quantum dot in a lateral electric field

A theoretical model describing the effects of a lateral electric field on the optical properties of a single quantum dot is presented. The model accounts for new effects observed in a lateral electric field for the site-selected dots studied in this thesis. These same effects were not observed in previous work on randomly nucleated quantum dots [42, 47–49]. The objective of previous work was to facilitate the generation of entangled photon pairs [42, 47–49], by removing the fine-structure splitting using an in-plane electric field. This fine-structure splitting, also known as the anisotropic exchange splitting (AES), arises in anisotropic dots and is manifested as a removal of the degeneracy of the two optically bright exciton states in the quantum dot *s*-shell [64]. The intermediate exciton states in the biexciton-exciton cascade therefore emit at slightly different energies allowing one to distinguish the decay pathway and consequently destroying the photon entanglement (see Section 7.1 for definition of biexciton-exciton radiative cascade).

The theoretical model presented here describes the expected reduction of the AES

under applied lateral field, as observed in previous work and also in this thesis (discussed in detail in Chapter 6 and 7). Unfortunately, the oscillator strengths of many of the optical transitions are significantly reduced at the electric fields required to remove the AES. For scalability, an alternative scheme for the generation of entangled photon pairs is needed that utilizes a method that does not necessitate the removal of the fine-structure splitting. I show here that removal of the fine-structure splitting is no longer required if the biexciton binding energy can be tuned to zero. This unbinding of the biexciton is shown to occur for a single quantum dot subject to a lateral electric field.

In this chapter, full configuration interaction calculations are presented in the effective mass approximation that reveal how the biexciton is unbound through the manipulation of the electron-hole Coulomb interaction. This manipulation of the electron-hole Coulomb interaction also manifests itself as a compensation of the single exciton Stark shift. The compensation of the single exciton Stark shift does not occur if the field is applied along the growth direction. In addition to manipulation of Coulomb interactions, the electric field breaks the rotational symmetry of the dot and modifies electron-hole wavefunction overlaps of the optical transitions. This modification of electron-hole overlaps accounts for the appearance of a new, field-activated optical transition observed in experiment that is identified as a radiative recombination of the neutral exciton in an excited state involving an s-shell electron and p-shell hole ($s-p$). The ability to electrically switch between the ground state and forbidden, $s-p$ transition is expected to support applications in advanced single photon sources or electron-spin resonance techniques [26].

The calculations discussed in this chapter were performed by M. Korkusiński from

the Quantum Theory Group at the Institute for Microstructural Sciences, National Research Council. The calculations are compared with results from gated InAs/InP dots under applied lateral electric field in Chapter 6 and are found to be in excellent qualitative agreement. The single quantum dot is modeled as a two-dimensional parabolic potential using the effective mass approximation to obtain single particle states in the harmonic oscillator basis. Coulomb interactions and correlation effects are included that perturb the single particle energies, which are then calculated using the full configuration interaction method. In order to directly compare with experiment, emission spectra are calculated from the resulting energies and states using Fermi's golden rule.

The chapter is organized as follows: In Section 5.1, the theoretical model is described. The model presented here is distinguished from that developed by Ritter *et al.* [98], which only considered single excitons in the ground state. Section 5.2 describes the principle effects of a lateral electric field applied to a single quantum dot. In Section 5.3, calculated emission spectra from the neutral exciton are presented. Compensation of the single exciton Stark shift is briefly discussed in Section 5.3.2 and the much larger Stark shift of the field-activated optical transition is presented in 5.3.3. In Section 5.4, the removal of the biexciton binding energy in a lateral field is discussed. Finally, in Section 5.5, the calculated emission spectra from singly charged excitons are compared to that from the neutral exciton in order to exclude the presence of charged exciton species in the measured optical data presented in Chapter 6.

5.1 Theoretical model

5.1.1 Single particle states

In a single quantum dot where the vertical confinement is much stronger than the lateral confinement, the in-plane potential can be approximated by an isotropic two-dimensional (2D) harmonic oscillator potential in the effective mass approximation (see Chapter 2). In this theoretical model, the two-dimensional potential acts in the x-y plane and the electric field, $\vec{F} = F\hat{x}$, is directed along the x axis [27]. The profile of the confinement along the electric field direction is shown schematically in Figure 5.1(a) with the upper and lower parabola representing the electron and hole potentials, respectively [27]. The single particle Hamiltonian of an electron with effective mass, m_e^*, and charge $(-e)$ in such a displaced harmonic oscillator potential takes the form

$$\hat{H}_e = \frac{\hat{p}^2}{2m_e^*} + \frac{1}{2}m_e^*\omega_e^2\left(x^2 + y^2\right) - eFx, \tag{5.1}$$

where $\hbar\omega_e$ is the shell energy level spacing for electrons (characteristic harmonic oscillator energy) [27]. The first term of Equation 5.1 is the kinetic energy and second term is the 2D parabolic potential. Since the Hamiltonian is separable in the $x-$ and $y-$dependent parts, the effect on the single particle states for an electric field applied along the x axis can easily be determined. First, rearranging Equation 5.1 in the $x-$ and $y-$dependent parts gives

$$\hat{H}_e = \frac{\hat{p}^2}{2m_e^*} + \frac{1}{2}m_e^*\omega_e^2\left[\left(x^2 - \frac{2eF}{m_e^*\omega_e^2}x\right) + y^2\right]. \tag{5.2}$$

Completing squares gives

$$\hat{H}_e = \frac{\hat{p}^2}{2m_e^*} + \frac{1}{2}m_e^*\omega_e^2\left[\left(x^2 - \frac{2eF}{m_e^*\omega_e^2}x + \frac{(eF)^2}{(m_e^*\omega_e^2)^2} - \frac{(eF)^2}{(m_e^*\omega_e^2)^2}\right) + y^2\right]. \tag{5.3}$$

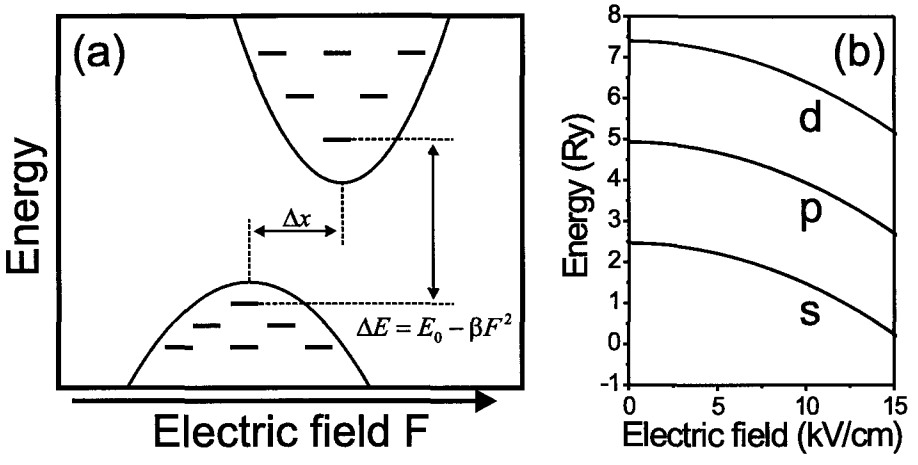

Figure 5.1: Fundamental properties of single quantum dot in a lateral electric field [27]. (a) Schematic picture of the system. (b) Energies of the single-particle states of an electron as a function of the field.

Simplifying Equation 5.3 provides the effect of the electric field along the x-axis on the single particle states

$$\hat{H}_e = \frac{\hat{p}^2}{2m_e^*} + \frac{1}{2}m_e^*\omega_e^2\left[\left(x - \frac{eF}{m_e^*\omega_e^2}\right)^2 + y^2\right] - \frac{(eF)^2}{2m_e^*\omega_e^2}. \tag{5.4}$$

The electric field shifts the origin of the potential for electrons by

$$\Delta x_e = +\frac{eF}{m_e^*\omega_e^2}. \tag{5.5}$$

The last term of Equation 5.4 produces a Stark shift, β_e, and reduces the single particle energies for electrons by

$$\beta_e = \frac{(eF)^2}{2m_e^*\omega_e^2}. \tag{5.6}$$

Similarly for holes, but with effective mass m_h^*, and opposite charge to that of the electron $(+e)$, the single particle Hamiltonian for holes takes the form

$$\hat{H}_h = \frac{\hat{p}^2}{2m_h^*} + \frac{1}{2}m_h^*\omega_h^2\left(x^2 + y^2\right) + eFx. \tag{5.7}$$

Applying similar algebra to the single particle Hamiltonian for holes as for electrons, the resulting Hamiltonian gives

$$\hat{H}_h = \frac{\hat{p}^2}{2m_h^*} + \frac{1}{2}m_h^*\omega_h^2\left[\left(x + \frac{eF}{m_h^*\omega_h^2}\right)^2 + y^2\right] - \frac{(eF)^2}{2m_h^*\omega_h^2}. \tag{5.8}$$

Comparing Equation 5.8 to 5.4, the opposite charge of the hole has the effect of shifting the origin of the hole confinement potential in the opposite direction to that of the electron:

$$\Delta x_h = -\frac{eF}{m_h^*\omega_h^2}. \tag{5.9}$$

The separation of the electron and hole confinement potentials is therefore $\Delta x = \Delta x_e - \Delta x_h$, which leads to separation of carriers and modification of the electron and hole wavefunction overlap. Comparing the last term in Equation 5.8 to that in 5.4, we have the same sign, leading to a Stark shift that lowers the emission energy. The Stark shift for holes is

$$\beta_h = \frac{(eF)^2}{2m_h^*\omega_h^2}, \tag{5.10}$$

the difference from β_e being the effective mass and harmonic oscillator energy.

The solutions of the single particle Hamiltonian for the electron in Equation 5.4 are displaced harmonic oscillator states with eigenstates $|n_e, m_e, \sigma_e\rangle$, and corresponding single particle energies

$$E^e(n_e, m_e) = \hbar\omega_e(n_e + m_e + 1) - \beta_e. \tag{5.11}$$

Here, $n_e, m_e = 0, 1, \ldots$ are the harmonic oscillator quantum numbers, and $\sigma_e = \pm 1/2$ (or $\uparrow, \downarrow$) is the electron spin. Due to the separability of the Hamiltonian in Equation 5.4, the wave functions are simple products of one-dimensional harmonic oscillator states, $\langle r|n_e, m_e\rangle = \phi_{n_e}(x - x_0^e)\phi_{m_e}(y)$ [27]. The single-particle eigenenergies,

$E^e(n_e, m_e)$, are represented by bars within the upper parabola in Figure 5.1(a). Similarly for holes, the solutions of the single particle Hamiltonian in Equation 5.8 are displaced harmonic oscillator eigenstates $|n_h, m_h, \sigma_h\rangle$, labeled by the heavy-hole spin $\sigma_h = \pm 3/2$ (or $\Uparrow, \Downarrow$), and corresponding single-particle energies

$$E^h(n_h, m_h) = \hbar\omega_h(n_h + m_h + 1) - \beta_h. \tag{5.12}$$

The single particle energies for holes are represented by bars within the lower parabola in Figure 5.1(a). Note that in assuming a 2D parabolic potential, the single particle spectra shell spacing (s, p, d) does not change as a function of the field. As a consequence, the shell structure does not change by the symmetry breaking introduced by the field, a rather counterintuitive result [27]. The electric field dependence of the single particle energies for electrons is plotted in Figure 5.1(b). The dependence of the single particle energies for holes is qualitatively similar to that of electrons, but with smaller energy level spacing between shells.

In the treatment for holes, the valence subband mixing effect is neglected, and only heavy holes are assumed as described in Chapter 2. To account for strain in the effective mass approximation, the values for $\hbar\omega_e$, and $\hbar\omega_h$ are selected appropriately. The value of the effective mass accounts for the effects of strain and the presence of the heterointerface (*i.e.*, the quantum dot is surrounded by a higher bandgap material). This value can either be computed by comparing the effective mass model to that of a more advanced calculation such as an atomistic model or by comparing with experiment, which accounts for strain automatically. In these model calculations, the confinement energy (energy level spacing) for electron and holes and ratio were selected for their similarity to the experimentally investigated dots in this thesis but were modified slightly to simplify the Coulomb matrix element calculations (*i.e.*, $m_e^*\omega_e = m_h^*\omega_h$).

The electronic effective mass was calculated by comparing the calculated electronic spectra for InAs quantum dots embedded in GaAs to that of a more advanced calculation that used the strain-dependent eight-band $k \cdot p$ Hamiltonian [99, 100]. The electronic effective mass was used as a fitting parameter, and was found to be between that of InAs and GaAs, as expected [100]. Although the surrounding material (InP) for InAs quantum dots studied in this thesis is different than GaAs, this system is also strained. Therefore, to qualitatively describe the effects of the applied lateral field in this thesis, a similar effective mass was selected as the InAs/GaAs quantum dot material system. It should be noted that this value of the electronic effective mass is also between InAs ($m_e^* = 0.023m_0$) and InP ($m_e^* = 0.08m_0$).

In the calculations presented here, the following system parameters are assumed: $\hbar\omega_e = 12$ meV; $m_e^* = 0.055m_0$; $\hbar\omega_h = 6$ meV and; $m_h^* = 0.11m_0$ with m_0 being the mass of a free electron [26].

5.1.2 Many-body Hamiltonian

In the previous section, the single particle energies for electrons and holes were determined in the presence of the quantum dot confining potential and applied in-plane electric field. In reality, electrons and holes are strongly interacting, charged particles and the single particle energies are renormalised by these interactions. In addition, an electron or hole can scatter to a higher lying exciton configuration and this further perturbs the exciton energy.

The strongly interacting electrons and holes confined within the quantum dot are

accounted for in the many-body Hamiltonian

$$\begin{aligned} H &= \sum_i \varepsilon_i c_i^\dagger c_i + \sum_j \varepsilon_j h_j^\dagger h_j + \frac{1}{2}\sum_{ijkl}\langle ij|V_{ee}|kl\rangle c_i^\dagger c_j^\dagger c_k c_l \\ &+ \frac{1}{2}\sum_{ijkl}\langle ij|V_{hh}|kl\rangle h_i^\dagger h_j^\dagger h_k h_l - \sum_{ijkl}\langle ij|V_{eh}|kl\rangle c_i^\dagger h_j^\dagger h_k c_l, \end{aligned} \tag{5.13}$$

where the composite indices $i = nm\sigma$ (likewise j, k, l) enumerate the electron and hole orbitals; σ denotes the carrier spin ($\pm 1/2$ for electrons, $\pm 3/2$ for holes) and; c_i,$c_i^\dagger$ (h_i,$h_i^\dagger$) denote the annihilation and creation operators for electrons (holes). In this Hamiltonian, the first two terms account for the single-particle properties and the following three terms describe the electron-electron, hole-hole, and direct electron-hole Coulomb interactions, respectively. The matrix elements scaling these interactions are obtained by direct integration in the harmonic-oscillator basis, which can be determined analytically [27].

Eigenenergies and eigenstates of the Hamiltonian (5.13) are calculated within a configuration interaction approach. This involves creating all possible configurations of N_e electrons and N_h holes on the three lowest single-particle shells (s, p, d), forming the Hamiltonian matrix in the basis of these configurations for each value of the electric field and diagonalizing it numerically [27]. In the shell model of quantum dots, there are six single particle states for electrons and six for holes (see Figure 5.1). In this finite basis of the parabolic quantum dot, there are a total of 36 possible configurations (6×6) that can be created for an exciton and approximately 1000 possible configurations for the biexciton (two excitons). In the configuration interaction approach, all possible configurations mix via the Coulomb interaction which therefore perturbs the single particle energy by a correlation correction term.

To compare directly with photoluminescence experiments, the emission spectrum,

$I(\omega)$, is calculated using Fermi's golden rule:

$$I(\omega) = \sum_f |\langle f, N_e - 1, N_h - 1|P^-|i, N_e, N_h\rangle|^2 \delta(E_i - E_f - \hbar\omega). \tag{5.14}$$

The radiative recombination takes place from the initial state $|N_e, N_h, i\rangle$ of N_e electrons and N_h holes. The summation extends over all final states $|N_e - 1, N_h - 1, f\rangle$ of $N_e - 1$ electrons and $N_h - 1$ holes. The energy of the emitted photon equals the energy difference between the initial and final states. The amplitude of the outgoing radiation is determined from the dipole matrix element involving the interband polarization operator $\hat{P}^-$. The $\hat{P}^-$ operator removes a single electron-hole pair from the system, where $\hat{P}^- = \sum_{ij} \alpha_{ij} c_i h_j$, and $\alpha_{ij} = {}_e\langle i|j\rangle_h$ is the overlap integral controlling the optical selection rules for the emission (*i.e.*, overlap between harmonic oscillator states). The effects of the electric field are captured both in the PL peak position corresponding to the difference between the energies of the initial and final states, and the PL peak amplitudes, governed by the overlaps between the single-particle states.

5.2 Effect of lateral electric field

In the simple model utilizing a 2D parabolic potential in the x,y direction and step-like potential along the growth direction (z), as described previously, the effect of the increasing applied lateral electric field is twofold. First, it separates the electron and hole parabolic potentials leading to a modification between electron-hole (e-h) wavefunction overlaps. Generally, e-h wavefunction overlaps exist between states belonging to the same shells at zero electric field, while overlaps between states originating from different shells appear at finite field. Secondly, the single particle energies are tending

towards lower energy due to the quantum confined stark effect leaving the energy level spacing for electrons and holes unaffected (see Figure 5.1).

5.2.1 Single particle electron-hole wavefunction overlap

The separation of electron and hole parabolic potentials leads to a modification of the optical selection rules in the quantum dot. At zero electric field, angular momentum is conserved so that allowed optical transitions correspond to states belonging to the same shells. For example, $|00\rangle_e \rightarrow |00\rangle_h$ $(s-s)$, $|10\rangle_e \rightarrow |10\rangle_h$ (p_x-p_x), $|01\rangle_e \rightarrow |01\rangle_h$ (p_y-p_y), *etc.* A lateral electric field applied along the x-direction has the effect of removing rotational symmetry of the confining potential so that angular momentum is no longer conserved in the band to band recombination process. Therefore, as the electron and hole are spatially separated with increasing field, the electron-hole overlap of the $s-s$ transition gradually decreases, while transitions between states that are forbidden at zero electric field become allowed due to the symmetry breaking of the field. The single-particle calculation of the e-h wavefunction overlaps for the s orbital electron, $|00\rangle_e$, with the s ($|00\rangle_h$), p_x ($|10\rangle_h$), and d_{xx} ($|20\rangle_h$) orbital holes are summarized in Figure 5.2. Since the electric field is applied along the x-direction, the e-h overlaps of the s electrons with the p_y ($|01\rangle_h$), d_{xy} ($|11\rangle$), and d_{yy} ($|02\rangle$) orbital holes are expected to be zero due to the orthogonality of the wave-functions along x- and y- directions. In contrast, the $s-s$ transition e-h overlap gradually reduces to zero, whilst the $s-p_x$, and $s-d_{xx}$ transition e-h overlaps slowly rise to a maximum and then quench with increasing electric field. Note that these calculations only account for the single particle e-h wavefunction overlaps and do not consider the time-dependent dynamics to populate the states experimentally (see Chapter 6). As an example, a previous recombination event may leave the system in an excited state

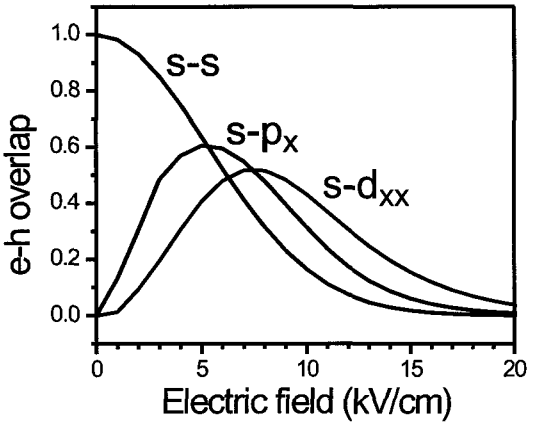

Figure 5.2: Calculated single particle electron-hole wavefunction overlaps of s electron orbital with s hole $(s-s)$, p hole $(s-p_x)$, and d hole $(s-d_{xx})$ as a function of lateral electric field depicted in red, blue, and black, respectively.

which can then be observed experimentally.

5.3 Neutral exciton in a lateral electric field

5.3.1 Calculated photoluminescence spectra

The strength of the PL transitions (PL amplitudes) and the PL peak positions as a function of lateral electric field for the neutral exciton are calculated to compare theory with experiment. The PL amplitudes are extracted utilizing Fermi's golden rule (see Equation 5.14) and the peak positions are calculated in the configuration interaction approach (see Section 5.1). The neutral exciton in the ground state involves recombination of an s-shell electron and s-shell hole $(s-s)$ and the first excited state that appears at finite bias in experiment is formed by placing an electron on the s-shell orbital and the hole on one of the p-shell orbitals $(s-p)$. These results include the calculated single particle overlaps presented in Figure 5.2 as well as Coulomb interaction and correlation effects. In the following calculaton, the initial state is

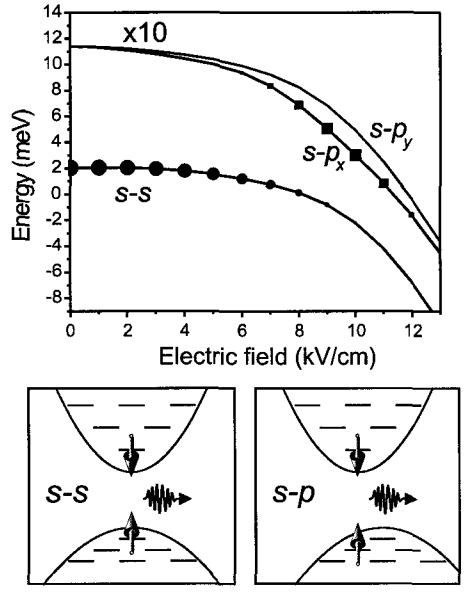

Figure 5.3: (Upper panel) Calculated emission spectra from the excitonic ground state ($s-s$, red circles) and first excited states ($s-p_x$, blue squares and $s-p_y$, black line) as a function of the electric field. The size of the symbols represent the PL amplitudes. The PL amplitudes of $s-p_x$ and $s-p_y$ optical transitions are multiplied by a factor of 10. Note that the PL amplitude of $s-p_y$ remains zero for an applied electric field along the x-axis. (Lower panel) Dominant configuration which contributes to the many-body wavefunction for the calculated emission spectra in the upper panel.

assumed to be populated by only a single exciton, which has the possibility to scatter to higher lying states via the Coulomb interaction and perturb the exciton energy. The main contribution of the wavefunction is determined by diagonalizing the Hamiltonian in the configuration interaction method. The dominant component in the full exciton wavefunction for the $s-s$ optical transition is with both the electron and hole occupying the s-shell orbital, while the main contribution to the wavefunction for the s-p_x transition involves an s-shell electron, and p-shell hole.

The results of the calculation for the $s-s$ (red circles) and $s-p_x$ (blue squares) optical transitions as a function of applied lateral electric field along the x-direction are shown in the upper panel of Figure 5.3. Note that the PL amplitude of $s-p_y$

(black line) remains zero for an applied electric field along the x-axis. The dominant contribution to the many-body wavefunction for the $s-s$ and $s-p_x$ transition is shown schematically in the lower panel of Figure 5.3. As discussed previously for the calculated overlaps, the strength of the transition shifts from the $s-s$ to the $s-p_x$ transition; however, in the case of the configuration interaction calculations, the amplitude of the $s-s$ transition decreases more gradually at fields of less than 9 kV/cm and rapidly for fields in excess of 9 kV/cm. Moreover, the electric field range in which the $s-p_x$ retains PL amplitude is decreased. The overlap between the s-shell states using the shell model notation is [27]

$$ {}_e\langle 00|00\rangle_h = \exp[-(\Delta x)^2/8\ell_e^2], \tag{5.15}$$

while the overlap between the s-shell electron and p-shell hole states is

$$ {}_e\langle 00|01\rangle_h = 0 \tag{5.16}$$

for $s-p_y$ and

$$ {}_e\langle 00|10\rangle_h = \frac{1}{2\ell_e}\Delta x \exp[-(\Delta x)^2/8\ell_e^2] \tag{5.17}$$

for $s-p_x$. Here, l_e is the electronic oscillator length. The dependence on the electric field enters via $\Delta x = x_0^e - x_0^h$, so that as the electric field grows, the first of these elements (Equation 5.15), $s-s$ decreases monotonically, while the last one (Equation 5.17), $s-p_x$, increases and then quenches [27].

5.3.2 Exciton Stark shift

The lowest-energy configuration of the neutral exciton, X^0, involves a single electron-hole pair occupying the quantum dot s-shell as discussed in Chapter 2. This is the $s-s$ transition discussed in Section 5.3.1. There are four possible configurations for

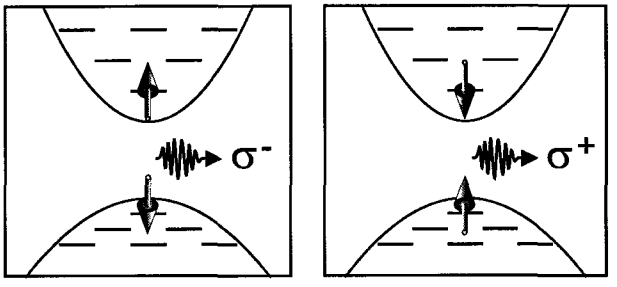

Figure 5.4: Possible spin configurations for bright exciton states. By conservation of angular momentum, a left or right circular polarization photon is emitted depending on the spin configuration of the exciton. See Chapter 2.3 for more details.

X^0 including spin with two possible bright excitonic states. The two possible bright excitonic states are shown in Figure 5.4. The optically active state is

$$|X^0, \sigma^+\rangle = c^+_{00\downarrow} h^+_{00\Uparrow} |0\rangle \tag{5.18}$$

and the remaining state is

$$|X^0, \sigma^-\rangle = c^+_{00\uparrow} h^+_{00\Downarrow} |0\rangle. \tag{5.19}$$

In the absence of the electron-hole exchange, these configurations have the same energy,

$$E_{X^0} = E^e(0,0) + E^h(0,0) - V_0^{eh} - \Delta E_x^{corr}, \tag{5.20}$$

which is a sum of the energies of the s-shell electron and hole and their Coulomb attraction. The last term, ΔE_x^{corr}, is the correlation correction term arising as a result of mixing the configuration $|X^0\rangle$ with higher lying exciton configurations. Since the final state of the neutral exciton is the vacuum, the calculated exciton energy can be determined directly from optical experiments.

As determined in Equation 5.6 and 5.10, the single-particle energies of the electron and hole, $E^e(0,0)$ and $E^h(0,0)$, exhibit a Stark red shift quadratic in F. The sum of these two energies as a function of the field, F, is plotted in Figure 5.5(a) with

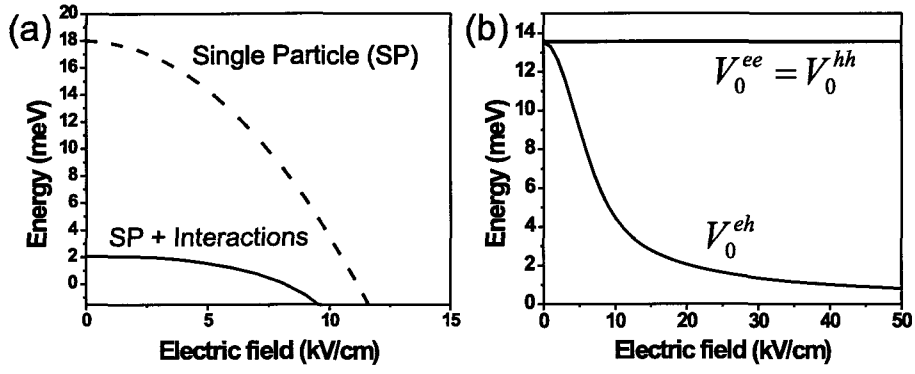

Figure 5.5: (a) Calculated exciton Stark shift without (blue dotted line) and with Coulomb electron-hole interactions (black solid line) [26]. (b) Fundamental Coulomb matrix element V_0^{ee}, V_0^{hh}, and V_0^{eh} calculated as a function of the electric field [26].

the dotted blue line. The quadratic dependence on the electric field to lower energies is normally what one would expect for single quantum dots studied in vertical electric fields [3, 101]. Considering vertical and lateral confinement energies typical of self-assembled quantum dots, the single particle Stark shift is expected to be significantly larger in a lateral electric field compared to that of a vertical electric field. This is due to a much weaker lateral confinement compared to that for vertical confinement. This confinement energy, w, appears in the denominator as a quadratic term when calculating the single particle Stark shift. Therefore, smaller w results in a larger Stark shift, β. For example, the ratio of vertical to lateral confinement for the InAs/InP quantum dots studied in this thesis is approximately 10:1. Estimating the single particle Stark shift in vertical and lateral electric fields for confinement energies typical of InAs/InP quantum dots, the Stark shift in a vertical electric field ($\beta = 2.1\ \mu\text{eV}\,\text{cm}^2/\text{kV}^2$) is two orders of magnitude smaller than what is expected in a lateral electric field ($\beta = 144\ \mu\text{eV}\,\text{cm}^2/\text{kV}^2$).

In reality, the Stark shift in a lateral electric field differs from that expected within

a single particle picture as a result of the Coulomb interaction between electron and hole. The calculated exciton energy including electron-hole Coulomb interaction is shown in Figure 5.5(a) with the solid black line. Here, the exciton energy is reduced by the exciton binding energy and the Stark shift is strongly compensated compared to the single particle picture. To understand this reduction of the Stark shift in a lateral electric field, the Coulomb matrix elements are calculated in the harmonic oscillator basis. The fundamental electron-hole Coulomb matrix element at zero electric field is [27]

$$V_0^{eh} = \langle 00, 00 | V_{eh} | 00, 00 \rangle = \sqrt{\pi \Omega_e}, \tag{5.21}$$

where $\Omega_e = 2.466 Rydberg$ (*i.e.*, $\hbar\omega_e = 12\,\mathrm{meV}$).

In Figure 5.5(b), the fundamental matrix element V_0^{eh} as a function of the field is plotted together with the fundamental electron-electron (V_0^{ee}) and hole-hole (V_0^{hh}) elements. The electron-electron and hole-hole elements are independent of the field, since the symmetry or spatial extent of the harmonic orbitals do not change and the relative distances between carriers of the same type remain constant. In contrast, the electron-hole element V_0^{eh} decreases exponentially with the increase of the field due to the spatial separation of the charges. Since this element enters the exciton energy with a negative sign, it partially compensates the single-particle red shift. The calculated polarizability β of this exciton is 30 $\mu\mathrm{eV\,cm^2/kV^2}$; however, this result is sensitive to the confinement energies of the system. Small changes in the lateral confinement potential of less than 10 % reduces β further by a factor of five ($\hbar\omega_e = 14\,\mathrm{meV}$, $\hbar\omega_h = 4\,\mathrm{meV}$). Such changes in the Stark shift are a direct result of the interplay between single-particle effects and Coulomb interactions. It should be noted that a quadratic fit was used to obtain the Stark shift quoted here. The quadratic fit

was made over the electric field range in which the exciton state retains its oscillator strength (see Section 5.3.1). The exponential decrease of the electron-hole Coulomb interaction modifies the quadratic dependence of the single particle Stark shift. Only when V_0^{eh} approaches zero does the Stark shift revert back to its quadratic form. At the electric field where V_0^{eh} approaches zero, the PL amplitude of the ground state exciton is negligible. The calculated β is still larger than that obtained experimentally ($\beta = 0.31\ \mu\text{eV cm}^2/\text{kV}^2$) in the next chapter, but this fundamental result qualitatively explains the strong reduction of the Stark shift as compared to the single particle picture.

The above argument does not apply in vertical electric fields. Due to the small QD height (several nm) the electrons and holes cannot be efficiently separated, which results in a much weaker dependence of V_0^{eh} on the field. As a result, the Stark shift is dominated by the single-particle effect, and the measured Stark shifts are expected to be similar to that of the single particle calculation.

5.3.3 Stark shift of forbidden $s-p$ transition

The first excited state of the neutral exciton involving an s-shell electron and p-shell hole is well approximated by the configuration,

$$|X^{s-p}\rangle = c^{+}_{00\downarrow} h^{+}_{10\Uparrow} |0\rangle. \tag{5.22}$$

This configuration is absent at zero electric field, but becomes allowed at finite field. The results of the emission spectra in a lateral electric field reveal that the Stark shift of $|X^{s-p}\rangle$ is larger than the $|X^0\rangle$ exciton (see Figure 5.3). By applying a quadratic fit to $|X^{s-p}\rangle$ over the electric field range in which the e-h overlap is retained, a Stark shift $\beta = 130\,\mu\text{eV cm}^2/\text{kV}^2$ is obtained. The value of β is very close to the single

particle Stark shift, which is a direct result of the e-h Coulomb interaction term that is significantly smaller at finite fields than at zero electric field. In addition, the Coulomb matrix element for $|X^{s-p}\rangle$ is slightly smaller than $|X^0\rangle$, thus providing less compensation to the single particle Stark shift.

The transition energy of the forbidden transition, $|X^{s-p}\rangle$, is given by

$$E_{s-p} = E_e^{(s)} + E_h^{(p)} - 0.75V_{eh}. \tag{5.23}$$

The term $E_e^{(s)}$ indicates the energy of an electron in the s-shell, whereas $E_h^{(p)}$ indicates the energy of a hole in the p-shell. Both of the single particle terms exhibit a quadratic Stark shift to lower energies similar to that of $|X^0\rangle$. In contrast, the factor scaling the matrix elements of the electron-hole Coulomb interaction, V_{eh}, does not compensate the Stark shift as strongly as for $|X^0\rangle$ implying a stronger Stark shift for $|X^{s-p}\rangle$, as observed experimentally in Chapter 6.

5.4 Biexciton in a lateral electric field

A biexciton, XX, is formed when an electron-hole pair is captured by the quantum dot in the presence of an additional exciton. The lowest energy configuration of XX, $|XX\rangle = c^+_{00\uparrow}c^+_{00\downarrow}h^+_{00\Uparrow}h^+_{00\Downarrow}|0\rangle$, is formed when all carriers are placed in the quantum dot s-shell. This configuration is shown schematically in Figure 5.6. The energy of this configuration,

$$E_{XX} = 2E^e(0,0) + 2E^h(0,0) + V_0^{ee} + V_0^{hh} - 4V_0^{eh} - \Delta E_{xx}^{corr}, \tag{5.24}$$

contains two single particle electrons and holes (1st two terms), electron-electron and hole-hole repulsion, and four times the electron-hole attraction. Here, the electron-hole Coulomb term arises since there are two electron-hole pairs building the biexciton, and interactions between the electron and hole of the same spin. The last term is the correlation energy of XX and is a small correction to the XX energy due to higher lying configurations. Substituting the X^0 energy from Equation 5.20 into the XX energy above, Equation 5.24 simplifies to

$$E_{XX} = 2E_X^0 + \left(V_0^{ee} + V_0^{hh} - 2V_0^{eh}\right) + \left(2E_x^{corr} - E_{xx}^{corr}\right). \tag{5.25}$$

Since the final state of the biexciton is the exciton, the energy of the emitted photon is the difference between the initial biexciton state and final exciton state:

$$E_{XX} - E_X^0 = E_X^0 + \left(V_0^{ee} + V_0^{hh} - 2V_0^{eh}\right) - \left(E_{xx}^{corr} - E_x^{corr}\right). \tag{5.26}$$

The absence of Coulomb interactions and correlation effects leads to the appearance of the XX and X^0 emission peaks at the same energy (zero XX binding energy). By including all interaction terms and at zero electric field (second term), the repulsion between carriers of the same type is balanced by electron-hole attraction and the binding energy of XX is zero. It is the third term, comparing the correlation corrections of the biexciton to those of the exciton, which determines whether the binding energy of XX is negative or positive. This correlation correction term is usually negative resulting in biexcitonic emission peaks that appear at lower energies than those of single excitons.

Figure 5.6 shows the calculated emission spectra of the biexciton and exciton as a function of lateral electric field for a bound biexciton (XX emission energy below X^0). With increasing electric field, the photon emitted by the exciton redshifts while

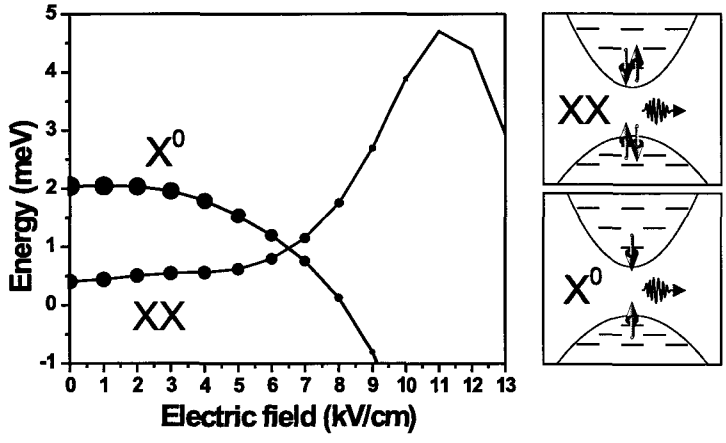

Figure 5.6: Calculated emission spectra of exciton, X^0, and biexciton, XX, as a function of lateral electric field. For a critical value of the electric field, $F = 6.5\,\mathrm{kV/cm}$, the emission energies of XX and X^0 cross and the binding energy of XX is removed. Of particular importance is that this crossing envisions the possibility for production of entangled photon pairs. The lowest energy for XX and X^0 is shown in the right panel. Note the other spin configuration for X^0 is also possible.

the photon emitted from the biexciton blueshifts. In these model calculations, at $6.5\,\mathrm{kV/cm}$, the Coulomb interaction terms cancel the correlation corrections, resulting in a degeneracy of the biexciton and exciton emission. This crossing of the exciton and biexciton emission lines allows pairs of entangled photon pairs to be produced when the biexciton binding energy has been removed [25, 27]. The possibility to generate entangled photons pairs by removing the biexciton binding energy in a lateral electric field is discussed in Chapter 7.

The blueshift of the biexciton photon is understood through manipulation of the Coulomb interaction terms in Equation 5.26. The Stark shift of the exciton (first term) is almost unchanged because of the competing single particle and electron-hole Coulomb interaction. However, as the electrons and holes are separated via the electric field, the electron-hole attraction decreases driving the biexciton PL peak positions towards higher energies. The biexciton blueshifts until the electron-hole

Coulomb attraction is turned off after which the biexciton quadratically redshifts.

5.5 Charged exciton complexes

To preclude the presence of charged exciton species appearing under applied bias in experiment (Chapter 6), it is necessary to compare calculated charge neutral emission spectra with that of charged emission spectra in a lateral electric field. Additional configuration interaction calculations have been performed corresponding to recombination events from both singlet and triplet singly charged excitons in a lateral electric field involving X^+ and X^-. Here, only a detailed discussion of the positively charged exciton is discussed since the behaviour of the emission spectra of X^- is qualitatively the same.

The results of the calculation for the positively charged exciton, X^+, is given in Figure 5.7(a). The calculated energies and Stark shift of X^+ is compared to that of the neutral exciton for the ground state ($s-s$) and the forbidden transition ($s-p$) presented in Section 5.7. The neutral exciton species are replotted in Figure 5.7(a) with open symbols for direct comparison. The positively charged exciton dominant configuration is shown in Figure 5.7(b)-(e). There are two possible spin configurations for X^+: holes forming a spin-triplet $|X_T^+\rangle$ or holes forming a spin-singlet $|X_S^+\rangle$. The $|X_T^+\rangle$ complex ground state is well approximated by the lowest-energy configuration

$$|X_T^+\rangle = c_{00\downarrow}^\dagger h_{00\uparrow}^\dagger h_{01\uparrow}^\dagger |0\rangle. \tag{5.27}$$

This configuration is shown schematically in Figure 5.7(b) and (c). Radiative recombination from this state can occur in two ways: (i) the s-shell electron recombines with the s-shell hole as shown in Figure 5.7(b) or; (ii) the s-shell electron recombines with the p-shell hole as shown in Figure 5.7(c). As a result, two emission lines are

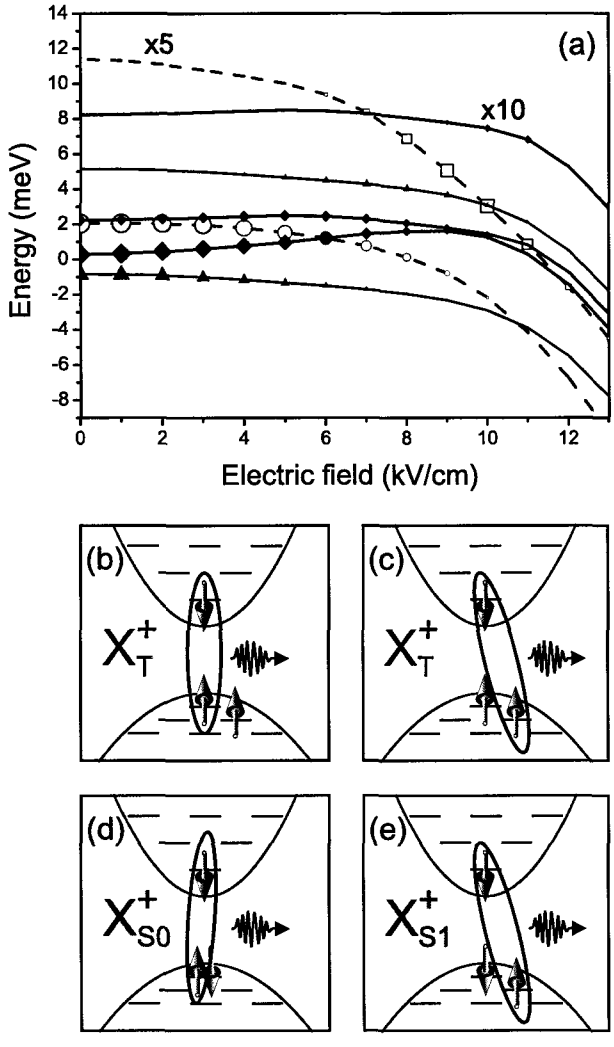

Figure 5.7: (a) Comparison of neutral exciton and positively charged exciton in a lateral electric field. Calculated emission spectra of the neutral exciton for the ground $s-s$ exciton state (open red circles) and excited $s-p$ state (open blue squares) compared to the positively charged exciton complex in the hole triplet (green triangles) and hole singlet (brown diamonds) configuration. The size of the symbols is proportional to the calculated emission amplitude. The PL amplitudes of the neutral $s-p$ transition is multiplied by a factor of 5 while the excited X_{S1}^{+} configuration in (e) is multiplied by 10. Panels (b) and (c) show the ground state configuration of the triplet charged exciton X_T. Panels (d) and (e) show the ground and first excited configuration of the singlet charged exciton, $X+S$, and $X+S_1$, respectively. The carriers undergoing radiative recombination are marked with an oval.

expected with case (ii) realized only at finite fields. In Figure 5.7(a), the calculated emission lines (green triangles) are found on either side of the $s-s$ emission line (open red circles). Note that the lower line arising from case (i) corresponds to energies lower than $s-s$, the extra binding energy is due to additional correlations brought about by the presence of the extra hole. The field dependence of $|X_T^+\rangle$ for both emission lines exhibits a slightly smaller Stark shift than $s-s$.

In the case of $|X_S^+\rangle$ two configurations are considered. In one of them both holes occupy the s-shell,

$$|X_{S0}^+\rangle = c_{00\downarrow}^\dagger h_{00\uparrow}^\dagger h_{00\downarrow}^\dagger |0\rangle, \tag{5.28}$$

as shown schematically in Figure 5.7(d). In this case, the radiative recombination involves only the carriers from the s-shell. In the second configuration the holes occupy the s- and p-shells,

$$|X_{S1}^+\rangle = (c_{00\downarrow}^\dagger h_{00\uparrow}^\dagger h_{01\downarrow}^\dagger |0\rangle + c_{00\downarrow}^\dagger h_{01\uparrow}^\dagger h_{00\downarrow}^\dagger |0\rangle)/\sqrt{2}, \tag{5.29}$$

as shown in Figure 5.7(e). Here the emission can occur as a result of recombination of the s-shell electron and either s-shell or p-shell hole. The three emission lines corresponding to the $|X_S^+\rangle$ complex are shown in Figure 5.7(a) with brown diamonds. The highest-energy $|X_S^+\rangle$ emission line appears to be a good candidate for the additional emission maximum seen in the experiment. However, its Stark shift is comparable to that of the neutral $s-s$ exciton in the $|X^0\rangle$ configuration (open red circles), whilst the Stark shift of the neutral, excited $s-p$ configuration (open blue squares) is much larger. The smaller Stark shift of the $|X_S^+\rangle$ line than $s-p$ is due to the fact that the suppression of the electron-hole interactions is larger as the electron interacts with two holes instead of only one. This same argument can be applied to all other charged complexes presented in Figure 5.7(a).

The magnitude of the Stark shifts is understood within the same formalism presented previously in Section 5.3 for the compensated Stark shift of $|X^0\rangle$ in the ground state $(s-s)$. The transition energy of X^+ is given by,

$$E_{X+} = E_{X^0} + V_{hh} - V_{eh}, \tag{5.30}$$

where E_{X^0} is the transition energy of the uncharged exciton; V_{hh} is the hole-hole Coulomb repulsion and V_{eh} is the electron-hole Coulomb attraction. In this expression, it is the hole-hole and electron-hole Coulomb interaction terms that differentiate the Stark shift of the charged exciton from that of the uncharged exciton. The h-h repulsion is independent of the lateral electric field since the shell separation does not change and the separation of holes remains constant for a 2D harmonic oscillator parabolic potential. In contrast, the strong modification of the e-h attraction due to the field-induced separation of electrons and holes provides the mechanism to further reduce the Stark shift of X^+. Similar arguments are also valid for X^-.

Comparable analysis has been performed for the negatively charged exciton X^- composed of a single hole and two electrons (not shown in Figure 5.7(a)). The position and behavior of the emission peaks resulting from the recombination of the s-shell hole and the s-shell electron are very similar to the respective X^+ peaks. In contrast, the recombination of the s-shell hole and the p-shell electron results in the emission of a higher-energy photon compared to that in the X^+ complex because of the larger electron confinement energy. The field dependence of the X^- peaks being qualitatively the same as that of the X^+ maxima and combined with the additional energy argument allows the presence of the negatively charged exciton to be excluded in the measured spectra in Chapter 6.

Chapter 6

Single quantum dot in a lateral electric field

Experimental optical emission data from excitonic complexes within a deterministically positioned InAs/InP single quantum dot subject to an in-plane electric field are investigated, where control over the dot nucleation site allows one to precisely position electrostatic gates with respect to the dot. Previous work in this area [42, 47–49, 102] has used randomly nucleated quantum dots. The experimental results presented here are compared to the theoretical calculations presented in the previous chapter and excellent qualitative agreement is found. As seen in previous work on randomly nucleated quantum dots [42, 47–49], a reduction in the fine-structure splitting is observed under applied lateral field. In addition, the excitonic Stark shift of the ground state is strongly compensated and a new optically allowed transition appears under applied bias for both directions of the field. Compared to model calculations, the additional maximum is identified as a recombination event of a neutral exciton in an excited state rather than a signature of charged excitons.

This chapter is organized as follows: Section 6.1 introduces the samples (InAs

dots on InP ridge templates) used in the present experiments and discusses the optimum experimental conditions utilized for the electric field measurements. In Section 6.2, experimental optical data are presented for a single prepositioned quantum dot as a function of applied lateral field (labeled QD1). The experimentally observed compensation of the Stark shift for the ground state is discussed in Section 6.2.1 and the observation of a new, field-activated optical transition is presented in Section 6.2.2. In Section 6.3, another dot subject to a lateral electric field is presented which exhibits a fine-structure splitting (labeled QD2). In Section 6.4, the electric field is calibrated by comparing experiment with theoretical calculations presented in the previous chapter. Finally, in Section 6.5, the main conclusions are summarized.

6.1 Sample

Figure 6.1 shows a schematic view of the sample used in the present experiments. InAs dots are nucleated at the apex of a "stripe geometry" InP nanotemplate and subsequently capped with InP. These templates, produced *in situ* during crystal growth, allow one to control the surface migration of deposited InAs, so that the nucleation site of the dots can be selected *a priori* [30]. Pairs of metallic Schottky gates, deposited across the InP nanotemplate, with narrow (300 nm) gaps, allow in-plane electric fields to be applied along the stripe (x-) direction and serve to isolate the luminescence from individual quantum dots if the dot density is made sufficiently low (see Chapter 3 for more details on single dot isolation). The inset of Figure 6.1 shows typical photoluminescence (PL) data at low excitation powers (~ 0.01 W/cm^2) from such a structure. The observed emission peak indicates that the single dot regime on the ridge nanotemplate has been reached.

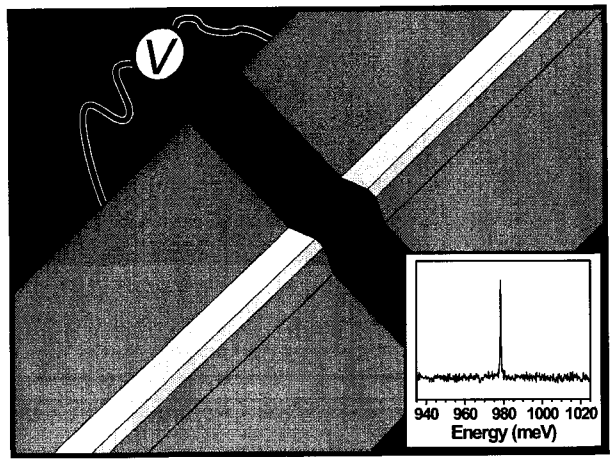

Figure 6.1: Schematic view of the device showing two metallic gates on top of an SEM micrograph of an uncapped, "stripe geometry" InP ridge. A linear array of InAs quantum dots is seen at the apex of the ridge in the gap (300nm) separating the gates. In real devices, the quantum dots are capped with InP prior to gate deposition and the dot density is chosen to be lower than that shown here, so that individual dots can be isolated. Shown in the inset is a typical PL spectrum at 4.2 K with a power of approximately 0.01 W/cm^2. The emission line at 978.5 meV is resolution limited ($\sim$ 0.25 meV) [26].

Single dot isolation is confirmed on the ridge nanotemplate by performing micro-PL state-shell filling spectroscopy from a single quantum dot obtained from a gap such as that shown in Figure 6.1 (data obtained at zero electric field). The optical data for this particular dot (labeled QD1) verify that this is indeed an isolated quantum dot where typical state-shell filling spectroscopy is observed [29, 80]. Such behaviour is typical of ridge templates and has been observed in more than 40 dots ranging with emission wavelength from 1260 nm to 1580 nm. Shown in Figure 6.2(a) are PL data from QD1 as a function of increasing pumping power. At the lowest excitation power in Figure 6.2(a) (also shown in the inset of Figure 6.1), a single, resolution limited line is observed at 978.5 meV. The power dependence of the observed emission peak at 978.5 meV identifies the optical transition as a radiative recombination of the neutral

exciton (X^0) ground state, involving a single electron-hole pair from the quantum-dot s-shell (see Figure 6.2). The narrow linewidth of X^0 indicates that the dot is of very high optical quality and that the template controlling the dot nucleation site does not degrade its optical emission. Such an observation is also confirmed by atomistic calculations of the electronic and optical properties of an InAs quantum dot on an InP patterned substrate [40].

Confirmation of the assignment for X^0 is determined by the linear dependence of the integrated intensity with increasing excitation power shown in Figure 6.2(b). This assignment is corroborated by the observation of an anisotropic exchange splitting in the ground state transitions from some dots as is discussed in Section 6.3. Increasing the excitation power modifies the average exciton occupancy of the dot and emission is observed from states involving the p-shell. The p-shell transitions for QD1 presented in Figure 6.2(a) begin around 990 meV. The satellite peaks a few meV around X^0 arise from recombination of s-shell exciton states perturbed by the presence of excitons occupying higher lying p-shell states [92].

The saturation of the integrated intensity for X^0 in Figure 6.2(b) is attributed to the statistical nature of capturing electrons and holes into the quantum dot using non-resonant optical excitation [92] (see Section 4.1.1). Neglecting the relative lifetimes of exciton states occupied, the excitation power at which saturation is achieved corresponds to an average of a single exciton occupancy [92]. Thus, for the electric field measurements presented in this chapter, the incident pump intensity was chosen to excite only the ground state transition from QD1 at zero applied electric field such that only a single excitonic emission is observed. More specifically, the single quantum dot emission was maximized while observing only a single emission

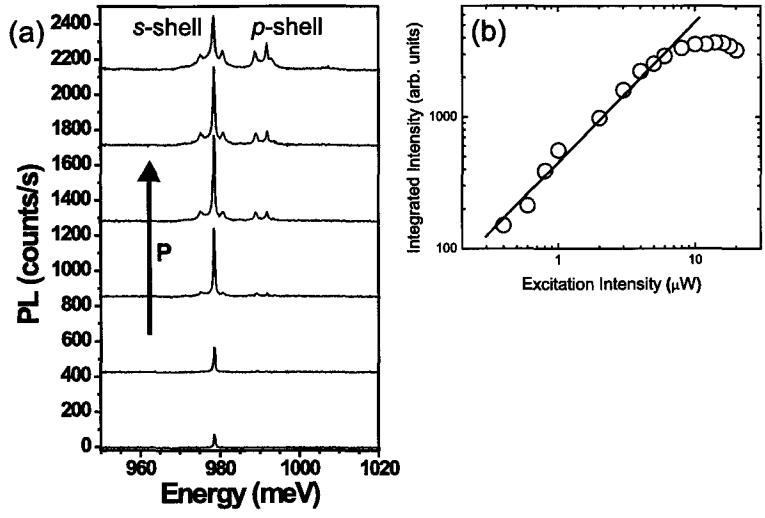

Figure 6.2: (a) Power dependence PL spectra at 4.2 K of a single QD isolated in the gap from a sample such as that shown in Figure 6.1. The spectra is offset along the y-axis for clarity. (b) Integrated intensity of X^0 exhibiting linear power dependence. Note that the linear dependence is on a log-log scale since the probability to have an average occupation of exactly one exciton is governed by a Poisson distribution.

peak. This ensured that electric field screening was minimized for the present samples investigated.

6.2 Application of a lateral electric field

Single-dot photoluminescence under applied lateral field is shown for QD1 in the main panel of Figure 6.3, which is typical for such a deterministically positioned quantum dot. At 0 V bias, only the single X^0 emission line at 978.5 meV is observed. The X^0 transition is seen to retain its oscillator strength under applied field until biases of approximately ± 2.0 V, at which point it quickly quenches. As the X^0 transition loses oscillator strength, a second transition appears at approximately 5 meV higher energy, which is itself quenched at higher bias. A schematic illustration for interpretation of the effects of the applied lateral electric field is shown in the inset of Figure 6.3.

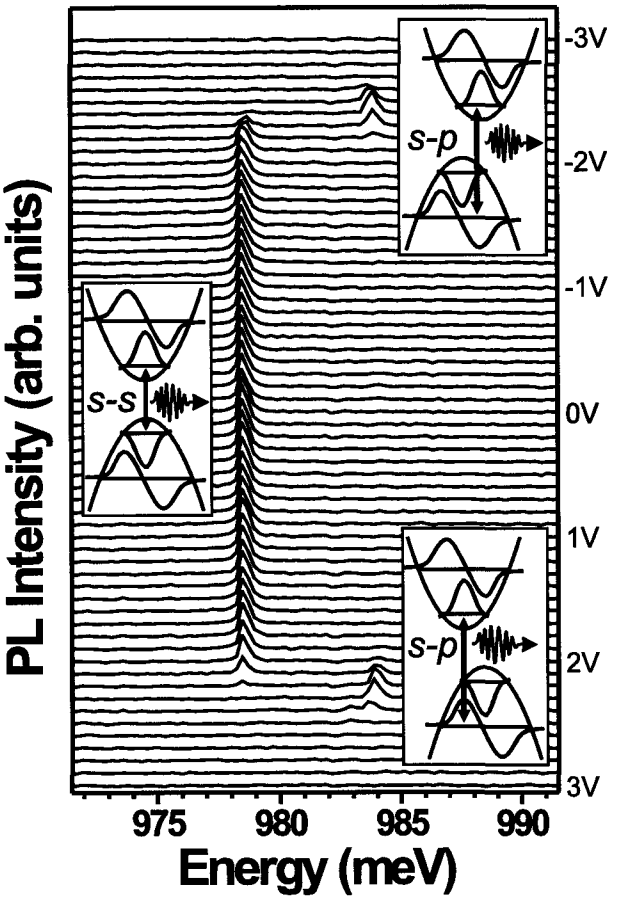

Figure 6.3: Typical photoluminescence spectra as a function of the lateral electric field at T = 4.2 K for both bias directions. A schematic view of the allowed transition $(s - s)$ at 0 V and forbidden transition $(s - p_x)$ at $\pm$ 2.2 V are shown in the inset. The electron wavefunctions are shown in blue and hole wavefunctions in red [26].

Here, the addition of a linearly varying potential has the effect of misaligning the centers of the electron and hole parabolic confining potentials and of reducing the energy gap, *i.e.*, producing a Stark shift. At 0 V bias, the wavefunction overlap for an s-shell electron and an s-shell hole is maximal as shown in the central inset of Figure 6.3. With increasing lateral field, this wavefunction overlap decreases as the electron and hole are separated, while the excited state overlap, corresponding to an s-shell electron and p-shell hole, increases (top and bottom insets of 6.3). This newly

allowed transition, an s-shell electron recombining with a p-shell hole, is associated with the transition observed at 984 meV in Figure 6.3. Since the measured Stark shift of the ground state X^0 in Figure 6.3 is surprisingly small and not immediately apparent within the spectral resolution, the additional maximum is used to confirm the application of a lateral electric field.

The behavior illustrated in Figure 6.3 is typical of single InAs quantum dots nucleated on ridge nanotemplates and has been observed on eight separate quantum dots nucleated on templates with a variety of widths. Over the eight dots measured, the average separation between the neutral exciton and the additional finite-bias emission peak is (4.8 ± 0.6) meV while the average separation of emission peaks originating from the s- and p-shells is (13 ± 3) meV. This result provides a direct probe of the energy level spacing for electrons ($\hbar w_e$) and holes ($\hbar w_h$) in the same PL experiment. Taking the mean energies obtained in experiment, the separation of the the $s - s$ and $s - p$ optical transition provides an estimation of the hole energy level spacing ($\hbar w_h = 4.8$ meV). Since the s- and p- shell separation is $\hbar w_e + \hbar w_h = 13$ meV, the electron energy level spacing is determined to be $\hbar w_e = 8.2$ meV. Thus, the ratio of the electron and hole confinement energies is $\hbar w_e : \hbar w_h = 1.7 \pm 0.3 : 1$. The ratio of electron and hole confinement energies measured here are very close to the assumption made in the effective mass approximation calculations presented in the previous chapter, where a ratio of confinement energies for electrons and holes of 2:1 was selected.

In addition to the small Stark shift and peak appearing under finite bias in Figure 6.3, the optical response is symmetric about 0 V bias. The insensitivity of the data to electric field direction is expected within the present interpretation. Such insensitivity

is unlikely if the peak appearing under applied bias is a result of additional charges being added to the system [103] since the existence of any charge traps break the system's symmetry. However, such a symmetric behaviour is not observed in all cases since some of the Schottky gates are leaky in one bias direction. In such cases, the applied bias has no observed effect on the optical spectra.

6.2.1 Single exciton Stark shift

In Figure 6.4, the peak positions of X^0 $(s-s)$ as a function of the lateral electric field for both bias directions (open circles) at higher spectral resolution is shown. The experimental data are compared with estimates computed using confinement energies typical of InAs/InP quantum dots (solid blue line). In these estimates, the single-particle Stark shifts of the electron and hole energies is included, but Coulomb interactions are neglected. Data are given for an electric field range of ± 10 kV/cm in which the X^0 $(s-s)$ transition retains its finite oscillator strength. The electric field is calibrated using the fitting procedure discussed in Section 6.4, which suggests that that electric field screening effects are minimal for the data presented here. From a quadratic fit of the data (Figure 6.4, solid red line) using the following expression, $E = E_0 + pF + \beta F^2$ [101], a polarizability of $\beta = 0.31$ μeV cm^2/kV^2 is obtained, *i.e.*, more than two orders of magnitude smaller than the value of $\beta = 144$ μeV cm^2/kV^2 estimated theoretically (Figure 5.5(a)). In this expression for the quadratic fit of the data, E_0 is the energy at $F = 0$, p is the built-in dipole at zero electric field, and the last term arises from the quantum confined Stark effect.

After including Coulomb interaction for the electron and hole, the single particle Stark shift is strongly compensated (see Section 5.3). The calculated polarizability including Coulomb interactions is $\beta = 30$ μeV cm^2/kV^2. Although the magnitude of

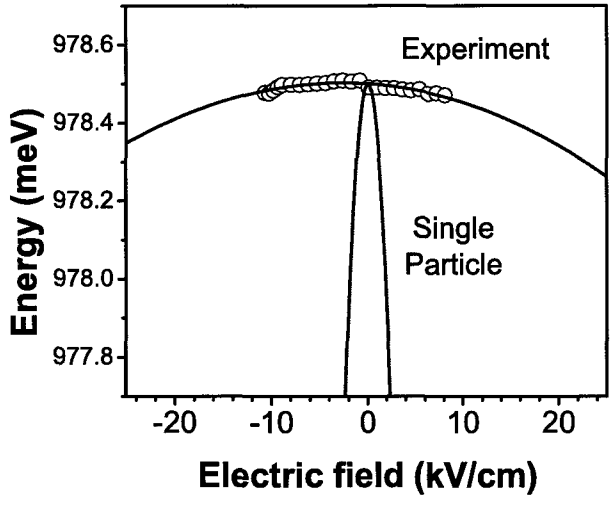

Figure 6.4: Comparison of calculated single particle Stark shift (solid blue line) and measured Stark shift (open circles) for the single, neutral exciton ground state, X^0, in an applied lateral electric field. The solid red line is a quadratic fit to the measured data [26].

the calculated Stark shift is stronger than the one measured experimentally, small changes in the confinement energy for electrons and holes reduces β by a factor of five. As discussed previously in Section 5.3, the reduction of the Stark shift from the single particle picture is governed by a detailed balance of single-particle energies and electron-hole Coulomb interaction. This balance depends strongly on the details of confinement energies for electrons and holes and their effective mass. Since the electrons and holes are effectively separated by the applied lateral field, the electron-hole Coulomb interaction decreases rapidly and compensates the single particle Stark shift. The calculated polarizability does not reproduce the experimentally observed Stark shift, but the strong reduction in the Stark shift as compared to the single particle picture accounts for the small energy shift observed in Figure 6.3. A more accurate estimate of the expected polarizability requires a detailed understanding of the size and shape of the dot confinement potential, for example.

The reduction in Stark shift observed in a lateral electric field is not expected in a vertical field. For typical quantum dot heights ($\sim 3-5\,\mathrm{nm}$), there is only one vertical subband. Coulomb induced scattering to higher subbands, stimulated by the vertical electric field, is highly inefficient because of the large energy separation ($\hbar w_e = 100\,\mathrm{meV}$, and $\hbar w_h = 50\,\mathrm{meV}$ for InAs/InP quantum dots) and cannot be invoked as a means to reduce the Coulomb interaction. Coulomb scattering between harmonic oscillator states within the lowest vertical subband is forbidden for a vertical electric field. As a result, the Stark shift in a vertical electric field is dominated by the single particle effect, which explains good agreement between the estimated and measured exciton polarizability. Single-particle estimates for the polarizability in vertical fields are $\beta = 2.1\ \mu\mathrm{eV\,cm^2/kV^2}$ for InAs/InP quantum dots and $\beta = 0.81\ \mu\mathrm{eV\,cm^2/kV^2}$ for InGaAs/GaAs quantum dots. These estimates are only slightly larger than the measured values of $\beta = 1.7\ \mu\mathrm{eV\,cm^2/kV^2}$ for a single InAs/InP quantum dot and $\beta = 0.66\ \mu\mathrm{eV\,cm^2/kV^2}$ for a single InGaAs/GaAs quantum dot [3].

From the symmetric behavior of the ground state X^0 $(s-s)$ in Figure 6.4, a static dipole for the neutral exciton of $p = 3.2 \times 10^{-30}\ \mathrm{C\,m}$ is obtained. This corresponds to a zero-field, electron-hole separation of $\sim 0.02\,\mathrm{nm}$ in the lateral direction. This result is compared with a zero-field electron-hole separation of $\sim 0.5\,\mathrm{nm}$ for single InGaAs/GaAs quantum dots subjected to vertical electric fields [3]. The small static dipole measured here suggests near reflection symmetry for the in-plane direction of single InAs quantum dots on the InP nanotemplate.

6.2.2 Allowing forbidden s-p transitions at finite bias

The energies of the $s-p$ transition peak extracted from Figure 6.3 as a function of positive lateral electric field is shown in Figure 6.5 (identical behavior is found for

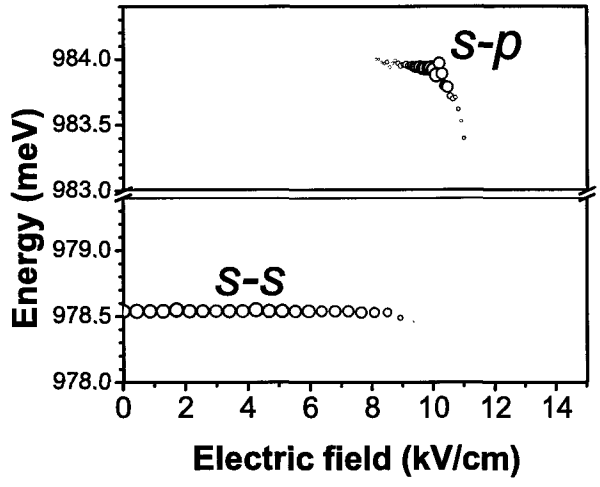

Figure 6.5: Measured emission maxima for the $s-p$ transition appearing under applied bias (open blue circles) and of the $s-s$ ground state transition (open red circles). The size of the symbols represent the normalized integrated intensity [26].

the opposite field direction). The polarizability of the $s-p$ transition is found to be $108\,\mu\text{eV}\,\text{cm}^2/\text{kV}^2$, which is in very good quantitative agreement with the theoretically estimated value of $\beta = 130\,\mu\text{eV}\,\text{cm}^2/\text{kV}^2$ from Section 5.3.3. Better agreement between theory and experiment is obtained for the $s-p$ transition compared to that of the $s-s$ transition since the e-h Coulomb interaction term is significantly smaller at finite fields than at zero electric field. The smaller e-h Coulomb interaction term leads a value of β for the $s-p$ transition that is closer to the single particle picture and does not compensate the single particle Stark shift as strongly as for the $s-s$ transition.

In the eight dots studied, the measured Stark shift of the extra emission peak appearing at higher energy ($s-p$) was larger than that of the $s-s$ transition in all cases. This result excludes the possibility that the new, field-induced transition is a result of a charged exciton feature since the Stark shift of charged excitons was calculated to be similar to that of the $s-s$, neutral exciton (see Section 5.5).

6.3 Fine-structure splitting

To further exclude the possibility of charged excitons within the present experiments, another dot (QD2) is investigated in which the fine-structure splitting is observable at zero applied bias using higher spectral resolution. Photoluminescence data from QD2 as a function of the lateral electric field are shown in Figure 6.6(a). At 0 V bias, transitions from the two neutral exciton states, split by e-h exchange, are observed around 922.4 meV (1344 nm) with a separation of 108 μeV. The fine structure, or asymmetric exchange splitting (AES) of the two peaks as a function of electric field (bias) is shown in Figure 6.6(b) (solid circles). With increasing bias, the AES diminishes, reaching a level of 56 μeV at 1.5 V. Beyond 1.5 V, the AES is below the instrumental resolution (50 μeV - dotted red line) and the oscillator strength of the X^0 decays monotonically. Both the value of the AES and its reduction with applied field are consistent with the behaviour observed previously for single excitons confined in InAs/GaAs quantum dots by Kowalik and colleagues [42]. In that work, an in-plane electric field was used to tune the AES from 140 μeV to 60 μeV, which is very similar to the AES tuning range presented here.

In Figure 6.6(b), the calculated AES (solid black line) is compared to the measured one (solid blue circles) as a function of lateral electric field. Details of the calculations are presented elsewhere [27]. The observed behaviour is traced to the electric-field induced separation of the electrons and holes, which decreases the magnitude of the electron-hole exchange elements responsible for AES. The dependence of AES as a function of the field for displaced electron and hole harmonic oscillator states is [27]

$$\Delta_{AES}(F) = \Delta_{AES}(F=0) exp\left[-\frac{\Delta x}{4l_e^2}\right]. \tag{6.1}$$

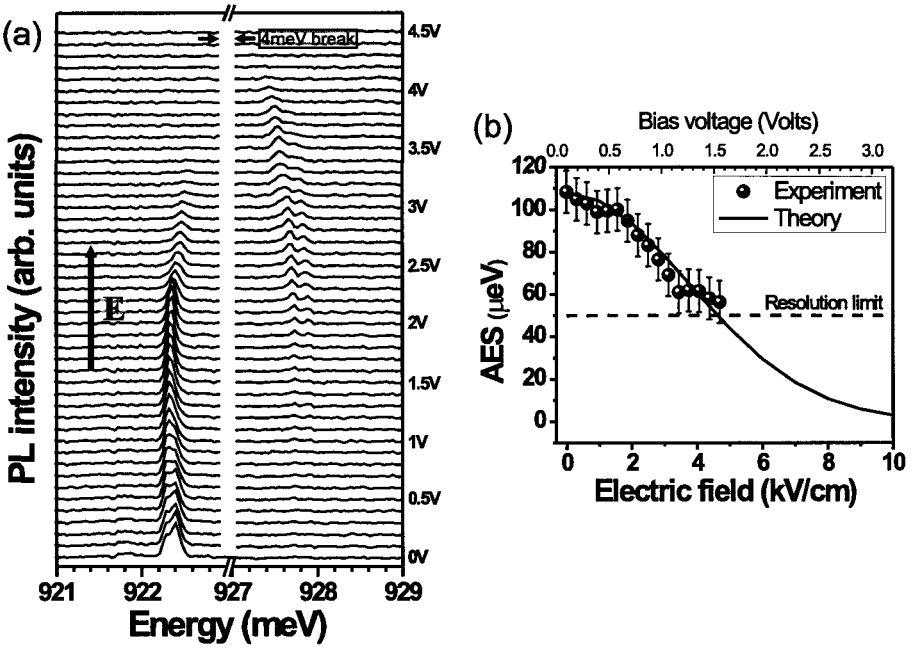

Figure 6.6: (a) Electric field-dependent high-resolution PL spectra measured with a quantum dot exhibiting the anisotropic exchange splitting. (b) Analysis of fine structure splitting (AES) from (a) as a function of lateral electric field. Excellent agreement between the measured AES (closed blue circles) and calculated AES (solid black line) is obtained, thus verifying the assignment of observed transitions [26].

Here, $\Delta_{AES}(F = 0)$ is the AES at zero applied electric field (108 μeV for QD2); Δx is the separation of the electron and hole which is dependent on the field and l_e is the oscillator length. The result of the calculation for $\Delta_{AES}(F)$ is in excellent agreement with experiment, thus confirming the assignment of the $s - s$ neutral exciton transition in the measured data. The reduction in AES is attributed to the field induced separation of carriers by the lateral electric field and the corresponding decrease in electron-hole overlap [64]. Of particular importance is the dependence of the AES on lateral electric field. Other schemes rely on removal of the AES with a lateral electric field for the generation of entangled photon pairs [42, 47–49]; however, it is clear from Figure 6.6(b) that the electron-hole overlap of the quantum

dot ground state transitions are significantly reduced at the electric field required to remove the AES. This result corresponds to a situation in which the optical transitions contributing to the generation of entangled photon pairs are not very efficient for device applications. Thus, for scalability, an alternate method that does not require the removal of AES is required. Such a scheme is discussed in Chapter 7.

In addition to the reduction of the AES and oscillator strengths of the ground state transitions by the applied lateral field, the average of the emission energy for the two AES split peaks exhibits a small red shift with increasing bias. At approximately 1.9 V, a blue shifting peak is observed, at an energy of approximately 922.4 meV. This peak is attributed to the onset of biexciton emission, corresponding to a situation in which the lifetime of the ground state X^0 is increasing rapidly under applied field [25]. The blue shift of the biexciton is confirmed by theoretical calculation (see Section 5.4) suggesting that it is possible to obtain degeneracy between the biexciton and exciton transitions. The appearance of the blue shifting transition is accompanied by a quenching of the ground state transitions involving s-shell electrons and s-shell holes with the simultaneous appearance of the $s-p$ forbidden transition involving s-shell electrons and p-shell holes at $\sim$ 5 meV higher energy. In the voltage range from approximately 1.5 V to 4 V, two additional transitions around 927.5 meV are observed instead of only one $s-p$ transition, as discussed previously. The splitting of $\sim 200\,\mu$eV for these two peaks is larger than the expected AES at this field since the exchange splitting for the ground state X^0 is already below the spectral resolution of the experiment ($< 50\mu$eV) and the e-h exchange involving s- and p-shell states is expected to be smaller than e-h exchange involving both the electron and hole in the quantum dot s-shell [9]. The appearance of two features instead of the anticipated

one can be explained by the dot asymmetry leading to the misalignment of the hole p_x and p_y orbitals with respect to the direction of applied field. Note that the observed splitting for the higher energy peak would not be present for the ground state of a charged exciton species in the singlet configuration, but is fully explained with the interpretation involving an s-shell electron and p-shell hole.

6.4 Electric field calibration

Figure 6.7 shows a comparison, as a function of lateral electric field, of the measured integrated intensity of the peaks shown in Figure 6.6 with the calculated strength of the emission maxima presented in Section 5.3. Here, the integrated intensities of the two exchange split peaks are added together to comprise the $s-s$ transition. To find the calibration between the experimental bias voltage ΔV and the electric field F used in the calculations, the maximum intensity of the measured $s-p_x$ is aligned with the theoretical maximum e-h overlap calculated in Figure 5.3. After assuming a linear relationship between this aligned bias voltage and electric field, excellent agreement is obtained between the measured intensity (open symbols) and calculated strength of transitions (solid lines). The $s-s$ transition intensity decreases monotonically with increasing electric field, while the $s-p_x$ transition becomes allowed for finite fields.

To confirm the validity of the calibration procedure for the electric field, the electric field is calculated between the two electrodes using the approach of J. Seufert and co-workers [102]. Here, the electrodes are assumed to be separated by a distance d and the dot is an infinite, thin slab between the electrodes with a thickness much less than d. For such an approximation, the electric field, F, applied across the quantum dot is $F = \Delta V/\varepsilon d$. Here, $\varepsilon = 12.4$ is the dielectric constant of InP. This simple

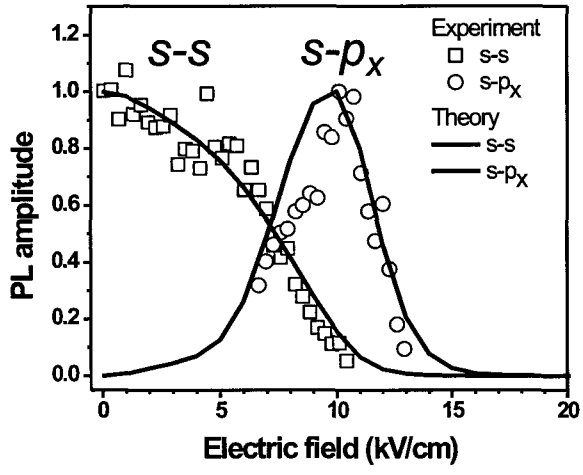

Figure 6.7: Field calibration in a lateral electric field. Measured (open symbols) and calculated (solid lines) emission intensity as a function of lateral electric field for the ground $s-s$ (red) and first excited $s-p_x$ (blue) exciton states. The field is calibrated by aligning the $s-p_x$ transition from experiment and theory with a one to one scaling [26].

scaling of the electric field agrees with that used in Figure 6.7 to within 7%.

6.5 Conclusion

These results demonstrate a post-growth tuning technique that allows one to electrically manipulate the electronic properties of individual, site-selected InAs/InP quantum dots. Photoluminescence data as a function of applied lateral electric field show an excitonic Stark shift that is two orders of magnitude smaller than that expected from single particle calculations. The polarizability of the ground state transition ($\beta = 0.31\,\mu\text{eV}\ cm^2/kV^2$) is understood through the exponential decay of the electron-hole Coulomb interaction under applied lateral electric field. The polarizability of the excited state involving an s-shell electron and p-shell hole is larger than the ground $s-s$ exciton state in all samples studied. The magnitude of the $s-p$ transition was found to be in excellent quantitative agreement with theory since the e-h Coulomb

interaction is significantly reduced at finite fields and therefore closer to the single particle picture. The observed modification of oscillator strengths for the excitonic transitions and the appearance of a normally forbidden, excited state of the neutral exciton are in excellent agreement with many body, configuration-interaction calculations of the emission spectra from Chapter 5. The number, position, Stark shift and fine structure of the emission peaks observed in experiment allows the presence of charged excitons appearing in a lateral electric field for these samples to be excluded.

An ability to electrically switch between the ground state and forbidden transition is expected to find application in advanced single photon sources or electron-spin resonance techniques. The forbidden transition can be used as an intermediate state to trigger the single photon source based on the exciton to vacuum optical transition. Alternatively, the lateral electric field can be used to increase the lifetime of the exciton (forbidden transition) to prolong the amount of time available for spin manipulation.

Finally, the scalable gating technology utilized to apply a lateral electric field to pre-positioned InAs/InP quantum dots presented here offers the possibility to create arrays of entangled photon pair sources on demand without the requirement to remove the fine-structure splitting, which is a major problem with existing devices. The method to overcome the need to enforce the degeneracy of the intermediate exciton states (*i.e.*, removal of fine-structure splitting) in the biexciton-exciton radiative cascade is circumvented by removal of the biexciton binding energy, as proposed recently [25, 27] and discussed in the following chapter.

Chapter 7

Generation of entangled photon pairs

Quantum mechanics allows pairs of optical photons to be joined together in such a way that changes made to one photon can be felt instantaneously by the other, even when they are separated by large distances. This correlated 'action at a distance' is at the heart of quantum computation and is fundamental to the development of quantum cryptographic systems that seek to share information more securely through manipulation of these photon pairs. Such photon pairs are said to be entangled and are viewed as a necessary requirement for quantum information applications including: secure quantum communication [104–107]; quantum repeaters [106]; controlled quantum logic gates [108] and; quantum teleportation [109].

Entangled photons can be generated by parametric down conversion within a non-linear crystal such as beta-barium borate (BBO) [110]. The major problem with such a scheme is inefficiency: approximately 1 out of 10 billion photons incident on the BBO crystal are down-converted and of these down-converted photons, even fewer are entangled [110]. At the same time, since the distribution of parametric down-converted photons follows Poissonian statistics [111], this inefficiency is accompanied

by a non-vanishing probability for emitting two or more pairs of photons. As an alternative to parametric down conversion, the biexciton-exciton radiative decay cascade within a single semiconductor quantum dot can be employed as a source of triggered, polarization entangled photon pairs [112]. Here, the source generates exactly one entangled photon pair per excitation pulse. After recombination of the two electron-hole pairs that form the biexciton, the quantum dot system is necessarily in its ground state and therefore cannot emit until the next excitation pulse. A triggered source is desirable as it avoids the possibility of multiple photon emissions and possible attacks to the secure quantum communications system [106]. To date, a fidelity of approximately 70 % has been achieved for the degree of entanglement in semiconductor quantum dots. This represents a substantial improvement over previous methods and constitutes a significant step towards the practical realization of polarization entangled photon pair sources [113]. In the demonstration of entangled photon pairs with high fidelity, the quantum dot was embedded within a planar microcavity, improving the light collection efficiency by an order of magnitude over that previously obtained for a single quantum dot [113].

Current proposals for the generation of entangled photon pairs using the biexciton-exciton-vacuum cascade within semiconductor quantum dots rely on the removal of the fine-structure splitting of the intermediate exciton states [42–51]. However, entanglement in these schemes is destroyed when the degeneracy of the two possible spin configurations of the intermediate neutral exciton ground state is lifted, as is frequently the case in the presence of electron-hole exchange splitting in anisotropic

quantum dots [64]. As such, many efforts are underway worldwide to develop techniques for removal of the anisotropic exchange splitting (AES) for the exciton. This removal has been demonstrated through the application of external magnetic fields [44], spectral filtering [45], quantum dot size and composition engineering through various growth techiques [43, 46, 51], or application of in-plane electric fields [42, 47–49]. To date, these efforts have been limited to randomly located quantum dots, a constraint which is addressed in this thesis.

In the work presented here, an alternative scheme for quantum dot entangled photon pair generation is proposed that is robust to the presence of the anisotropic exchange splitting. A gate-induced, lateral electric field tuning of the photon energies obtained from biexciton and exciton decay is demonstrated for a deterministically positioned quantum dot. Under certain conditions the binding energy of the biexciton is shown to vanish and it is possible to identify two indistinguishable recombination pathways for the biexciton, even in the presence of non-degenerate intermediate exciton states. The observed behavior provides a voltage controlled route to entangled photon pair generation even from imperfect quantum dots, without resorting to large external magnetic fields or materials engineering of individual dots. In addition, the scheme proposed here eliminates the major problem of existing devices based on in-plane electric fields, where the electron-hole overlap of the quantum dot ground state transitions are significantly reduced at the electric fields required to remove the AES (see Section 6.3).

The gate-induced control necessary to envision polarization entangled photon pairs can be achieved by precisely balancing the competing Coulomb attractions and repulsions for excitons (X) and biexcitons (XX) within a single, prepositioned InAs/InP

quantum dot using an applied lateral electric field. For the quantum dots discussed here, additional benefits accrue since they emit close to 1300 nm, or even 1550 nm under appropriate conditions, and are prepared using a technique that allows their nucleation position to be controlled *a-priori* (see Chapter 3). Such structures are ideal for fibre-based quantum cryptographic systems and are of immense promise for gate controlled, integrated semiconductor entanglement sources for quantum repeater technologies [24].

Additionally, the ridge nanotemplate that controls the quantum dot nucleation site is determined to affect the biexciton binding energy. Here, the biexciton binding energy can be controllably tuned from a bound to unbound XX state and over a large energy range of 7.1 meV. Such control is accomplished via appropriate choice of the growth conditions including ridge nanotemplate dimensions and amount of dot material deposited. By comparison to previous reports [89–91, 114–116] and model calculations [114,117], the unbound XX regime can be attained by piezoelectric fields in large quantum dots – a regime not previously achieved. The separation of charges required to produce an unbound XX state by piezoelectric fields in large quantum dots is also expected to produce fine-structure splittings near zero, thus allowing the possibility of producing arrays of entangled photon pairs near the telecommunications band around 1.55 μm.

The remainder of this chapter is organized as follows. In Section 7.1, the current method to generate entangled photon pairs that relies on degenerate intermediate exciton states in the biexciton-exciton radiative cascade is introduced. A new scheme to overcome the limitation of entangled photon pair generation through degenerate exciton states is presented in Section 7.2. Section 7.3 discusses the experimental

method of identifying exciton and biexciton optical transitions in experiment, which are necessary for verifying a single dot and selecting samples for entangled photon generation. In Section 7.4, removal of the biexciton binding energy is demonstrated for a single, prepositioned quantum dot subject to a lateral electric field. The controlled tunability of the biexciton binding energy via the ridge nanotemplate and its importance for the production of entangled photons near the telecommunications band around $1.55\,\mu$m is discussed in Section 7.5. Finally, in Section 7.6, the main conclusions are summarized.

7.1 Biexciton-exciton radiative cascade

The biexciton, XX, decays to vacuum through one of two possible channels (channel A or B) as shown schematically in Figure 7.1(a), with two states of the neutral exciton, X_1 and X_2, as possible intermediate exciton states. Within present proposals for quantum dot entangled photon pair sources, the energetics of the intermediate exciton states play a crucial role in determining if the pair of photons emitted from the biexciton decay cascade is indeed entangled. In a typical, strained quantum dot, the heavy- and light-hole degeneracy is lifted, so that the exciton ground state is primarily of heavy-hole character [52]. The bright exciton intermediate states can then be constructed from $J_z = \pm 3/2$ single particle hole states and $S_z = \pm 1/2$ single particle electron states to yield two bright excitons with a total angular momentum of ± 1. In an idealized quantum dot, the confining potentials for electrons and holes are rotationally symmetric, so that angular momentum is a good quantum number. In such circumstances, the two bright exciton states, X_1 and X_2 are degenerate (*i.e.*, AES = 0). Here, transitions from the biexciton to exciton and exciton to vacuum

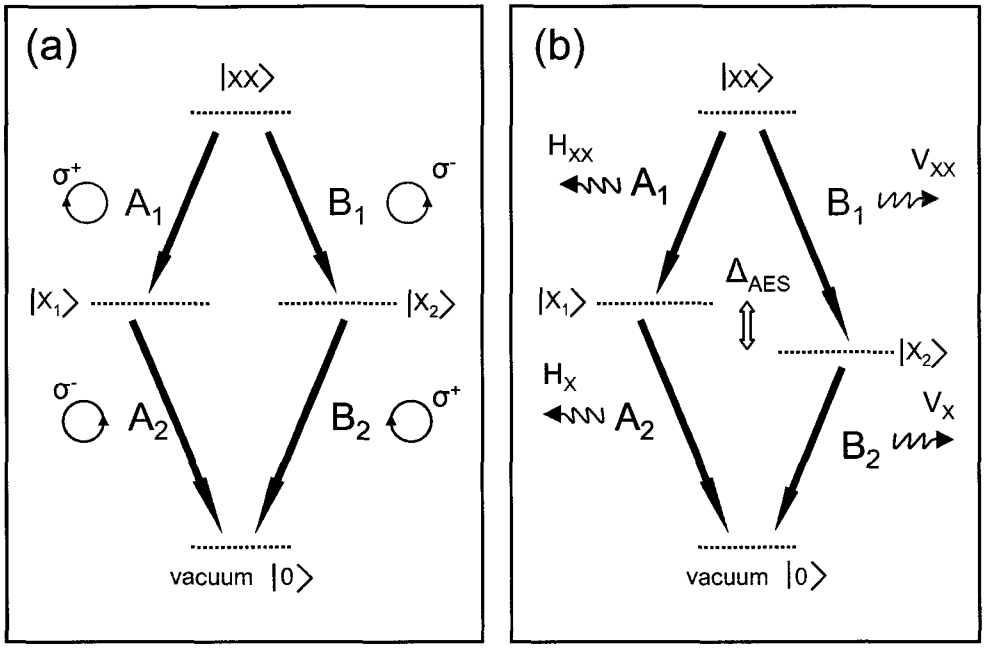

Figure 7.1: Present method for entangled photon pair generation utilizing the biexciton-exciton radiative cascade. (a) Circular symmetric dot in which $\Delta AES = 0$. In such circumstances, a photon energy measurement cannot distinguish the path and polarization entangled photons are produced. (b) Quantum dot in presence of anisotropic exchange splitting ($\Delta AES \neq 0$). Here, the presence of AES destroys the entanglement since the photon energies in each recombination pathway (A or B) can be distinguished by a measurement.

produce either left (σ^-) or right (σ^+) circularly polarized photon emission depending on the spin configuration of the electron-hole pair that recombines [112]. The photons are emitted in the cascade without any specific requirement on the biexciton binding energy. In this case, the two photon wavefunction is entangled in the polarization degrees of freedom,

$$\Psi = \frac{1}{\sqrt{2}} \left(\sigma^+ \sigma^- + \sigma^- \sigma^+ \right), \tag{7.1}$$

since a measurement of the photon energies will not serve to distinguish the two possible decay channels and probability amplitudes must be added.

In quantum dots fabricated by self-assembly, however, the rotational symmetry

of the electron and hole confining potentials is frequently lost. Under these circumstances, the degeneracy of the intermediate exciton states, X_1 and X_2 is lifted because of the anisotropic electron-hole exchange interaction [64] and the techniques utilized within existing proposals to remove the AES must be attempted if the possibility of two-photon entanglement is to be regained. The biexciton-exciton radiative cascade in the presence of AES is presented in Figure 7.1(b). It is evident from a photon energy measurement that the recombination pathway, A or B, can be distinguished and therefore destroys the entanglement. The two channels for biexciton decay (A and B) are made indistinguishable again by setting $\Delta_{AES} = 0$, so that transitions A_1 and B_1 in Figure 7.1(b) become degenerate, as well as transitions A_2 and B_2, thus restoring the schematic depicted in Figure 7.1(a). Removal of the AES for arrays of individual QDs is technologically difficult since the application of large magnetic fields [44] or compositional modifications [43, 46, 51] cannot be accomplished locally on a dot to dot basis. In addition, for methods based on electric fields [42, 47–49], the optical transitions of the emitted photons in the biexciton-exciton cascade are significantly reduced at fields required to remove the AES and, in most cases, have quenched. The proposed scheme to overcome these limitations is discussed in the next section.

7.2 Proposed entangled photon pair scheme

The major problem of existing devices to produce entangled photon pairs utilizing the biexciton radiative cascade in semiconductor quantum dots is the need to enforce the degeneracy of the intermediate exciton states (*i.e.*, $\Delta AES = 0$). The question arises as to whether there is an alternative scheme to produce entangled photon pairs from

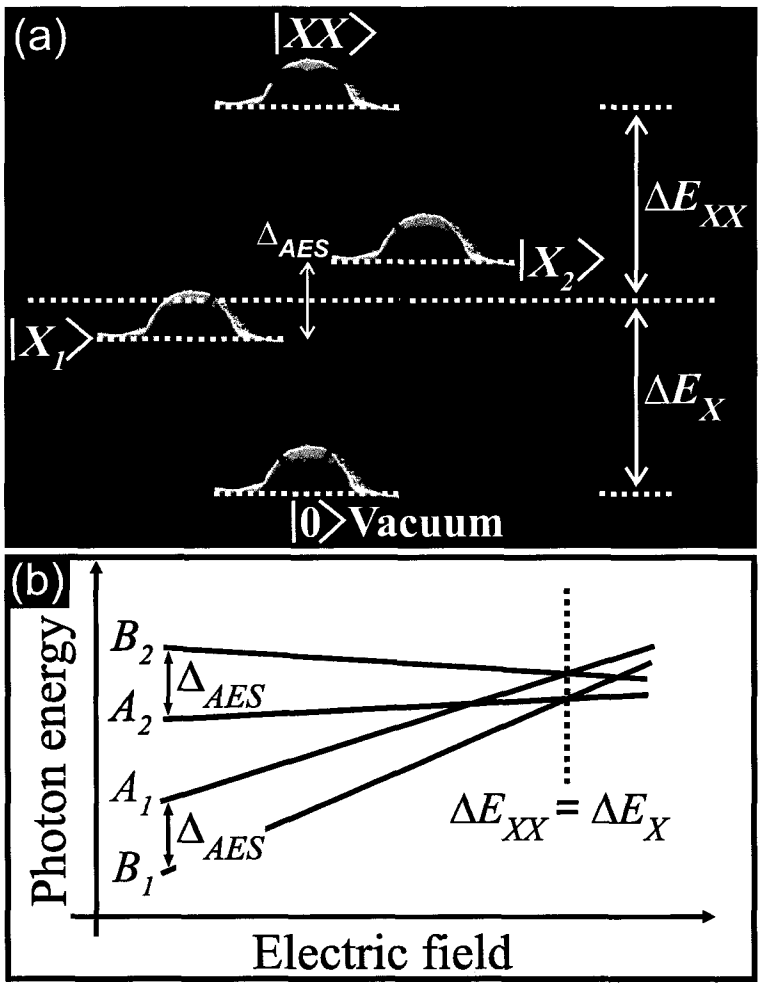

Figure 7.2: Polarization entangled photon source exhibiting exchange splitting. (a) Schematic diagram of the biexciton-radiative cascade for a polarization entangled photon source exhibiting an anisotropic exchange splitting (AES) when the binding energy of the biexciton is tuned to zero ($\Delta E_{XX} = \Delta E_X$). Two possible decay paths exist from the biexciton $|XX\rangle$ to vacuum $|0\rangle$ through the intermediate, non-degenerate excitonic states $|X_1\rangle$ and $|X_2\rangle$. The solid lines with arrows indicate transitions with energy A_1 (green), A_2 (red), B_1 (purple) and B_2 (blue). The two possible decay paths of the $XX - X$ cascade are represented by A and B, whilst the subscript 1 (2) denotes the first (second) photon emitted in the cascade. (b) Schematic view of transitions in (a) as a function of lateral electric field with the same colour scheme for transitions. For the case when $\Delta E_{xx} = \Delta E_x$, the biexciton binding energy vanishes and a polarization entangled photon pair is possible, even in the presence of exchange splitting.

the biexciton decay that does not require removal of the AES splitting – a requirement that the scientific community is attempting to overcome. The proposed scheme to resolve this issue is shown schematically in Figure 7.2(b). Each photon emitted in the biexciton cascade is represented by a different colour, defined in 7.2(a). In a situation in which the biexciton is at lower energy, the electric field will manipulate the binding energy of the biexciton, such that the exciton and biexciton transitions cross at finite field, *i.e.*, the condition $\Delta E_{XX} = \Delta E_X$ is satisfied as defined in Figure 7.2(a). At the electric field where the biexciton binding energy is removed (*i.e.*, XX PL transition is degenerate with the X one), two pairs of degenerate transitions can be identified even in the presence of a non-zero AES: A_1 and B_2, as well as A_2 and B_1. The resulting degeneracy results since both recombination pathways decay from the same initial state $|XX\rangle$ to final state $|0\rangle$. This expected degeneracy restores the indistinguishability of the biexciton decay channels and suggests that arrays of individually addressable, voltage controlled quantum dots would be able to provide multiple sources of entangled photons, in which the two-photon wave function is entangled in the horizontal (H) and vertical (V) polarisation degrees of freedom,

$$\Psi = \frac{1}{\sqrt{2}} \left(H_{XX} H_X + V_{XX} V_X \right). \tag{7.2}$$

Within the proposed scheme it would be possible, in principle, to distinguish the decay channel if temporal information were available since the biexciton is emitted before the exciton in the decay process. This problem is resolved using subsidiary linear optical elements to restore temporal overlap. An example of one possible, simple scheme for removing the timing information is shown in Figure 7.3. The two branches of the biexciton decay will produce photon pairs of either vertical (V) or horizontal (H) polarization. The different polarization for the two branches allows the separation

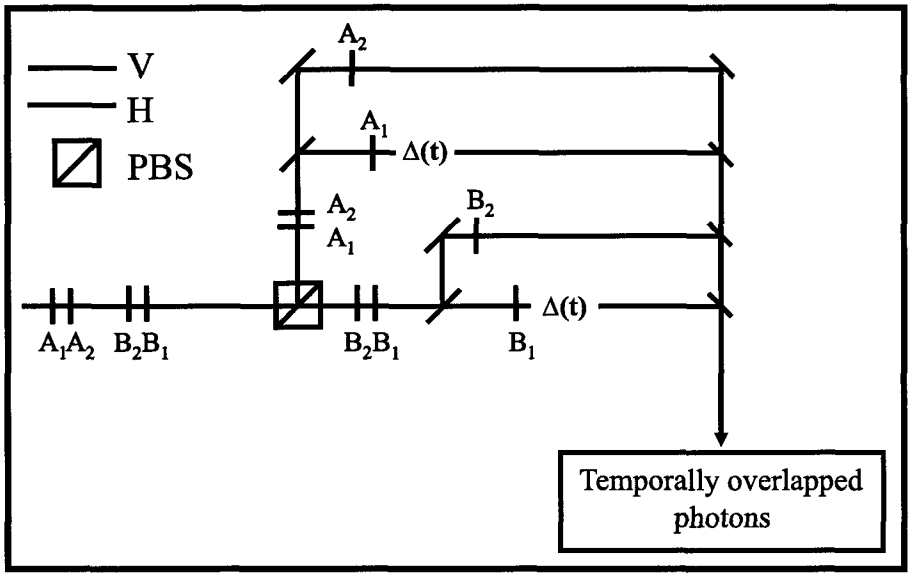

Figure 7.3: Removal of timing information in entangled photon pair proposal. Entanglement is destroyed if timing information were available. The proposed scheme involves linear optical elements to restore temporal overlap and therefore restoring entanglement.

of photons from either branch using a polarizing beamsplitter (PBS) and then acts to remove timing information on either branch. Taking one of the recombination pathways for example, photons of energy A_1 precede photons of energy A_2 due to the order of emitted photons in the biexciton cascade (*i.e.*, biexciton is emitted before that of the exciton). In the case of the other branch, the B_1 photon is emitted before the B_2 photon. In either case, the delay between the two photons can be erased by separating them energetically (A_1 and A_2 or B_1 and B_2) and then delaying one with respect to the other. Once the photons are bought back together again, the timing information is removed.

A theoretical investigation of time reordering for restoring entanglement can be found in the work of Avron *et al.* [118] and Pfanner *et al.* [119]. In this work, the degree of entanglement possible is discussed. Pfanner and coworkers suggest that

when filtering the emitted photons in the biexciton-exciton cascade, the degree of entanglement would remain low due to dephasing processes in the solid such as interactions with phonons [119]. In contrast, with no filtering and $\Delta AES = 0$, perfect entanglement is obtained within their present model [119]. However, the degree of entanglement, which is possible within the proposed scheme, remains to be tested experimentally and is very promising for the scientific community that have been struggling to reliably remove the AES. If successful, this would represent a significant step towards the practical realization of entangled photon pairs utilizing a scalable architecture.

7.2.1 Criteria for entangled photon pair generation

For the above-mentioned scheme to be feasible, the following criteria must be met:

1. remove biexciton binding energy while maintaining finite oscillator strength of optical transitions (*i.e.*, $\Delta XX = 0$);

2. achieve precise control of electric field – exciton and biexciton cross-colour transitions must be tuned within their natural linewidth (*i.e.*, within approximately $1\,\mu$eV);

3. erase timing information such that the which-path information (recombination pathway) cannot be distinguished; and

4. minimize timing jitter of emission photons and dephasing rates [119].

7.3 Identification of exciton and biexciton in experiment

To identify the exciton and biexciton in experiment, a combination of both power (state-filling spectroscopy) and polarization dependent spectroscopy of the observed photoluminescence (PL) emission spectra is conducted, similarly to previous reports [89–91]. Power dependent PL spectroscopy using non-resonant excitation provides information about average number of excitons in the dot [80, 89–91] while polarization of the emission for biexciton and exciton can be used to confirm the assigned excitonic transitions [44,45,89–91]. In addition, however, the electric field dependence studied in this thesis can be used as an additional experimental tool to identify the exciton and biexciton since Coulomb interactions play an important role. Coulomb interactions are ascertained to be manipulated very strongly in a lateral electric field in strong contrast to vertical fields (see Chapter 6). Consequently, the exciton and biexciton exhibit unique signatures (*i.e.*, Stark shifts, fine-structure, life time, *etc.*) as a function of lateral electric field, which allows the biexciton-exciton cascade to be differentiated from all other cascades including charged excitonic states allowing practical implementation [27].

7.3.1 Power dependent photoluminescence spectroscopy

In the power dependant PL data presented in Figure 7.4, both samples (QD3 and QD4) exhibit typical state-shell filling spectroscopy as a function of increasing pumping power [29, 80] (see Chapter 4). First, only a single emission peak is observed, which is attributed to X. Further increase of the excitation power results in XX emission either below (bound) or above (unbound) X as shown in Figure 7.4(a) and

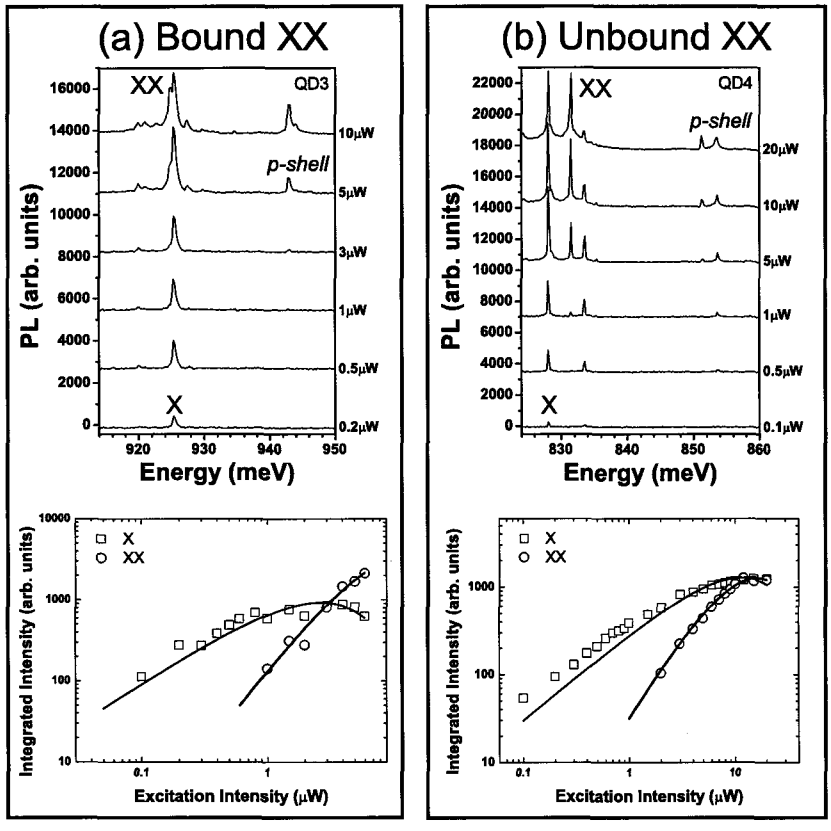

Figure 7.4: Typical state-shell filling spectroscopy of (a) bound and (b) unbound biexciton for a single prepositioned quantum dot on ridge nanotemplate at zero electric field. In the lower panel are fits (solid lines) to the data using Equation 4.1. Evidence of exciton and biexciton are inferred from the resulting linear and superlinear power dependence of integrated intensity on excitation power. The saturation of the observed emission peaks are well reproduced within the random capture model.

(b), respectively. Consistent with literature, the binding energy of the biexciton is defined as [89–91]

$$\Delta_{XX} = E_X - E_{XX}. \tag{7.3}$$

Here, a bound biexciton has a positive Δ_{XX} and is found at lower energy than X, whereas an unbound biexciton has a negative Δ_{XX} and is at higher energy than X. The definition of unbound does not mean that the biexciton is unbound although

this term is commonly used [91]. Here, the two spatially separated excitons forming the unbound biexciton are still strongly influenced by the confinement potential [91]. The binding energy of the biexciton is a direct result of Coulomb interactions of the two electron-hole pairs building the biexciton and correlations of higher lying states (see Chapter 5). To briefly summarize, the positive contributions to Δ_{XX} arises from e-h Coulomb attraction and correlation effects, while the negative component comes from the Coulomb repulsion between carriers of the same type. Thus, an unbound biexciton can be manifested from a weaker dependence on electron-hole Coulomb interactions than electron-electron and hole-hole Coulomb repulsion and reduction in correlations resulting from either a smaller quantum dot [91] or when the number of bound states decreases [90]. Additionally, strain induced piezoelectric fields in large dots can result in a separation of charges, thus leading to an unbound biexciton state [114, 116]. See Section 7.5 for more details of dependence of biexciton binding energy on quantum dot size. In the two dots presented here, the binding energy of the bound biexciton is $\Delta_{XX} = +0.8\,\text{meV}$ (Figure 7.4(a)) and unbound biexciton is $\Delta_{XX} = -3.4\,\text{meV}$ (Figure 7.4(b)).

The extra peak at slightly higher energy than XX in Figure 7.4(b) is typically observed for the unbound XX case. The energy of this peak is at $\sim$5 meV higher energy than X and is attributed to excitonic recombination of an $s-p$ forbidden transition as described in the previous chapter. Electric field dependent measurements for dots exhibiting an unbound XX state confirms the assignment of this excitonic transition. An example of such an electric field dependence for a dot which exhibits a XX at higher energy with increasing excitation power is shown in Figure 7.5. In contrast to a quantum dot that exhibits a bound XX (see Figure 6.3), the observed

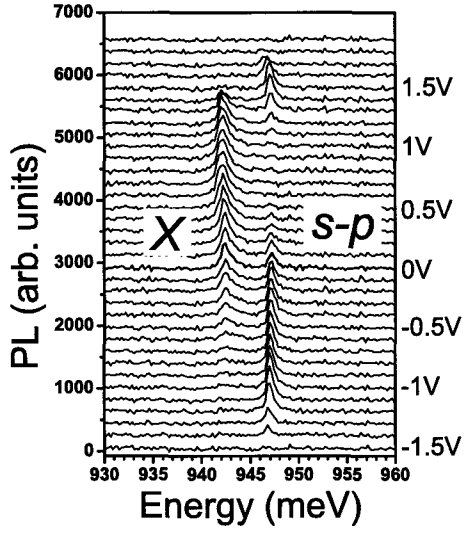

Figure 7.5: Electric field dependence of a single dot exhibiting a built-in charge separation at zero electric field. For this particular dot, an unbound biexciton is observed for increasing excitation power.

optical spectra shown here is asymmetric about 0 V bias and is due to a built-in electric field, which causes a charge separation of electron and hole. Instead, both the X transition and $s-p$ transition are observed at zero applied bias due to this built-in electric field. The separation of charges required to produce an unbound XX suggests that it is possible to have an electron-hole wavefunction overlap of the $s-p$ transition at zero electric field. With increasing lateral field ($-V$), the X transition quenches while the $s-p$ transition grows in intensity and then gradually quenches. In the other field direction ($+V$ lateral), the $s-p$ transition quickly disappears while the X transition grows in intensity. Further increase of the lateral field for positive bias results in quenching of the X transition while the $s-p$ transition appears and then is followed by immediate quenching. Such observed behaviour is consistent with an expected field induced separation of electron and hole resulting in modification of overlapping electron-hole wavefunctions.

Finally, in both dots of Figure 7.4, p-shell emission is observed when the s-shell is completely filled with appearance of satellite peaks about the X and XX line due to s-shell recombination perturbed by the presence of excitons occupying higher lying states in the the p-shell [92].

7.3.2 Polarization dependent spectroscopy

Excitons and biexcitons are identified by power dependent spectroscopy in the previous subsection; however, charged excitons and biexcitons can also exhibit similar dependence on excitation power to that of uncharged X and XX [92]. Therefore, to distinguish neutral complexes from charged ones, additional polarization measurements are made to resolve the fine-structure splitting of the transitions involved in the biexciton-exciton ($XX - X$) radiative cascade. The polarization of the emitted photons in the $XX - X$ cascade is dependent on the recombination pathway through the two intermediate exciton states (see Section 7.1 for more details). Thus, in a quantum dot exhibiting an anisotropic exchange splitting (AES), the emitted photons from the XX and X can be resolved by polarization. In practice, this is accomplished by rotating a half-wave plate polarizer in front of a fixed Glan-Thompson polarizer at the input of the spectrometer (see Chapter 4). A clear optical signature of the $XX - X$ radiative cascade with polarization dependent spectra is evident in Figure 7.6. The observed emission peaks for X and XX are cross polarized doublets with identical splitting but reversed polarization [90]. The reversed polarization obtained for XX and X arises due to the XX having no AES, while X is split by AES. Referring back to Figure 7.2, the vertically (V) polarized photons emitted in the $XX - X$ cascade are B_1 and B_2, while the horizontally (H) polarized photons are A_1 and A_2. The XX

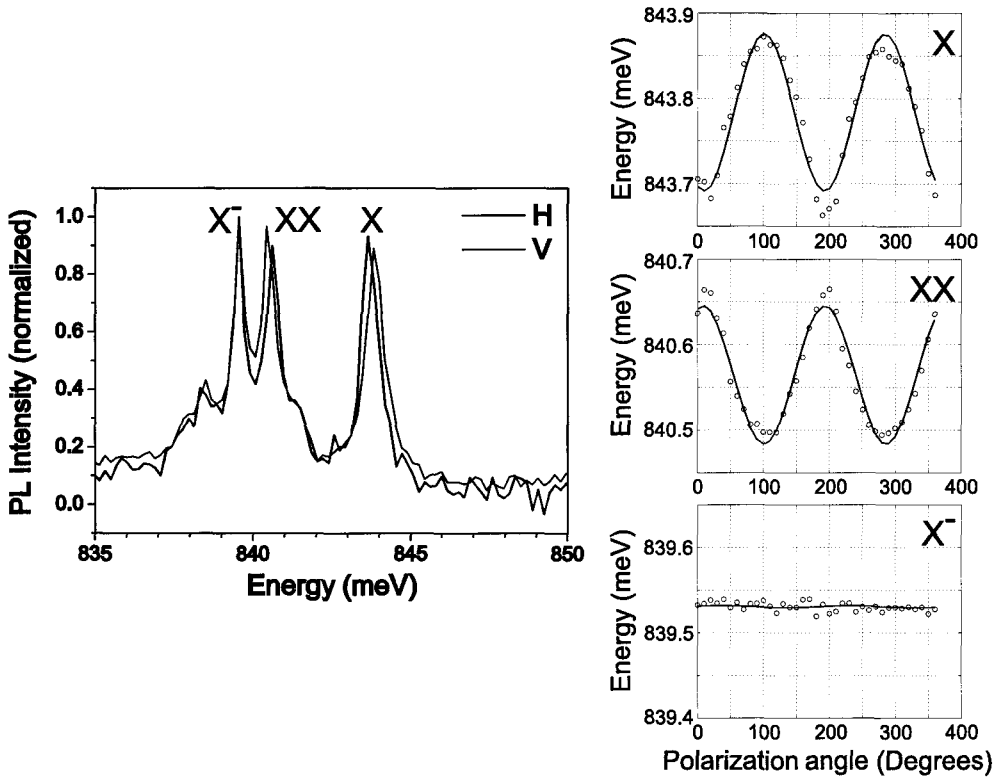

Figure 7.6: Polarization dependence of biexciton-exciton radiative cascade. The exciton and biexciton emission exhibit reversed horizontal (H) and vertical (V) polarizations with identical splitting; an optical signature of single quantum dot containing an anisotropic exchange splitting. From the polarization dependent emission of the exciton (right panel), a fine structure splitting of $185\,\mu$eV is obtained (*i.e.*, $\Delta AES = 185\,\mu$eV). As expected, the singly charged exciton, X^-, has no fine structure splitting.

does not constitute AES since the e-h exchange of the two excitons building the biexciton cancels (*i.e.*, the e-h exchange for one exciton ($\uparrow\Downarrow$) cancels the e-h exchange of the other exciton ($\downarrow\Uparrow$)). The origin of the observed XX splitting in the PL emission spectrum of Figure 7.6 is due to the final state, X, which is split by e-h exchange.

To extract a value for the exciton fine structure splitting, a Lorentzian curve-fitting procedure of the PL peak as a function of a half-wave plate polarization angle at the input of the spectrometer is utilized (right panel of 7.6). Using this method,

fine structure splittings below the spectral resolution could be obtained. The right panel of Figure 7.6 shows the emission energy of X, XX, and X^- (singly charged exciton) as a function of emission polarization angle. For this particular dot, a fine structure splitting of $\Delta AES = 185\,\mu$eV is obtained. As a reference, the polarization dependence of X^- is also shown. Here, no fine structure is observed for X^- as expected [64].

7.4 Removal of biexciton binding energy

To demonstrate the manipulation of the biexciton binding energy and removal at finite lateral electric field, a gated ridge sample comprising of an individual InAs/InP quantum dot is selected which exhibits a negative XX binding energy at zero applied bias. Photoluminescence data from such a dot as a function of the applied lateral electric field is shown in Figure 7.7(a) with the appearance of the XX at lower energy than the X shown in Figure 7.7(b) at zero electric field and higher excitation power. Since this is a very delicate experiment, the excitation power was chosen such that on average the dot occupation is less than one exciton according to Poisson statistics (*i.e.*, only the X peak is observed in PL). When higher excitation power was chosen to observe both the XX and X simultaneously, no effect of the field was obtained. Here, the higher excitation power screened the applied electric field. Although both the XX and X PL transitions could not be observed as a function of applied lateral field for the dots on ridges studied here, this is a possibility for a single dot in a pyramid (see Chapter 8).

At zero applied bias in Figure 7.7(a), transitions from the two neutral exciton ground states, split by e-h exchange, are observed at approximately 922.4 meV

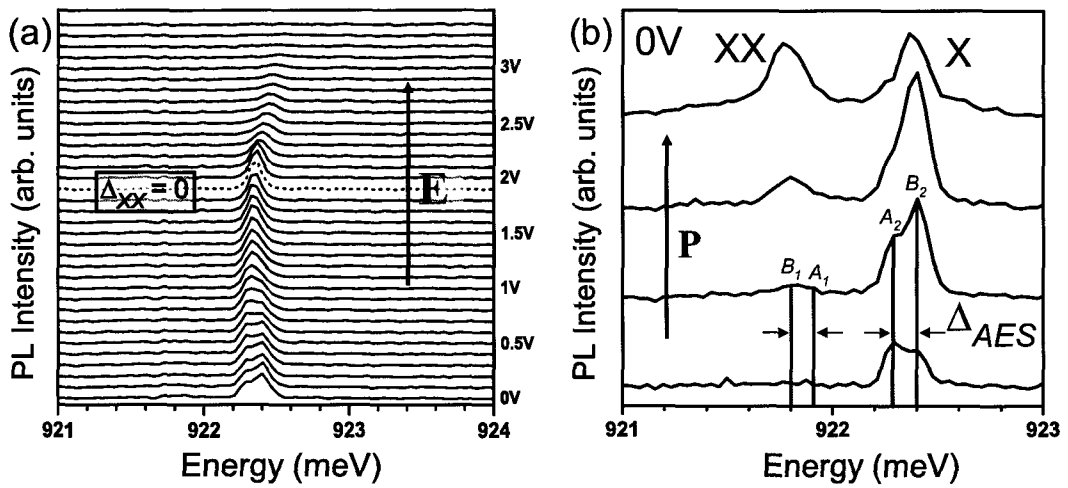

Figure 7.7: (a) Electric field dependent PL spectra from a single quantum dot in a ridge nanotemplate. At finite lateral electric field corresponding to 1.9 V bias, the biexciton binding energy is removed (*i.e.*, $\Delta_{XX} = 0$). (b) At 0 V bias, the XX is observed at lower energy than X and has a binding energy of $\Delta_{XX} = 510\,\mu$eV. The two peaks observed for X at 0 V bias corresponds to the two neutral exciton peaks that are split by e-h exchange.

(1344 nm). For biases from 0 V to approximately 1.9 V, the mean X energy shows a very small Stark shift, consistent with quenching of e-h Coulomb interactions as the electron and hole is separated in a lateral electric field (see Chapter 6). In addition, the AES diminishes from 108 μeV to 56 μeV. Beyond 1.9 V, the AES is below the instrumental resolution (50 μeV) and the oscillator strength of the X decays monotonically. Both the zero field value of the AES and its reduction with the applied lateral field are consistent with the behavior described in the previous chapter. The key feature is observed at the bias voltage of 1.9 V. Here, the main, exchange-split PL line is replaced by a transition that blueshifts as a function of increasing electric field. The change from the observed red-shifting exciton to blue-shifting biexciton in the optical spectrum corresponds to the desired resonance point, in which the biexciton binding energy is removed (*i.e.*, $\Delta_{XX} = 0$) and entangled photon pairs are generated.

7.4.1 Comparison with model calculations

To verify the above identification of spectral features, the calculated photon energies and oscillator strengths (represented as symbol size) calculated in the full configuration-interaction approach for the ground state of exciton (A_1 and B_1 in Figure 7.2) and the biexciton (A_2 and B_2 in Figure 7.2) are shown in Figure 7.8(a). The results of the calculations are compared to the field dependence of the exciton and biexciton energies in Figure 7.8(b), where the peak positions have been extracted from the electric field dependent PL spectra in Figure 7.7(a). This calculated behaviour is in excellent qualitative agreement with the experimental spectrum. As a function of increasing electric field, the A_2, B_2 transitions of the neutral exciton shift down in energy, with the intensity decreasing as the e-h overlap diminishes. The Stark shift of the X lines is very small, much smaller than the Stark shift of a non-interacting electron-hole pair and the exchange splitting is decreasing with increasing electric field. The biexciton transition, on the other hand, shifts upwards in energy, and is brought into resonance with the exciton transition at a finite field of 6.5 kV/cm. This corresponds to two pairs of degenerate transitions, the $A_1 - B_2$ pair and the $B_1 - A_2$ pair, thus leading to polarization entangled photon pairs even in the presence of non-degenerate intermediate exciton states as discussed previously. However, in experiment, either only the X or XX is observed. In the optical spectra in Figure 7.7(a), the exciton transitions split by e-h exchange, A_2 and B_2 are observed before the crossing of X and XX while the observed peak after the crossing corresponds to the XX transition. The fact that the biexciton is observed under applied field for the present experimental conditions is a consequence of the increasing exciton radiative lifetime as the electron-hole overlap diminishes [120].

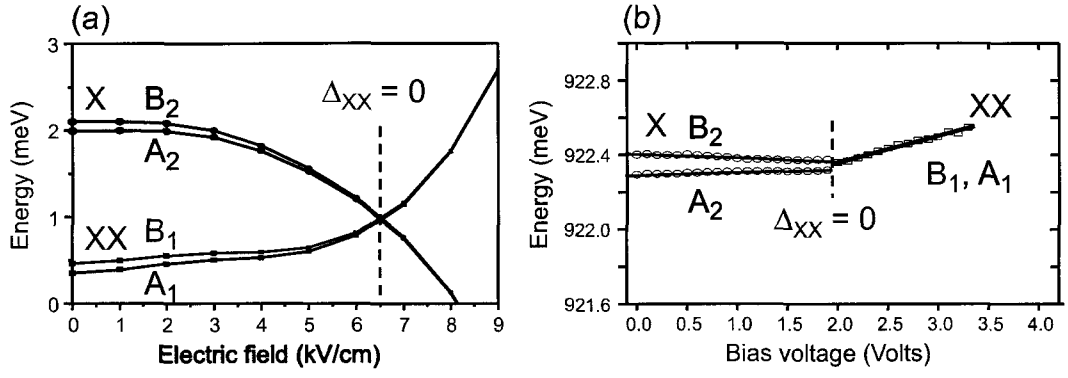

Figure 7.8: (a) Calculated PL transitions for exciton and biexciton as a function of lateral electric field obtained utilizing Fermi's Golden Rule. For a critical value of the electric field, $F = 6.5\,\mathrm{kV/cm}$, the emission energies of XX and X cross and the binding energy of XX is removed (*i.e.*, $\Delta XX = 0$). (b) Peak energies of X and XX extracted from Figure 7.7(a) as a function of bias voltage. In both (a) and (b), the transitions are colour coded in the same manner to the A_1, B_1, A_2, and B_2 transitions in Figure 7.2.

The origin of the crossing for the X and XX lines can be understood as follows. In the absence of e-h exchange, the two optically active $|\downarrow\Uparrow\rangle$ and $|\uparrow\Downarrow\rangle$ states have the same energy. Here, the single arrow denotes the spin of the electron, and the double arrow that of the hole. The e-h exchange mixes the two configurations and splits their energies. As a result, two excitonic states are obtained, $X_{1,2} = \left(|\downarrow\Uparrow\rangle \mp |\uparrow\Downarrow\rangle\right)/\sqrt{2}$, with energies

$$E_{X1,X2} = E_{00}^{e} + E_{00}^{h} - V_0^{eh} - \Delta E_X^{corr} \mp \frac{\Delta_{AES}}{\sqrt{2}}. \tag{7.4}$$

Here, $E_{00}^{e}+E_{00}^{h}$ are the single particle energies for electron and hole, V_0^{eh} is the electron-hole Coulomb attraction; ΔE_X^{corr} is the correlation energy, and Δ_{AES} is the anisotropic exchange splitting of the two intermediate exciton states. These two intermediate states in the biexciton cascade are shown schematically in Figure 7.2. Since the final state in the excitonic recombination is the vacuum, the above energies also define the PL peak positions corresponding to the transitions A_2 and B_2, respectively. As

the electrostatic field F is increased, both PL transitions of A_2 and B_2 decrease due to reduction in single particle energies (*i.e.*, Stark shift). The redshift is small due to compensation of Stark shift with applied lateral electric field, discussed in detail in Chapter 5 and 6. To briefly summarize, the e-h term V_0^{eh} and the correlation energy ΔE_X^{corr} also decrease and since they appear with negative sign, changes in the single-particle energies are compensated.

Similarly for the biexciton, the energy can be written approximately as

$$E_{XX} = 2E_{00}^{e} + 2E_{00}^{h} + V_0^{ee} + V_0^{hh} - 4V_0^{eh} - \Delta E_{XX}^{corr}, \tag{7.5}$$

with the e-e and h-h Coulomb terms accounting for the repulsion between carriers of the same type. The energies of photons emitted in transitions A_1 and B_1 correspond to the differences between this energy and those of the two single excitons. They are

$$\begin{aligned} E_{A1,B1} &= \left[E_{00}^{e} + E_{00}^{h} - V_0^{eh} - \Delta E_X^{corr} \pm \frac{\Delta_{AES}}{\sqrt{2}}\right] \\ &\quad + \left[V_0^{ee} + V_0^{hh} - 2V_0^{eh}\right] \\ &\quad - \left[E_{xx}^{corr} - 2\Delta E_x^{corr}\right]. \end{aligned} \tag{7.6}$$

In this expression, the first term is identical to the PL peak positions of the single excitons, only with opposite contribution from the AES. The field dependence of single excitons was determined to be almost insensitive to the field because of competing single particle and electron-hole Coulomb terms. Note that although the energy of the biexciton is not renormalized by the AES, the energies of the final states, *i.e.*, the excitons, are renormalized and this splitting will therefore appear in the biexciton PL spectrum with reversed polarization (see Figure 7.6). The second term accounts for the Coulomb interactions between the two electron-hole pairs building the biexciton. At zero electric field, this term is approximately zero since the repulsion between

carriers of the same type is balanced by electron-hole attraction so that the third term, comparing the correlation corrections of the biexciton to those of the exciton, defines the splitting between the PL lines of the two complexes. This third term is usually negative resulting in biexcitonic PL peaks that appear at lower energies than those of single excitons. The field induced separation of electron and holes decreases the electron-hole attraction driving the biexciton PL peak positions towards higher energies. For a sufficiently large electric field the interaction terms exactly cancel the correlation corrections, resulting in a degeneracy of the biexciton and exciton emission. Here, the redshifting exciton and blueshifting biexciton result in the removal of biexciton binding energy at a field of 6.5 kV/cm. At this point the two decay paths, A and B, become indistinguishable and entangled photon pairs are created.

7.5 Control of biexciton binding energy via ridge nanotemplate

Up to now, experimental investigations of biexciton binding energy, Δ_{XX}, on dot size have been performed on randomly located quantum dots [89–91,114–116]. In the work presented here, I study for the first time the dependence of Δ_{XX} on dot size using a scalable device architecture desirable for applications in quantum cryptography such as generation of single photon and entangled photon pairs. These results also investigate a new regime for the dependence of Δ_{XX} on dot size in larger InAs/InP quantum dots that emit near the telecommunications wavelength of 1.55 μm. The binding energy of the XX is found to be directly controlled by the base width dimensions of the ridge nanotemplate. Here, Δ_{XX} can be controllably tuned from the binding (bound) to antibinding (unbound) regime and through zero – a regime not previously studied

in large dots. The results suggest that the mechanism responsible to reach the antibinding regime for the XX in large quantum dots are piezoelectric fields [114, 116]. Piezoelectric fields in large quantum dots tend to separate electrons and holes, thus leading to an unbound XX state. The separation of charges required to produce an unbound XX is also expected to reduce the fine structure splitting since this splitting depends strongly on overlap of electron and hole wavefunctions [26, 64]. Indeed, in the large quantum dots presented here, no fine-structure splitting was observed within the spectral resolution of $50\,\mu$eV, consistent with the work by N. Chauvin and co-workers with spectral resolution of $100\,\mu$eV [116]. Thus, enhanced piezoelectric fields in large quantum dots leading to an unbound XX are also expected to strongly reduce the fine-structure splitting, possibly even near zero – a key requirement for entangled photon pair generation utilizing semiconductor quantum dots (see Section 7.1 and 7.2). Over half of site-selected dots shown here exhibit unbound biexcitons with observed fine-structure splittings less than the spectral resolution, thus promising arrays of entangled photon pairs to be generated within this scalable architecture (*i.e.*, if fine-structure splitting is smaller than the homogeneous linewidth of exciton). An added benefit to the expected reduction in AES with piezoelectric fields in larger dots is the strong dependence of exchange energy, which decreases for increasing dot size [116, 121]. In general, the AES splitting is smaller than the exchange energy (splitting between dark and bright exciton states) [64], which therefore also contributes to the reduced fine structure splitting for site-selected dots exhibiting an unbound XX state.

7.5.1 Summary of previous work

In the past 3-5 years, many single quantum dot experiments have been conducted, which study the dependence of Δ_{XX} on the dot size [89–91,114–116]. In those optical studies of the exciton-biexciton system [89–91,114–116], the size of the quantum dots is parameterized by the exciton ground state energy since the exciton emission energy shifts to higher energy due to decreasing dot size. The decreasing dot size corresponds to dot height as in randomly located quantum dots, the lateral size and shape varies depending on the growth conditions [91].

For a nice summary of various reports for dependence of biexciton binding energy on dot size, see the work of C. Dal Savio *et al.* [91]. In that work they studied InAs/InGaAs quantum dots emitting in the spectral range of 1.14 eV to 1.2 eV and compared to previous reports mainly on InAs quantum dots embedded in an GaAs matrix (*i.e.*, InAs/GaAs), which emit at shorter wavelengths in the spectral range of 1.2 eV to 1.4 eV [89,114,115]. C. Dal Savio and co-workers concluded that there are two regimes for Δ_{XX} dependence on dot size [91]. One regime consists of small dots, in which Δ_{XX} decreases with decreasing dot size. In this regime, Δ_{XX} makes a transition from bound to unbound and for certain dot dimensions even $\Delta_{XX} = 0$ is obtained. This observed dependence of Δ_{XX} on dot size is attributed to decreasing correlations resulting from stronger confinement (increased energy level spacing) and reduced number of bound states for a finite barrier potential in small dots. Both the stronger confinement and reduced number of bound states in smaller dots contribute to a weaker interaction of the ground state mixing with excited states (*i.e.*, correlation). In addition, the stronger confinement potential in smaller dots generates a repulsive effect of the Coulomb interaction from carriers of the same type, thus leading to an

unbound ('anti-binding') biexciton state. The other regime is for large dots. Here, the dependence of Δ_{XX} on dot size is opposite to that of small dots. In these studies, they concluded that further measurements were required to predict the behaviour for larger dots [91]. It was suggested that a transition from binding (bound) to antibinding (unbound) may also take place for larger dots under the influence of piezoelectric fields [114, 117]. Note that the transition from a bound to unbound XX in smaller dots is due to a different mechanism. In small dots, the hole ground state is much more strongly localized than the electron ground state [114]. Thus, it is still possible to have an AES since there is considerable overlap of electron and hole wavefunctions. In contrast, in very large dots the hole wavefunction is strongly elongated due to the large piezoelectric field with a density minimum in the centre of the dot while the electron ground state is less sensitive to the piezoelectric potential due to the smaller electron mass [114]. Here, the AES is expected to be strongly reduced and possibly even near zero since there is a weak overlap between electron and hole wavefunctions [26, 64].

More recently, InAs/InP quantum dots have been studied by N. Chauvin and co-workers [116], which allowed them to study longer wavelengths in the exciton emission energy range of 0.9 eV to 1.05 eV. There, they mapped out the dependence of Δ_{XX} on dot size and confirmed results obtained by C. Dal Savio *et al.* [91] for larger dots. In their work, Δ_{XX} was reduced further in larger dots from 3.4 meV at 1.05 eV to 0.4 meV at 0.9 eV. The reduction in biexciton binding energy is attributed to increase in piezoelectric fields in large dots. Piezoelectric fields tend to separate charges, which leads to an unbound XX state [114]; however, the antibinding regime has not been achieved yet in large quantum dots until this work. The antibinding regime for XX in

large dots may be a very important step towards the realization of a scalable route for the generation of entangled photon pairs. As discussed previously, the piezoelectric field that causes a separation of charges leading to an antibinding XX state is also expected to reduce the fine-structure splitting since this splitting depends strongly on the electron-hole wavefunction overlap [26,64]. Indeed, in the work of N. Chauvin and co-workers, no fine-structure was observed within the spectral resolution of $100\,\mu$eV for large dots.

7.5.2 Ridge nanotemplate

The dependence of Δ_{XX} on dot size for 19 individual InAs/InP quantum dots in ridge nanotemplates is shown in Figure 7.9(a). In the data range for exciton (X) emission similar to N. Chauvin *et al.* [116], the dependence of Δ_{XX} on X emission energy is remarkably similar. In addition, however, for decreasing X emission energy, there is a transition from the bound to unbound XX regime. The tuning range controlled via the ridge nanotemplate is rather large: $\Delta_{XX} = +3.1$ meV at X emission energy of 1011 meV while $\Delta_{XX} \simeq -4$ meV near the telecommunications wavelength of $1.55\,\mu$m (800 meV). This corresponds to a controlled tuning range for Δ_{XX} of 7.1 meV. The observed crossover point for zero XX binding energy (*i.e.*, $\Delta_{XX} = 0$) occurs in the energy range between $\sim 910 - 930$ meV. The resulting dependence of Δ_{XX} on dot size is attributed to increase in piezoelectric fields with increasing dot size [114, 116].

As described in more detail in Chapter 3, the base width of the nanotemplate controls the dot size and therefore the exciton emission energy. For larger base widths (Figure 7.9(c)), the dot height is smaller and therefore emits at higher energy. As the starting base width is reduced (Figure 7.9(b)), the same amount of dot material corresponds to an increase in dot height and redshift of the exciton energies. The

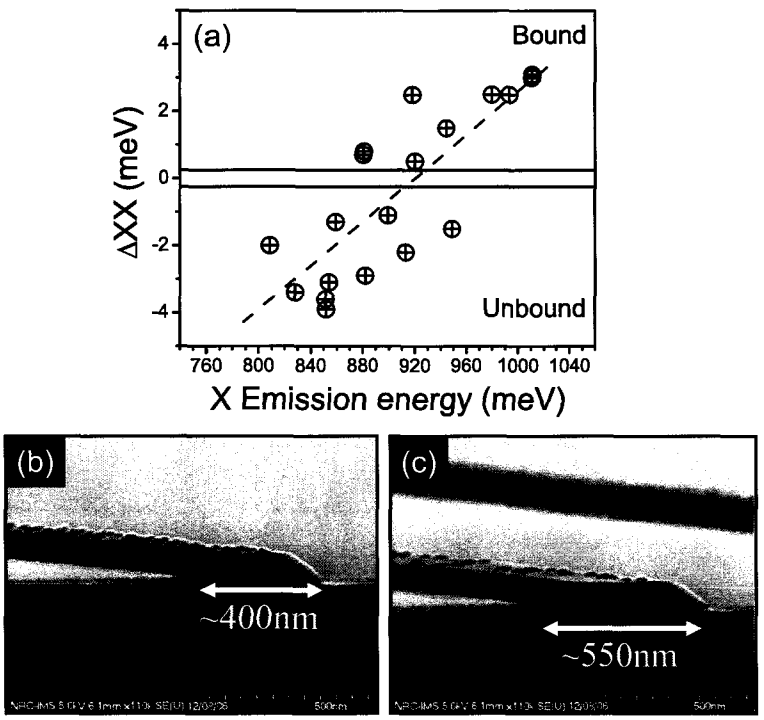

Figure 7.9: (a) Controlled tunability of biexciton binding energy, Δ_{XX}, on dot size for ridge nanotemplate. SEM images of ridge nanotemplates with starting basewidth of (b) 400 nm and (c) 550 nm. Decreasing the ridge base width increases the dot height for the same amount of dot material deposited and shifts the the excition emission energy towards the telecommunications band around 1.55 μm (800 meV).

redshift of the exciton energies for increasing dot height (decreasing ridge width) is observed in Figure 7.9(a). The differences in dot height for two different ridge nanotemplates can be observed in the SEM images of Figure 7.9(b) and 7.9(c).

There is considerable scatter of the observed Δ_{XX} for a given exciton emission energy. It is likely due to variations in the lateral dot dimensions for a given quantum dot height. At different dot dimensions, this leads to a different strain distribution inside the dot, thus leading to different piezoelectric fields which directly influences Δ_{XX} [114, 117]. The dotted line in Figure 7.9(a) shows a linear fit to the data and has a gradient of 0.03 ± 0.01.

The controlled tunability of Δ_{XX} via the ridge nanotemplate presented here is desirable for the realization of a scalable route to producing entangled photon pair sources. Such a scheme is possible providing piezoelectric fields in large quantum dots is sufficient to reduce the fine structure splitting near zero as the results suggest, when compared to model calculations. The optical signature of piezoelectric fields in large quantum dots is the observation of an unbound XX. In the InAs/InP site-selected dots studied here, the unbound XX regime is found to be controlled via the growth conditions of the ridge nanotemplate making it possible to produce arrays of entangled photon pairs near the telecommunications band around 1.55 μm.

7.6 Conclusion

Photoluminescence data of exciton and biexciton subject to an applied lateral electric field have been presented for a single, deterministically positioned InAs/InP quantum dot on ridge nanotemplate. These results suggest a mechanism for the production of entangled photon pairs in quantum dots that does not require removal of the anisotropic electron-hole exchange splitting – a requirement the scientific community has been struggling to overcome. Instead, entangled pair generation can be affected through the electrical tuning of individual quantum dots such that the biexciton binding energy is removed at finite field. The observed crossing of the exciton and biexciton (*i.e.*, $\Delta_{XX} = 0$) is accomplished in experiment by precisely balancing the Coulomb repulsions and attractions of the exciton and biexciton via an in-plane electric field and is found to be in excellent qualitative agreement with many-body configuration interaction calculations of the multi-exciton emission process.

Additionally, an alternate scheme for the generation of entangled photon pairs,

that does not require electric field tuning, was investigated. The biexciton binding energy of individual InAs/InP quantum dots was determined to be controlled via the ridge nanotemplate. Here, the biexciton binding energy was found to decrease with increasing dot size (decreasing ridge base width). The results demonstrated a large tuning range of the biexciton binding energy of 7.1 meV. A new regime of the biexciton binding energy was obtained in large quantum dots, the unbound biexciton regime. Comparison to model calculations revealed that piezoelectric fields are responsible for separation of charges leading to an unbound biexciton state. Finally, fine structure splittings within the spectral resolution were not observed for unbound biexcitons in these large dots suggesting that piezoelectric fields are also expected to strongly reduce the fine-structure splitting near zero. Such a scheme, if successful is a significant improvement over all existing proposals for generation of entangled photon pairs around the telecommunications band of 1.55 μm.

The techniques presented in this chapter promise the practical realization of arrays of quantum dot based entangled pair sources using site-selected quantum dots emitting at wavelengths suitable for fibre based quantum cryptography, without resort to large external magnetic fields, or materials engineering of individual dots.

Chapter 8

Single electron charging and entangled photon generation in the same quantum dot

Thus far, this thesis has presented optical and electronic properties of a single quantum dot in a lateral electric field. The highlight of this research is the possibility to generate entangled photon pairs in a scalable device architecture through removal of the biexciton binding energy. The device studied in this chapter advances scalability further since arrays of gated, single quantum dots can be fabricated without the need of post-processing to isolate a single dot. In addition to applying an in-plane electric field across the quantum dot as demonstrated previously, an electric field can also be applied along the growth direction (vertical electric field). Application of a vertical electric field adds functionality to the device through precise control of the electron number. By tuning the electric field, a single electron can be isolated – an effort that is achieved and demonstrated in this chapter in a scalable device architecture desirable for quantum information applications.

Recent advances in coherent control of the spin states of a single electron, split by a static magnetic field which is confined in a semiconductor quantum dot, makes such

structures an ideal choice for the optical qubit [122]. A quantum bit (qubit) is the basic logical unit of information within a quantum computer [123]. In contrast to bits in a classical computer, where each bit can only exist as a logical 0 or 1, the quantum bit can exist as a coherent superposition of both states. To be useful for quantum information processing, full quantum control of the qubit is necessary, such that the quantum state can be initialized in a well-defined state, coherently manipulated and then read out with high fidelity before the quantum information is lost due to decoherence [122]. Additionally, the atomic-like electronic structure of such quantum dots is expected to suppress coupling of the spin to the solid-state environment, thus protecting the quantum information against decoherence and extending storage times to the millisecond time-scale, allowing many spin manipulations to be performed [124].

Full quantum control of the electron spin is already well established in "top-gate" defined quantum dots [125–127]. However, to make the long distance transfer of quantum information a possibility, an optical qubit is desirable. In self-assembled quantum dots, both electrons and holes are confined and the dots are therefore optically active allowing the spin state of the carriers to be easily converted into the polarization state of a single photon [23]. Demonstration of all quantum optical control of the electron spin in self-assembled quantum dots has been achieved allowing the spin to be initialized in a well-defined orientation [124], manipulated coherently on the picosecond timescale [14] and read out with non-destructive optical techniques on the nanosecond timescale [13]. More recently, all optical quantum control of the electron spin has been achieved on the picosecond timescale within a single system, thus increasing the number of operations possible before the electron spin information is lost due to decoherence [15]. Additionally, due to the sensitive techniques required to measure

the single spin optically, such as direct absorption [128] or time resolved Faraday [12] and Kerr [11] rotations, the very weak signals involved limit the time available for spin manipulation to $\sim$ 1 microsecond or even a few nanoseconds [129]. More advanced readout schemes have been proposed that utilize non-perturbative, time gated photoluminescence measurement of the charge state, which extends storage times into the millisecond range. Converting the spin information of the resident electron into charge, which can then be measured non-perturbatively by photoluminescence, allows spin manipulation and investigations of spin relaxation and decoherence mechanisms over the longer time scales that are described by theory [129].

Although coherent quantum optical control has also been demonstrated for isolated nitrogen-vacancy defect centres in diamond [130] at room temperature, they cannot at present be controllably positioned in a scalable device architecture. The ability to position dots, as demonstrated in this thesis, is advantageous for producing arrays of quantum dots making them potentially more scalable. To date, demonstrations of qubit coherent control and manipulation of the electron spin have been performed on randomly nucleated self-assembled quantum dots [11–15]. Such quantum dots can be embedded within the intrinsic region of an n-i Schottky diode, where the number of electrons can be precisely controlled [2–10] and the spin manipulation required for quantum information processing can be performed. To bring such experiments closer to large scale implementation, one must find routine ways to control the nucleation site of individual dots and embed them within active devices as required. The necessary control can be achieved using nanotemplate deposition techniques where the nucleation site of individual InAs/InP dots can be precisely controlled [29, 30] and electrostatic gates or photonic crystals constructed around them [8].

In the work presented here, a single, deterministically positioned, InAs/InP quantum dot is electrically contacted allowing direct control of the number of electrons within the dot using a vertical electric field. Single electron charging is monitored through the photoluminescence signal from the dot as a function of the vertical electric field. By measuring the induced Stark shift of the excitonic transitions, I show that the zero electric field quantum dot dipole is in the opposite direction to that of InAs/GaAs quantum dots suggesting that the electron is localized above the hole. The strength of the measured dipole is supported by a model in which the Indium composition is uniform throughout the dot, a result that is consistent with independent studies of conventionally grown InAs/InP quantum dots [8, 131, 132].

On the same quantum dot, by using four gates precisely positioned around the periphery of the quantum dot, it is possible to apply a lateral electric field in the plane of the quantum dot. Of particular significance is that the exciton and biexciton are both observed as a function of lateral field and the binding energy of the biexciton is tuned over a large energy range. Removal of the biexciton binding energy was found in the previous chapter to be important for the generation of entangled photon pairs. Comparison to theoretical calculations reveal the underlying confinement potential for single dots on pyramid nanotemplates are square-like. In comparison to dots on ridges, which exhibit an in-plane parabolic confinement potential, the physics of gated dots on pyramidal templates is similar – the biexciton and exciton transitions are expected to cross at finite field thus resulting in removal of the biexciton binding energy.

To understand the charging mechanism presented in this chapter, two-dimensional calculations are presented aimed at controlling the electron number in individual

quantum dots via vertical electric fields since the InP nanotemplate device geometry is pyramidal and not planar as in the literature and should be taken into consideration. In order to obtain single electron charging and entangled photon pair generation on the same quantum dot, three-dimensional Nextnano calculations are presented in order to determine the applied biases required on each of the four top Schottky gates around the periphery of the single quantum dot. Solutions of the three-dimensional Poisson equation in Nextnano show that it is possible to apply an in-plane electric field in any crystal orientation – an important step in next generation devices for entangled photon pair generation. The Nextnano calculations also show the effect of the applied electric field due to a dot misalignment if the four top Schottky gates are not aligned perfectly with respect to the single dot – a common situation in practice since alignment is currently limited to the resolution of the e-beam writer.

This chapter is organized as follows: Section 8.1 introduces the deterministically positioned, gated, single InAs quantum dot on InP nanotemplate that is used in the single electron charging and in-plane electric field experiments. In Section 8.2, two-dimensional calculations are presented to understand the current charging mechanism in the positioned quantum dots. In Section 8.3, three-dimensional calculations in Nextnano are presented that show that it is possible to apply an in-plane electric field in any crystal orientation. These calculations also show that it is possible to obtain single electron charging in metal-oxide-semiconductor devices and that the effect on the conduction band edge is larger than that of metal-semiconductor devices. The single electron charging experiments for a single gated InAs quantum dot on InP nanotemplate are shown in 8.4. In Section 8.5, results of combined vertical and lateral electric field measurements are presented, which exhibit a large tuning range of the

biexciton binding energy by more than 1.5 meV. The in-plane lateral electric field dependence suggests a square-like confining potential in the plane of the quantum dot when compared with model calculations. This is in contrast to the parabolic potential presented earlier for single dots on ridges. Finally, in Section 8.6, the main conclusions are summarized.

8.1 Device

An SEM micrograph of a typical device used for the single electron charging experiments in a deterministically positioned quantum dot (Section 8.4) is shown in Figure 8.1(a) along with a schematic cross section of the device in Figure 8.1(b), depicting the positioned single InAs quantum dot. The structure consists of four metallic Schottky gates positioned around the pyramidal InP nanotemplate used to control the quantum dot nucleation site. These four gates can be used to apply an electric field within the plane of the quantum dot [26] or in conjunction with an ohmic back contact, to apply a vertical electric field along the growth direction. Details of the directed self-assembly technique used to control quantum dot nucleation are presented in Chapter 3. Typical photoluminescence (PL) from such a dot is shown in Figure 8.1(c), in which only a single emission peak is observed over a wide energy range ($\sim$400 meV) – a clear signature of reaching the single dot regime on the nanotemplate (see Chapter 3).

Device construction is a three-step process: In the first step, an oxide covered, (001)-oriented, sulphur doped, n-type InP wafer is patterned with e-beam lithography to produce square openings, with edges aligned along the [110] crystallographic directions, that expose the underlying InP substrate. Chemical beam epitaxy (CBE)

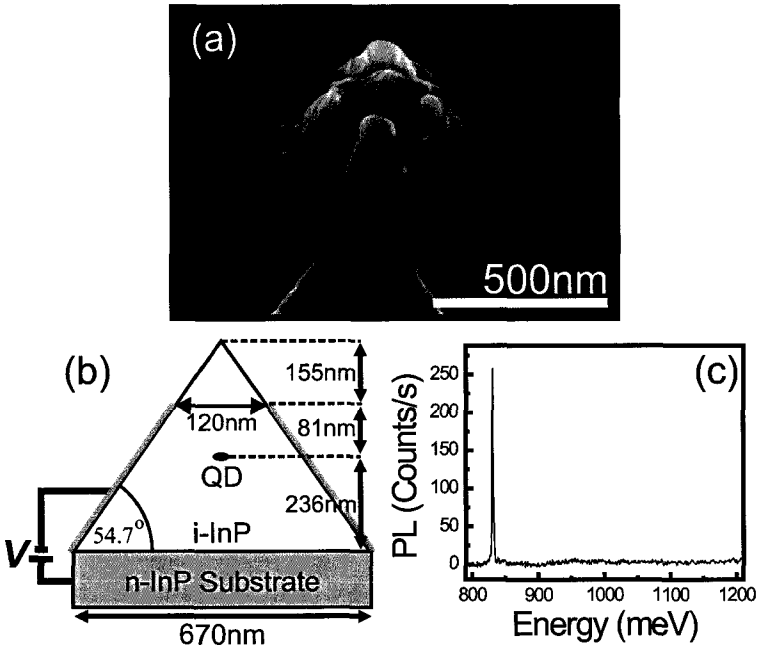

Figure 8.1: (a) SEM micrograph of four Schottky metallic gates precisely positioned around a buried individual InAs quantum dot in an InP pyramidal nanotemplate. (b) Schematic view of device indicating a single InAs quantum dot embedded in the intrinsic region (InP) of an n-i Schottky diode. A 20 nm layer of SiO_2 is used between the top Schottky gates and n-doped InP substrate to minimize leakage current. (c) Typical single-dot photoluminescence from device structure shown in (a) which emits around 830 meV (1500 nm).

of InP on such patterned wafers produces growth only on the exposed areas of substrate. Undoped InP pyramids with {110} side-facets are produced; designed such that the (001) apex is wide enough to support only a single dot (see Chapter 3). A single InAs quantum dot is then grown on this apex before being capped with InP and removed from the growth system for Schottky diode processing. If the InP cap is grown sufficiently thick, the overgrowth rotates the pyramid to produce {111} sidewalls instead of the initial {110} sidewalls. The top Schottky gates (20 nm Ti/80 nm Au), defined by e-beam lithography and liftoff, are precisely positioned with respect to the dot and lie on the {111} sidewalls of the nanotemplate. An ohmic contact

is made to the back surface of the n-type substrate to facilitate the application of a vertical electric field. Note that a contacted pyramid containing the initial {110} sidewalls are also possible, although the electric field in this device is slightly larger due to the modified device dimensions (see Section 8.3).

Utilizing the known device dimensions (shown in Figure 3) and background doping within the intrinsic region of the nanotemplate ($10^{16}\,\mathrm{cm}^{-3}$), the vertical electric field, F, at the position of the dot as a function of top gate bias voltage, V_G, is calculated as (Section 8.2)

$$F[kV/cm] = 15.5V_G + 11.1. \tag{8.1}$$

Here, $V_G > 0$ for reverse bias. The details of the model used to calibrate the electric field can be found in the following section.

8.2 Electrostatic modeling of gated pyramids

Quantum dot charging of an individual quantum dot embedded in a gated pyramidal nanotemplate (structure from Figure 8.1(a)) was studied using a commercial device simulation software (ATLAS, Silvaco International), which simultaneously solves Poisson's equation and the continuity equations for electrons and holes while utilizing the drift diffusion model for charge transport. Firstly, the structure is defined including the substrate (50 nm n-doped InP), metallic gates and buried quantum dot on a finite difference grid with resolution of 1 nm. Secondly, the pyramidal nanotemplate is modeled as a cone in cylindrical coordinates in order to approximate the pyramidal geometry in three-dimensions. The dimensions of the pyramid are chosen to be representative of the present nanotemplates studied, where the basewidth, w, is 500 nm and the height of the pyramid is $\frac{1}{2}w$. Thirdly, to represent the InAs quantum dots

attractive potential, the quantum dot is modeled as an acceptor trap with energy 150 meV below the conduction band and is defined to be full when a single electron is loaded into the trap. To obtain the electron density, N_T, for a single electron, the volume, V, of the quantum dot is multiplied by the electron density and set equal to one ($VN_T = 1$), which corresponds to the single electron. Lastly, the quantum dot dimensions are chosen to be comparable to the experimentally investigated dots with a height of 5 nm and width of 30 nm.

A 2D cross-section of the pyramidal nanotemplate model with a vertical cut through the centre of the cone is shown in Figure 8.2(a). The structure consists of an n-i structure with a single quantum dot (trap) embedded in the intrinsic region of the InP pyramid ($\sim$ 125 nm from the pyramid apex). The background doping of the intrinsic region is $10^{12}\,\mathrm{cm}^{-3}$. An aluminum top Schottky gate and back contact gate is present in order to apply axial electric fields, which allows the direct control of dot occupancy. The contour plot in Figure 8.2(a) demonstrates the modification of the local potential in the region of the dot due to the top Schottky gate when the gates are at 0 V. Without the top gate, the potential in the pyramid would be uniform and the dot occupancy would be full since the electrons from the n-doped region would drift towards the trap.

To understand the mechanism of obtaining direct control of the dot occupancy, the energy band diagram for the device configuration along the Y-Cut from Figure 8.2(a) is depicted in Figure 8.2(b), as well as the potential. At 0 V bias, the energy and location of the dot can be observed along the conduction band energy curve at a distance of 125 nm from the apex of the pyramid. The height of the quantum dots attractive potential is 150 meV below the conduction band to represent the depth of

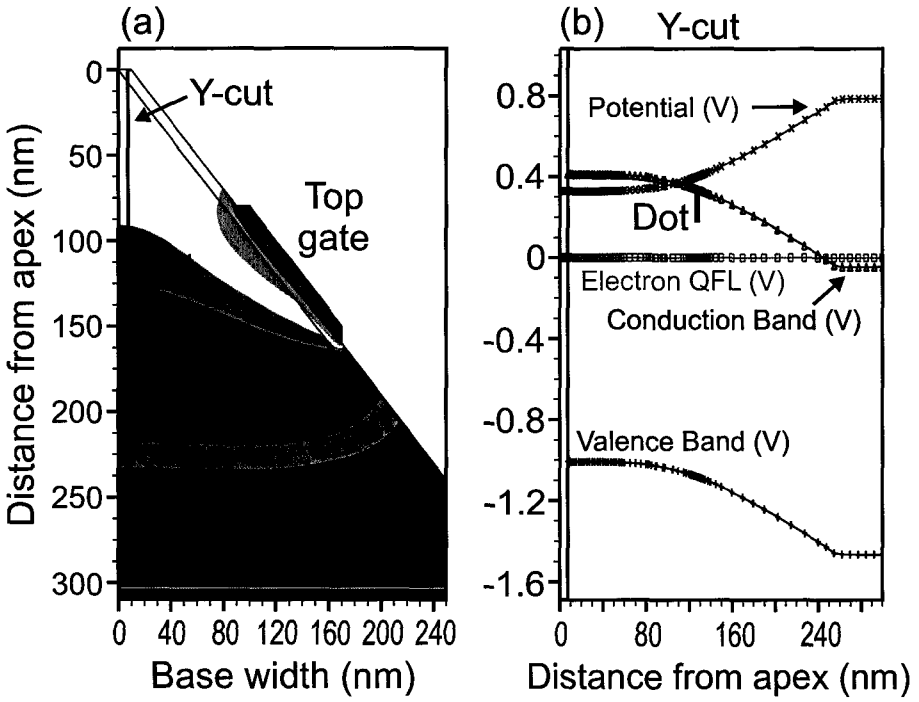

Figure 8.2: (a) 2D cross-section of pyramidal nanotemplate model in ATLAS. Only half of a triangle is required to model the pyramid as a cone in cylindrical coordinates. Each color change in the contour plot signifies a potential difference of 0.05 V, where the potential increases as the vertical cut through the dot varies from the pyramid apex to the base of the pyramid.(b) Energy band diagram of the device, as well as the potential along the Y-cut through the device in (a).

the trap. The dot is empty at 0 V bias since the energy level of the quantum dot (trap) is above that of the electron quasi Fermi level (QFL). By forward biasing the device, the energy level of the quantum dot crosses that of the QFL, thus filling the dot with a single electron. To empty the dot again, the bias is reversed until the energy level of the quantum dot is above the electron QFL. Note that the mechanism required to fill the dot is not the strength of the electric field, but the ability to manipulate the electron QFL with respect to the quantum dot energy levels (*i.e.*, band bending of conduction band). The strength of the electric field is relevant for the discussion on

the excitonic dipole in Section 8.4.1.

By changing the position of the quantum dot or position and length of the top Schottky gate, the switching voltage required to load or empty a single electron (depends on bias direction) can be modified from 0.7 V reverse bias to 0.4 V forward bias. Additionally, the voltage regime required to empty the dot of excess electrons shifts to larger reverse biases for higher background doping than $10^{12}\,\mathrm{cm}^{-3}$. For example, in conventionally grown InAs/InP quantum dots on planar substrates with a background doping in the intrinsic region of $10^{12}\,\mathrm{cm}^{-3}$, a forward bias of $\leq 0.2\,\mathrm{V}$ is required to empty the dot. Increasing the background concentration of the intrinsic region shifts the switching voltage required to empty the dot to reverse biases due to electric field screening [8]. In the low bias regime, the effect of the field widens the depletion region from the top Schottky gate to the position of the dot and the bias voltage has minimal effect on the electric field at the location of the dot. With increasing reverse bias, the depletion region widens past the location of the dot. Once the quantum dot is in the depletion region once again, the electric field is approximately linear with gate voltage. The bias voltage required to empty the dot (1.4 V reverse bias) was well produced within the present model when modifying the device dimensions to reproduce the planar geometry and assuming a background concentration in the intrinsic region of $5\times10^{16}\,\mathrm{cm}^{-3}$, which is in excellent agrement for the measured background doping as measured using secondary ion mass spectrometry [8].

8.3 Electric field in any crystal orientation – 3D model

The four gates precisely positioned around the periphery of the pyramidal nanotemplate can also be used to apply a lateral electric field in the plane of the quantum dot in any crystal orientation (Figure 8.3(a)). Such a capability may be advantageous for the generation of entangled photon pairs (see Chapter 7). The gated pyramid described here provides infinite degrees of freedom compared to two terminal devices presented in Chapter 6 since applied fields can be oriented in any crystal direction. This is in strong contrast to two terminal devices since the electric field can only manipulate one axis of the crystal in the plane of the quantum dot. The added benefit of the four terminal device presented here is that the ohmic back gate can be used in conjunction with the top gates to control the charge state of the device, desirable for device applications.

To understand the applied electric field in the gated pyramid utilizing all 5 gates (4 top gates, one global back gate), three-dimensional calculations were conducted in Nextnano3, a commercial software developed by the Walter Schottky Institute in Garching, Germany. Since the software is presently in the development stage, Nextnano3 was unable to model devices with Schottky contacts since two different materials come in contact with the same gate material – a situation that is not allowed in Nextnano3 (*i.e.*, semiconductor and air). To overcome this limitation, a cap oxide is introduced which circumvents this problem. Additionally, due to the large computational effort required in Nextnano3 for three dimensions, the gated pyramid modeled here is smaller than the experimentally investigated ones. The current model uses dimensions of the gated pyramid with a base width of 300 nm and height of

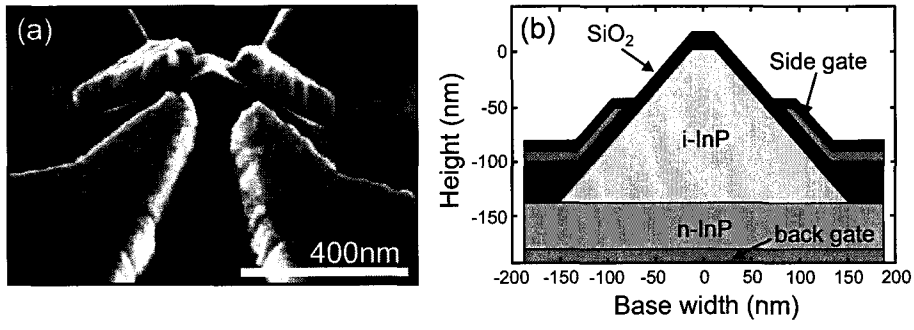

Figure 8.3: Device structure to be modeled in three dimensions by Nextnano3. (a) SEM micrograph of pyramidal nanotemplate with four gates precisely positioned around the buried quantum dot. There is a back ohmic contact to facilitate the application of vertical field (b) 2D cross-section of gated pyramid. The base width of the pyramid is 300 nm. Two side-gates are evident in the 2D cross-section. The other two side-gates are also used as input in the Nextnano3 model (not shown here). Since the model is 3D, the width of the gate at the base of the pyramid is 160 nm and tapers down to 60 nm at the tip of the gate. The cap oxide is introduced as an artifact as two materials are not allowed to surround the side-gate in three-dimensional Nextnano3 calculations.

150 nm, which is approximately 40-60 % smaller than the experimentally investigated ones. Thus, the results presented here only provide a qualitative picture of the applied electric field in the pyramid and are not representative of the applied voltages required in experiment to obtain the same electric field strength. Nevertheless, the physics is the same and the model presented is crucial in understanding the applied voltages required on each gate in experiment for a true lateral field. Of particular importance is that the vertical electric field is not modified while applying an in-plane electric field since this would change the charge state of the dot; an undesirable result. I show here that for appropriate choice of the applied voltages on each gate, the vertical field is constant at the centre of the dot if precisely positioned in the middle of the four top gates and that the electric field can be applied in any in-plane crystal direction. If there is a slight misalignment of the gates around the periphery of the dot, then

the electric field is modified resulting in a built-in lateral field when the four top gates are held at the same potential similar to experimental investigation. Experimental optical data for an in-plane electric field in a gated pyramid device is presented in Section 8.5.

A 2D cross-section of the 3D gated pyramid model is shown in Figure 8.3(b). Here, two of the four side metallic gates can be viewed. The other two side gates are also used as input in the Nextnano3 model, although not shown here. By rotating the 2D cross-section 90° about the growth axis, it is possible to view the other two side gates. The 2D cross-section of this 90° rotation would be identical to the one presented in Figure 8.3(b). Since the model is 3D, the width of the gate at the base of the pyramid is 160 nm and tapers down to 60 nm at the tip of the gate. The height of the gates used here are 50 nm. Other important parameters used within this model are: thickness of oxide, $t_{ox} = 20\,\text{nm}$; background doping in intrinsic InP region of $1 \times 10^{16}\,\text{cm}^{-3}$ and; doping concentration of n-doped InP region is $5 \times 10^{18}\,\text{cm}^{-3}$.

8.3.1 Vertical field – Growth direction

Results of the calculation for biasing all four top gates at the same negative potential are shown in Figure 8.4(a). At low negative gate potentials, the intrinsic region (i-InP) of the InP is not depleted and the bias voltage has little effect on the conduction band edge of InP. At a critical bias voltage of approximately $V_g = -0.1\,\text{V}$, the InP pyramid is depleted of electrons and the gate voltage has a greater effect on the conduction band edge. Depending on the location of the dot in the gated InP pyramid, the effect of the gate voltage on the dot potential significantly varies as evident in Figure 8.4(a). At a location of 30 nm from the pyramid apex ($z = 30\,nm$), the conduction band edge of InP varies linearly according to $\sim 0.6\,\text{eV/V}$ after the InP pyramid is

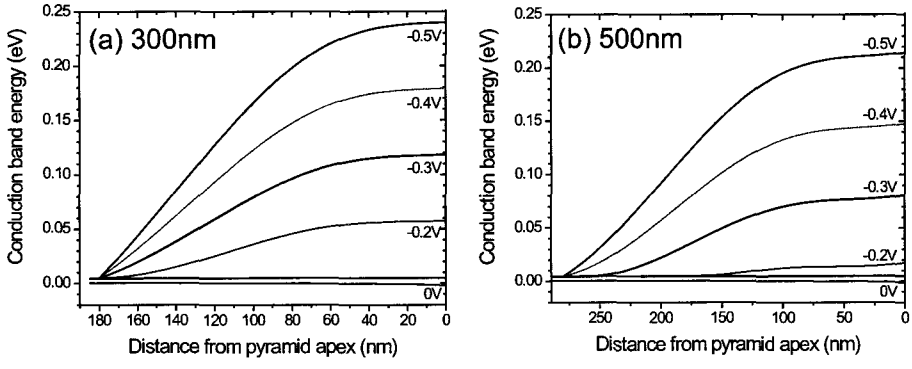

Figure 8.4: Effect of top gate voltages on gated InP pyramid with base width of (a) 300 nm and (b) 500 nm. The effect of the gate potential on the dot potential is highly dependent on the dot position in the gated pyramid. In these simulation results, all four gates are held at the same negative potential.

depleted. Thus, electron charging is also possible in the metal-oxide-semiconductor device presented here since the quantum dot's ground state is typically $\sim$ 100 meV below the band edge of InP in InAs/InP quantum dots – a result that depends highly on the dot size [61]. The energy level of the *s*-shell in the quantum dot can therefore be tuned above and below the electron Fermi level (0 eV in Figure 8.4) corresponding to an empty and charged dot, respectively.

Similar calculations were conducted on a larger pyramid size with base width of 500 nm and height of 240 nm (Figure 8.4(b)) – a pyramid size similar to the experimentally investigated ones. In comparison to the 300 nm pyramid, the effect of the gate voltage on dot potential is similar – a rather counterintuitive result. In the 500 nm pyramid, the variation of the conduction band edge with gate voltage after the InP pyramid is depleted is $\sim$ 0.66 eV/V. The main differences between the two pyramid sizes is the strength of the electric field and critical voltage required to deplete the pyramid. The further the gate is from the dot, the smaller the electric field strength as deduced by the slope of conduction band energy in Figure 8.4 ($\sim$ factor

of 2 smaller for the 500 nm pyramid compared to the 300 nm one). This is equivalent to differentiating the dot potential to obtain the electric field strength. Additionally, the critical voltage required to deplete the pyramid shifts to higher negative potentials in the larger 500 pyramid ($V_g = -0.18\,\mathrm{V}$) compared to the 300 nm pyramid ($V_g = -0.1\,\mathrm{V}$) at $z = 30\,nm$.

8.3.2 Lateral field – In-plane direction

To obtain a true lateral electric field in the gated pyramid device, all four top gates are first biased to the desired charge configuration by using a negative potential, V_g, with respect to the back gate which is grounded. Next, two opposite gates are biased at $V_g \pm V_L$ as shown schematically in Figure 8.5(a). Thus, the potential difference between the two opposite gates is $\Delta V = 2V_L$. Alternatively, the four top gates can be grounded ($V_g = 0$) and the back gate positively biased. In the calculations presented here, it is only possible to model the former. The results of the calculation are shown in Figure 8.5 for a distance of 30 nm below the pyramid apex and with $V_g = -0.3V$. The contour lines in Figure 8.5(a) represent equipotential surfaces at $\Delta V = 0.5\,\mathrm{V}$, with the distance between two adjacent surfaces reflecting how rapidly the potential changes. Thus, as the spacing decreases, the electric field increases corresponding to a lateral field applied in the plane of the pyramid.

To study the strength of the in-plane electric field and verify that the field is applied along the desired crystal direction, a 1D x-cut across the pyramid at a distance 30 nm below the pyramid apex is shown in Figure 8.5(b). The lateral electric field has the effect of tilting the bands in the plane of the pyramid. If the dot is placed at the centre of four gates, then the lateral field does not modify the vertical field; a desirable result for device applications. However, for a small misalignment in the dot location

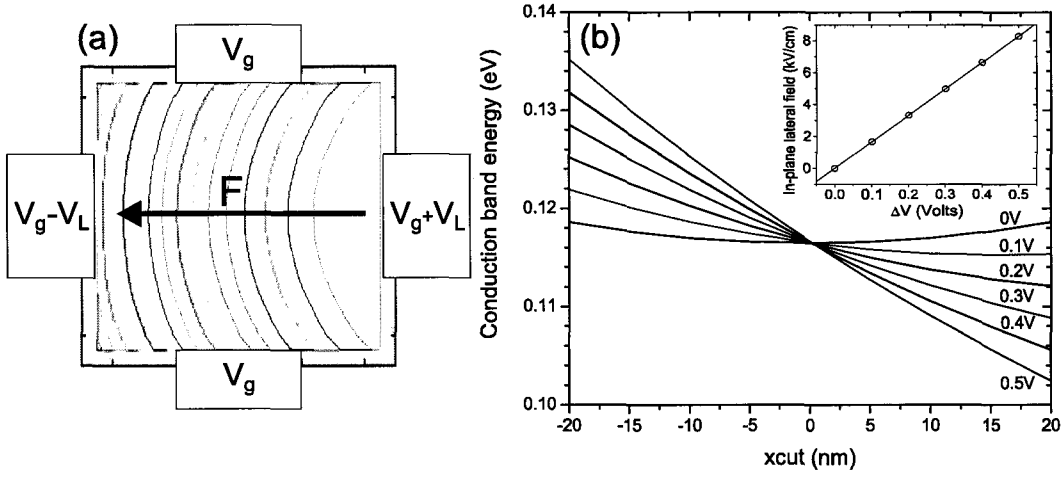

Figure 8.5: (a) Schematic top-view of gated pyramid with calculated equipotential surfaces in 2D. A lateral field is obtained by biasing two opposite gates with respect to V_g at $\pm V_L$. (b) 1D-cut across pyramid at depth of 30 nm from pyramid apex. The conduction band minimum of gated InP pyramid is shown for varying ΔV.

from the centre results in the vertical electric field being modified, corresponding to a different gate voltage, V_g, required for device operation (*i.e.*, to control the number of electrons). The effect of dot misalignment is discussed in more detail subsequently. Shown in the inset of Figure 8.5(b) is the strength of the electric field, which varies linearly with ΔV as expected according to 16.6 kV/cm per volt. To verify that applied biases of $\pm V_L$ along the x-direction does not affect the field in the y-direction along the other two gates biased at V_g, the conduction band energy was studied for a 1D y-cut across the pyramid (data not shown, although evident in Figure 8.5(a)). The results show no change in the conduction band energy, concluding that it is possible to apply an in-plane field in the desired crystal direction.

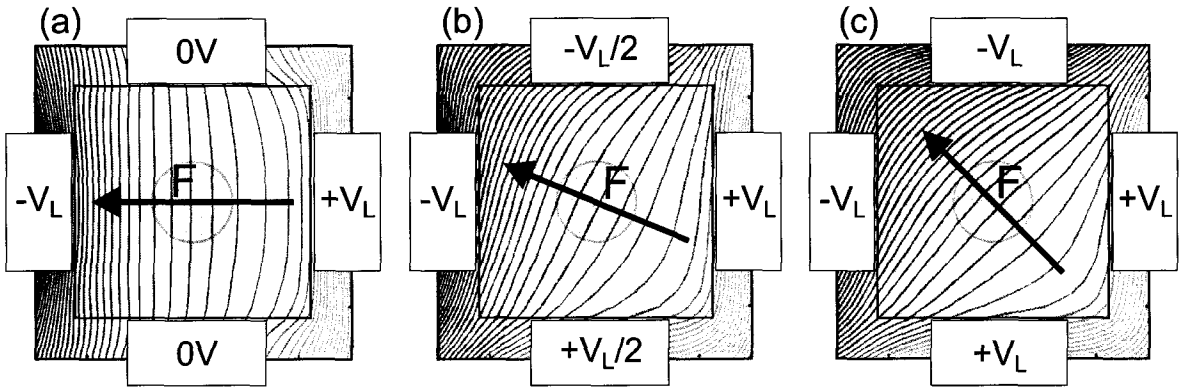

Figure 8.6: Demonstration of applied electric field in any crystal orientation. By manipulating the applied gate voltages, the electric field can be rotated about the pyramid in-the plane of the quantum dot. Examples are shown for angle of rotation with respect to x-direction at (a) 0° (b) 22.5° and (c) 45°. The contour lines represent equipotential surfaces due to the applied voltages on each gate. The direction of electric field, F, is perpendicular to the equipotential surfaces, with strength determined by the spacing between contour lines (*i.e.*, increases for smaller spacing). The dot, four gates, and pyramid dimensions are shown schematically. The dot diameter is 30 nm and 2D-slice is at a distance of 30 nm from the pyramid apex. The dimensions of pyramid is 90×90 nm at this 2D cross-section.

8.3.3 Rotation of lateral electric field

In addition to applying a lateral electric field in one crystal orientation, it is possible to rotate the electric field in any crystal orientation in the plane of the quantum dot. First, a lateral electric field is obtained by biasing the left (V_L) and right (V_R) gate metal at $V_g \pm V_L = \pm V_L$ as described in the previous section, which is also shown in Figure 8.6(a) with $V_g = 0$. Next, the top metal (V_T) and bottom metal (V_B) are biased such that ($V_L = V_T$) and ($V_R = V_B$) as shown in Figure 8.6(c). Here, the electric field is rotated by 45° compared to Figure 8.6(a). As an intermediate step, Figure 8.6(b) depicts the electric field orientation in between the two cases of Figures 8.6(a) and 8.6(c), with $V_B = +V_L/2$ and $V_T = -V_L/2$. The angle of rotation in this case is 22.5° with respect to the x-axis.

The calculations presented here in four terminal top-gate devices demonstrate the significant advantage over two terminal top-gate devices. Four gates provide the ability to apply an electric field in any crystal orientation; a situation that is not possible for two terminal devices since in this case a lateral field can only be applied along one crystal direction.

8.3.4 Dot misalignment

In the e-beam process to precisely position electrostatic gates around the periphery of the quantum dot, there is the possibility that the dot is not exactly in the centre of the top four gates. In such cases, the potential at the location of the dot is modified compared to perfect alignment. To understand how the dot potential is modified due to dot misalignment (or gate misalignment), the potential in the InP pyramid is studied as a function of possible dot locations. Depicted in Figure 8.7(a) is a 1D x-cut across the pyramid at a distance 30 nm below the pyramid apex with various applied top-gate voltages held at the same negative potential. The conduction band energy is subtracted at each applied bias for direct comparison since this curvature cannot be observed on the larger energy scale as in Figure 8.4. A slight misalignment in the dot position from the centre of the top four gates translates into a modification of the dot potential. With increasing negative potential on the top gates, a small dot misalignment corresponds to an extra component that increases the conduction band energy linearly with gate voltage. For typical dot misalignments corresponding to $\pm 10 - 30$ nm, the modified dot potential is small. Although the conduction band energy shift is still comparable to the energy scale in quantum dots, the operating voltage required to empty (charge) the dot is shifted to slightly lower biases. This effect is negligible since the operating voltage can be easily corrected. The main

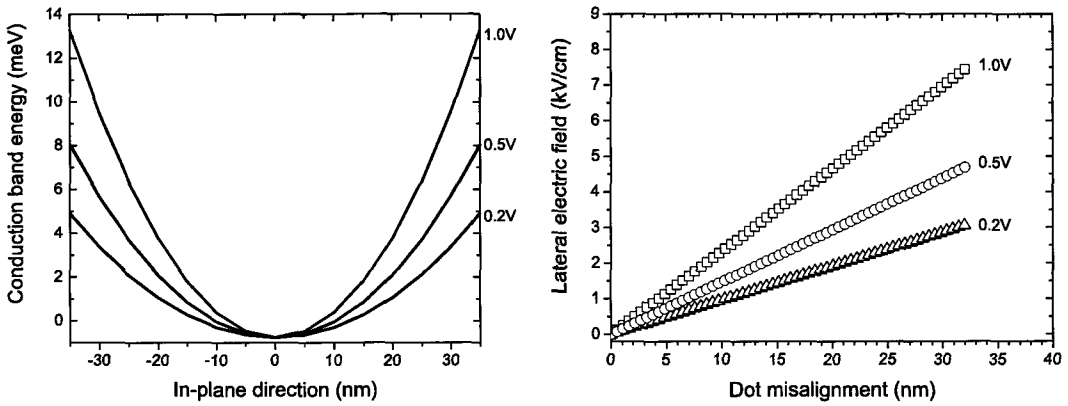

Figure 8.7: (a) In-plane cut across the pyramid at a distance of 30 nm from the pyramid apex. The conduction band minimum is shown at applied voltages of $V_g = -0.2\,\mathrm{V}$, $V_g = -0.5\,\mathrm{V}$, and $V_g = -1.0\,\mathrm{V}$ with all four top gates biased at equivalent negative potentials. Each curve has an offset such that the conduction band energy is 0 eV with perfect alignment for direct comparison. (b) Modification of in-plane lateral electric field due to slight dot misalignment. Note that *s*-shell excitonic transitions are expected to quench at lateral fields of greater than 10 kV/cm.

concern for dot misalignments is the modification of the in-plane electric field.

Shown in Figure 8.7(b) is the lateral electric field strength for applied biases of the four top gates held at the same potential of $V_g = -0.2\,\mathrm{V}$, $V_g = -0.5\,\mathrm{V}$, and $V_g = -1.0\,\mathrm{V}$, as a function of possible dot misalignments. An increase in dot misalignment corresponds to to an increase in the lateral electric field. Thus, at applied biases required to empty the dot in experiment for a device with dot misalignment, there is an expected built-in lateral electric field. The strength of the built-in lateral field is strongly dependent on applied biases required for device operation (*i.e.*, neutral dot for entangled photon pair generation). A built-in lateral electric field is indeed observed in experiment and is discussed in detail in Section 8.5.3.

8.4 Electron number control

Single electron charging is demonstrated in Figure 8.8(a) by monitoring the single-dot PL as a function of vertical electric field (reverse bias). In these electric field measurements, the excitation power was chosen to observe only single excitonic emission (*i.e.*, the dot is occupied with less than one exciton on average according to Poisson statistics). The charging data displayed in Figure 8.8(a) is similar to that obtained for single InGaAs/GaAs quantum dots which emits at shorter wavelengths [5]. Here, this result is typical for a gated, single InAs/InP quantum dot on the pyramidal nanotemplate and has been observed for ten individual quantum dots emitting close to the telecommunications band of $1.55\,\mu$m. In the charging data presented here, there are discrete changes in the excitonic emission from the s-shell corresponding to X^0 (neutral exciton), X^- (singly charged exciton), and X^{2-} (doubly charged exciton) species as the electric field is tuned.

The number of electrostatically induced electrons changes as a function of reverse bias depending on the position of the electron Fermi level, ϵ_F, with respect to the quantum dot energy levels. The position of ϵ_F is shown schematically in Figure 8.8(b) for three different reverse biases, $V_G = 0\,\mathrm{V}$, $V_G = 1.1\,\mathrm{V}$, and $V_G = 1.8\,\mathrm{V}$, corresponding to X^{2-}, X^-, and X^0, respectively. At high reverse bias, $V_G = 1.8\,\mathrm{V}$, ϵ_F lies below the quantum dot ground state and the quantum dot is empty since tunneling via the n-doped back gate is suppressed. In such circumstances, the PL probes only that of X^0 since there are zero electrostatically induced electrons. At higher reverse biases than $V_G = 2.3\,\mathrm{V}$, the emission from the dot quenches as the tunneling rate of photoexcited carriers out of the dot exceeds their radiative lifetime and carriers contribute to photocurrent [3, 101]. With decreasing reverse bias, ϵ_F crosses the energy level of

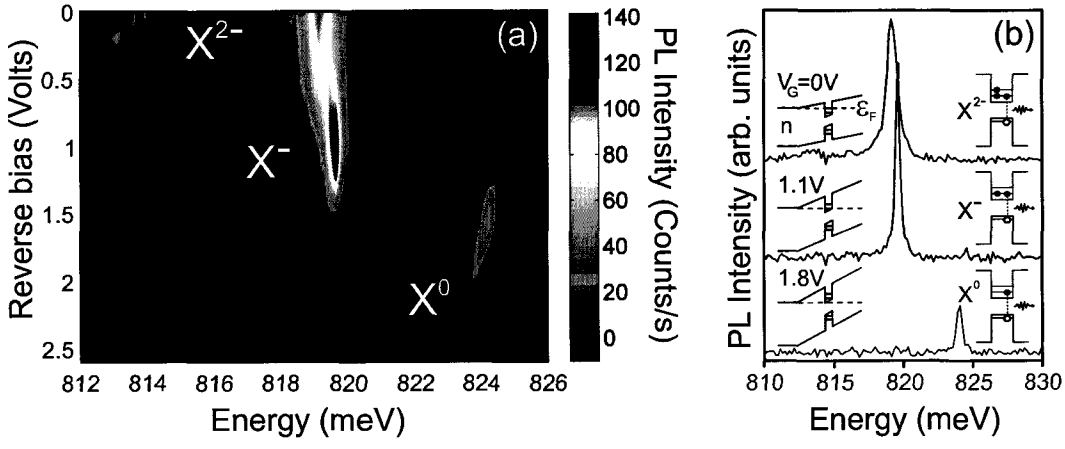

Figure 8.8: (a) Typical PL spectra (contour plot) for an individual, pre-positioned InAs/InP quantum dot as a function of vertical electric field (reverse bias). Single electron control is demonstrated by discrete changes in the optical spectra. For this particular dot, the electron number can be tuned from a quantum dot containing two electrostatically induced electrons (X^{2-}), to an empty dot, where the PL probes only that of X^0. The X^{2-} intensity of the lower emission peak is multiplied by a factor of three. (b) Individual spectra under reverse bias of the device for three top gate biases, $V_G = 0\,\mathrm{V}$, $V_G = 1.1\,\mathrm{V}$, and $V_G = 1.8\,\mathrm{V}$, corresponding to X^{2-}, X^-, and X^0, respectively.

the quantum dot ground state and a single electron tunnels into the quantum dot via the n-doped back gate. Thus, the quantum dot contains a single excess electron and the addition of an optically excited exciton corresponds to the singly charged exciton, X^-. The addition of the extra electron shifts the exciton recombination from X^- to $4.7\,\mathrm{meV}$ below that of X^0 due to many body effects and Coulomb interactions [74] (see Section 2.4 for more details). Moreover, the linewidth of X^- broadens from $\sim 0.3\,\mathrm{meV}$ at $1.2\,\mathrm{V}$ to $\sim 1\,\mathrm{meV}$ at $0.4\,\mathrm{V}$ reverse bias. This broadening of the emission line is indicative of additional charges being added to the system [5]. For $V_G < 0.4V$, an additional discrete jump in the optical spectra from X^- to X^{2-} is observed, where two excess electrons are electrostatically induced into the quantum dot. For X^{2-}, two emission lines are observed. This is characteristic of X^{2-} decay and corresponds

to the possible singlet and triplet configurations of the final state with corresponding anti-parallel and parallel spin orientations, respectively [5]. In comparison with the triplet state, singlet emission is expected at lower emission energy and with reduced amplitude, as observed in experiment. The singlet configuration of X^{2-} decay is more easily observed at higher excitation powers than the data presented in Figure 8.8. From the difference of the singlet and triplet emission peaks, an s-p electron-electron exchange interaction energy of 5.8 meV is obtained. The differences in energies of the three excitonic complexes are remarkably similar to the calculations of U. Hohenester *et al.* [74]. Details of these few particle interaction calculations are presented in Section 2.4.

8.4.1 Excitonic dipole

Of particular importance, there is an observed asymmetry of the excitonic Stark shift about zero electric field. The asymmetric Stark shift can be observed more clearly in Figure 8.9, where the peak positions of X^0 (black squares) and X^- (blue circles), extracted from Figure 8.8 using a Lorentzian lineshape, are plotted as a function of vertical electric field (reverse bias). Here, an offset is applied to the X^- energy to obtain a quadratic fit of the data for both peaks simultaneously. The reduction in dipole resulting from an additional charge being added to the system is expected to be negligible ($\sim$0.02 nm for one additional hole) [133].

The asymmetric Stark shift results from the existence of a built-in dipole at zero electric field which may be attributed to strain from the heterointerface of the InAs quantum dot and surrounding InP or by dot shape and composition [101,134]. In such circumstances, the electron and hole wavefunctions are spatially separated along the growth direction at zero electric field. Thus, the response of the excitonic transitions

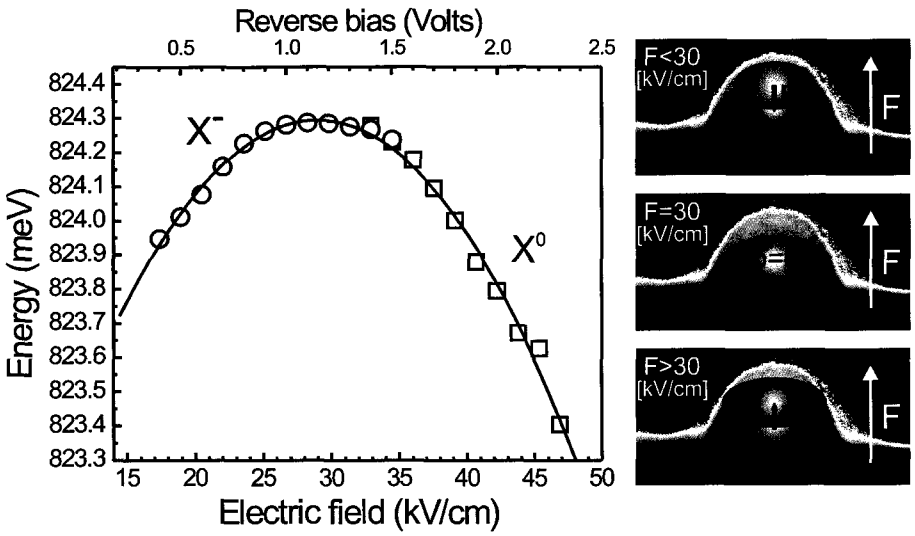

Figure 8.9: Left panel: Stark shift of X^0 (black squares) and X^- (blue circles) as a function of vertical electric field for a single InAs/InP quantum dot on pyramidal nanotemplate. Here, the X^- is offset by a constant energy. From a quadratic fit of the data (solid black line), the built-in dipole and Stark shift is obtained. The size and direction of the built-in dipole ($p/e \sim 1.6\,\mathrm{nm}$) indicates that the InAs quantum dot composition is uniform. Right panel: Schematic view of electron-hole wavefunction alignment at fields of $F < 30\,\mathrm{kV/cm}$, $F = 30\,\mathrm{kV/cm}$, and $F > 30\,\mathrm{kV/cm}$.

with applied field provide important information about the quantum dot such as alignment of electron and hole wavefunctions and dot composition [101, 134]. The electron-hole separation, $s(F)$, is modified in the applied field, F, according to

$$s(F) = s_0 + \beta F, \tag{8.2}$$

where s_0 is the electron hole separation at $F = 0$, and β is the sum of the polarizabilities for the electron and hole wavefunctions or the Stark shift. Thus, the excitonic dipole is modified in the applied electric field according to

$$p(F) = es(F) = e\left(s_0 + \beta F\right). \tag{8.3}$$

Since the energy of a dipole, p, in an electric field is $E = \vec{p} \cdot \vec{F}$, one obtains the

perturbation of the excitonic energy with applied field,

$$\Delta E = e\left(s_0 F + \beta F^2\right). \tag{8.4}$$

Hence, the transition energy can be expressed in terms of the transition energy at zero electric field E_0, and the Stark shift perturbation energy ΔE:

$$E = E_0 + \Delta E = E_0 + e s_0 F + e\beta F^2. \tag{8.5}$$

From a quadratic fit of the data (solid line), a zero field electron-hole separation, s_0 of $1.58\pm0.05\,\mathrm{nm}$, and Stark shift, β, of $2.7\,\mu\mathrm{eV\,cm^2/kV^2}$ is obtained, corresponding to a built-in dipole at zero electric field of $p/e \sim 1.6\,\mathrm{nm}$. The direction of the measured dipole is consistent with conventionally grown InAs/InP quantum dots as obtained by Stark shift spectroscopy [10]. The measured built-in dipole, $p/e \sim 0.8\,\mathrm{nm}$, of conventionally grown InAs/InP quantum dots is a factor two smaller than the one measured here ($p/e \sim 1.6\,\mathrm{nm}$). The larger built-in dipole of gated InAs/InP quantum dots in the pyramidal nanotemplate compared to conventionally grown ones may be due to enhanced piezoelectric fields for larger dot size in the pyramidal nanotemplate. For all dots measured in the present study, the orientation of the built-in dipole was in the direction of the applied field; from dot apex to base and the measured Stark shifts were comparable to that expected for InAs/InP quantum dots within a single particle picture ($\beta = 1.7\,\mu\mathrm{eV\,cm^2/kV^2}$).

To explain the observed response of single excitonic transitions to electric field in the gated InAs/InP quantum dot presented here, the electron wavefunction must lie above the hole at zero electric field (see right panel of Figure 8.9). With increasing electric field, the field induced dipole cancels the built-in dipole, *i.e.*, the applied field pulls the electron and hole wavefunctions together with corresponding blue shift of

the excitonic emission. At the maximum transition energy, the electron and hole wavefunctions cross and the dipole is zero. At this applied field (29 kV/cm $\sim$ 1.15 V), the electron-hole wavefunction overlap is maximized, which can be observed in the PL intensity contour plot of Figure 8.8. As the electric field is increased further, there is a redshift of the excitonic energy since the dipole changes sign and is in the same direction as the applied field. The electron and hole are separated once again and the overlap is reduced as observed experimentally. For fields in excess of 29 kV/cm, an inverted electron-hole alignment is obtained (hole wavefunction above electron wavefunction).

The magnitude of the measured dipole of $p/e = 1.6\,\text{nm}$ for a single InAs/InP quantum dot on a gated pyramid is 3-4 times larger than that obtained for randomly located InAs/GaAs quantum dots and in the opposite direction [4, 101]. The magnitude of the dipole for InAs/GaAs quantum dots is approximately $p/e = -0.4\,\text{nm}$ as measured by P.W. Fry and co-workers [101] or $p/e = -0.5\,\text{nm}$ as measured by F.Findeis and co-workers [4]. In the work of P.W. Fry et al., the experimentally measured dipole data required an inverted electron-hole alignment at zero electric field (*i.e.*, hole wavefunction above electron wavefunction) [101]. To explain this behavior, a combination of both dot shape truncation and Ga diffusion within the nominally pure InAs dots was required. The need for compositional grading of Ga remains true for dots of any shape in which the dot base is larger than the dot apex [101]. The experimentally measured dipole in InAs/InP dots is of opposite sign to that observed by P.W. Fry *et al.* suggesting that the composition of these InAs/InP quantum dots is uniform. Although it might be possible for other combinations of dot shape and

composition gradient to account for the direction of the measured dipole (*i.e.*, non-uniform dot composition), the magnitude of the dipole may exclude this possibility since it is approximately 3-4 times larger than observed for InAs/GaAs dots. In calculations by J.A. Barker *et al.*, a dipole of $p/e \geq 0.8\,\mathrm{nm}$ is required to ensure only pure InAs dot composition [134] as indeed measured here. In fact, for the experimentally investigated dot shown here, the measured dipole is a factor two larger. Comparison to the calculations of J.A. Barker *et al.* suggests that to obtain the experimentally observed dipole, the InAs composition should be uniform and that the alignment of electron wavefunction is on top of the hole at zero electric field [134]. Additionally, the quantum dot should be highly truncated with base width dimensions larger than the apex. This is indeed the case as InAs/InP quantum dots are known to have a square based pyramidal geometry with step-like monolayer fluctuations in height, where the base width dimensions are larger than the apex [135]. The result of uniform InAs dot composition is consistent with Stark shift spectroscopy measurements made on untemplated InAs/InP quantum dots [8, 10] and is corroborated by independent studies of conventionally grown InAs/InP quantum dots [10, 131]. In the work of C. Dion *et al.* uniform dot composition was determined by a combination of PL and transmission electron microscopy measurements with tight-binding and Bloch-wave calculations [131]. Elsewhere, pure InAs composition was found for twofold stacked InAs in InP by cross-sectional scanning-tunneling microscopy [136].

Prior to the work of Fry *et al.*, theoretical calculations predicted an alignment of electron wavefunction above that of the hole at zero electric field [52, 137] similar to the experimental results presented here. A calculation by M. Grundmann *et al.* is shown in Figure 8.10 [137]. The calculation shows electron and hole wavefunctions

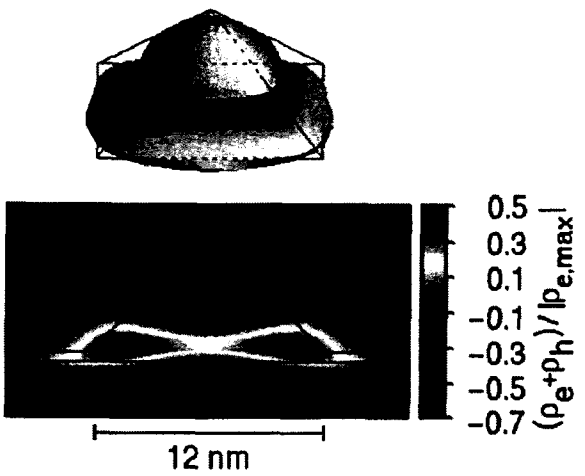

Figure 8.10: Calculated electron (blue) and hole (red) wavefunction alignment at zero electric field for a pure InAs pyramidal quantum dot embedded within a GaAs matrix. Due to strain effects, the hole is strongly localized towards the base of the dot. In contrast, the electron is more localized near the centre of the dot resulting in an electron-hole wavefunction alignment with the electron positioned above that of the hole. The dipole in this dot is calculated as $p/e = 7.7$ Å. Reproduced from M. Grundmann et al. [137].

for a pure pyramidal InAs quantum dot embedded in a GaAs matrix obtained using a single band $\mathbf{k} \cdot \mathbf{p}$ model. When assuming uniform InAs dot compositon, the alignment of electron above the hole is predicted for all dot shapes where the lateral size decreases from base to apex. This is a result of the strain-induced form of the valence band and conduction band edge profile and the difference in effective mass ratios along the growth direction (*i.e.*, $m^*_{hh} > m^*_e$) [101]. Due to compressive biaxial and hydrostatic strain, the heavy-hole wavefunction (red shading) is strongly localized towards the base of the dot where the lateral dimensions are largest. In contrast, the electron is unaffected from biaxial strain due to the lighter effective mass, however; the conduction band is sensitive only to hydrostatic strain resulting in the electron wavefunction (blue shading) being localized near the centre of the dot.

8.4.2 Fine-structure splitting of charged exciton complexes

Studying the fine-structure of the observed emission peaks from Figure 8.8 is used to confirm the assignment of charged exciton complexes in the bias dependent PL spectra. Shown in Figure 8.11 are the horizontal (black) and vertical (red) polarizations for the PL emission at fixed biases of X^0, X^-, and X^{2-}, respectively. The fine structure splitting (FSS) was determined by using a Lorentzian curve-fitting procedure as in Ref. [47] (similarly to Figure 7.5). The observed FSS of X^0 is approximately three times greater than that of X^{2-} and there is no detectable FSS for X^- as expected. Perturbative calculations suggest that the energy scale of the e-h exchange for X^0 should be a factor 2 larger than that of X^{2-}. In contrast, the e-h exchange for X^- is expected to be quenched since the e-h exchange interaction involving the spin up electron cancels that of the spin down electron [64]. The observed FSS taken together with linewidth, built-in dipole, and Stark shift of the observed PL transitions from Figure 8.8 confirms the ability to precisely control the number of electrons being electrostatically added to the deterministically positioned InAs/InP quantum dot.

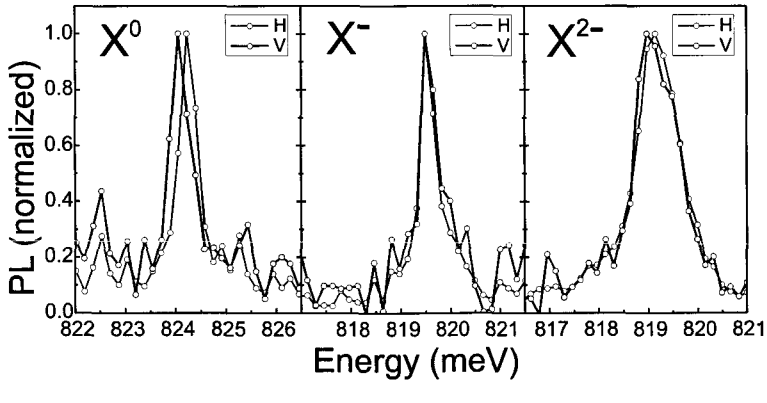

Figure 8.11: Fine-structure at fixed bias for X^0, X^-, and X^{2-}, respectively. The FSS of X^0 is 136±5 μeV, and X^{2-} is 45±3μeV, while no detectable FSS is observed for X^- as expected.

8.5 Combined vertical and lateral electric fields

A single InAs quantum dot embedded in a gated InP pyramid is presented as a function of both vertical and lateral electric field. Operation of the device is shown schematically in Figure 8.12(b) and is achieved by applying identical negative potentials, V_g, to the four top Schottky gates with respect to the global back gate to first precisely control the confined charge as discussed in detail in the previous section. On the same quantum dot, two opposite side gates are biased at $V_g \pm V_L$ such that a lateral electric field is applied in the plane of the quantum dot. The binding energy of the biexciton is shown to be manipulated by the in-plane field and controllably tuned by more than 1.5 meV. Such a prominent tuning range is desirable for removal of the biexciton binding energy and therefore production of entangled photon pairs on a dot to dot basis by simply tuning a voltage.

In comparison to theoretical calculations, the dependence of the exciton, and biexciton in a lateral electric field suggests that the confining potential for single dots in pyramid nanotemplates are square-like in the plane of the quantum dot. The square-like confining potential obtained for dots in gated pyramids is in contrast to positioned dots in ridge nanotemplates, which exhibit a parabolic confining potential (see Chapter 6). However, in both types of dots, there is an expected crossing of the exciton and biexciton at finite field such that entangled photon pairs are generated. Finally, SEM images of uncapped samples from both dots on pyramids and ridges are presented that corroborates the interpreted results. Additionally, the lateral field dependence found for the exciton and the biexciton suggests that there is a large built-in electric field at $V_L = 0$ corresponding to a dot misalignment with respect to the four top Schottky gates (see Section 8.3).

8.5.1 Applied vertical electric field

Reproducibility of the charging experiments are shown in Figure 8.12(a), where the charge state is controllably tuned from two excess electrons confined in the dot (X^{2-}) to an empty dot where PL probes only that of X^0. For this particular dot, the dot is emptied at applied biases of $V_g = -1.15\,\mathrm{V}$. To demonstrate control of the biexciton binding energy as a function of the in-plane electric field, the excitation power is increased to observe both the exciton (X^0) and biexciton (XX) simultaneously. Higher excitation power data is shown in 8.12(c). This data is taken at $V_g = -1.5\,V$ since the operating voltage required to observe neutral exciton states shifts to larger reverse biases at higher excitation powers due to electric field screening. To observe a signal of XX that is comparable to X^0, the singly charged exciton (X^-) is also present, identified by lack of fine structure splitting in Figure 8.12(c). The identification of X^0 and XX is performed using polarization dependent PL spectroscopy as described in Section 7.3. To briefly summarize, the exciton and biexciton exhibit a fine-structure splitting, but with reversed polarization. In this particular dot, XX is observed at an energy of 875.7 meV, which is 3.3 meV below that of X^0 (879 meV). Additionally, a fine-structure splitting of of 190 μeV is obtained.

The energy of the identified X^- PL transition is consistent with the presented vertical field data. At these large vertical electric fields, it is also possible that the excited states of the biexciton lead to a charge state configuration in the dot after p-shell electrons or holes tunnel out of the dot. The observation of the positively charged exciton, X^+ (two holes, one electron), is more apparent in the lateral electric field data discussed subsequently.

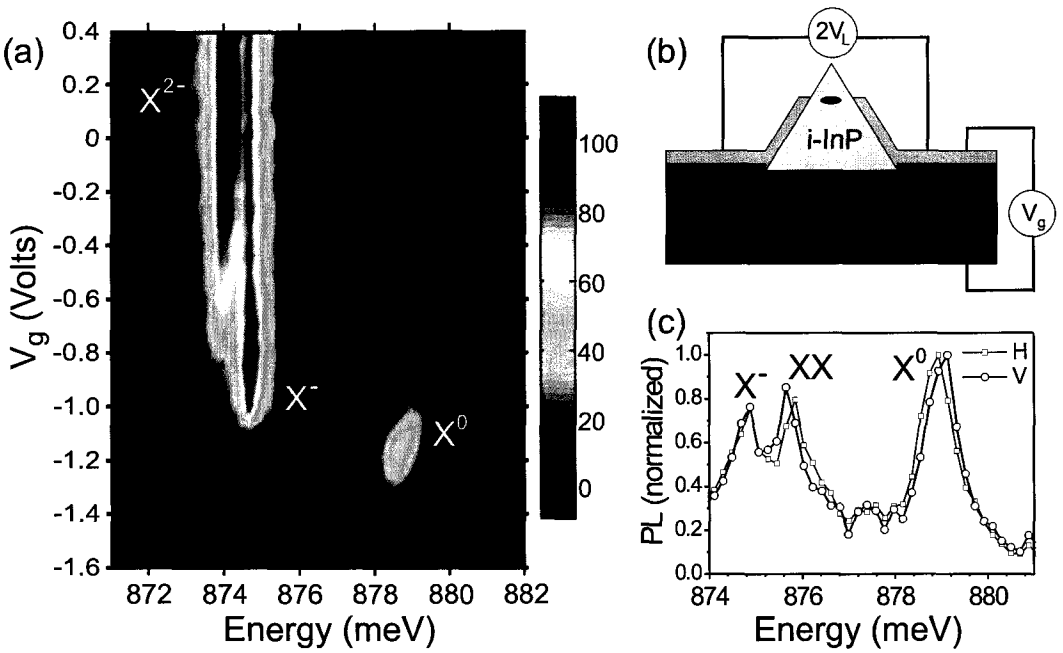

Figure 8.12: (a) Reproducibility of charging experiments for gated pyramid containing a single prepositioned quantum dot. Scale bar represents PL intensity in counts per second. (b) Schematic view of device structure used in experiment for combined vertical and lateral electric fields. (c) Identification of X^0 and XX spectral lines using polarization dependent PL spectroscopy.

8.5.2 Applied lateral electric field

The advantages of a vertical electric field applied to a single quantum dot compared to ungated dots are that the quantum dot is ascertained to be initialized to the desired charge configuration and that a more stable environment surrounding the quantum dot can be achieved for device operation, which is free of trapped charges. In this study, the quantum dot is first initialized to the neutral exciton state and the excitation power is increased to observe both the biexciton and exciton simultaneously (see previous section). On the same quantum dot, two opposite gates are biased at $V_g \pm V_L$ in order to apply a lateral electric field. The ability to apply an electric field in the plane of the quantum dot is desirable for entangled photon pair generation

(see Chapter 7). The bias difference between the two side-gates is $\Delta V = 2V_L$. PL data from such a dot as a function of lateral electric field (ΔV) is shown in Figure 8.13(a) represented as a contour plot. Of particular significance is that both X^0 and XX are observed simultaneously as a function of lateral field; a situation that was not possible for dots on ridge nanotemplates due to electric field screening [26]. The peak positions of the observed emission peaks from Figure 8.13(a) extracted using a lorentzian line-fitting procedure are depicted in Figure 8.13(b). Both X^0 and XX exhibit a quadratic field dependence in which the maximum transition energy occurs at an applied bias that is non-zero. The non-zero maximum for the applied lateral field (ΔV) is attributed to a built-in electric field resulting from a small dot misalignment with respect to the four top Schottky gates (see Section 8.3). As an example, for a gate spacing of 200 nm (400 nm), the built-in lateral electric field at $\Delta V = 0$ corresponds to 11.3 kV/cm (5.6 kV/cm) utilizing the electric field calibration procedure as described in Section 6.4. Thus for one direction of ΔV, the X^0 transition quickly quenches, while in the other field direction it grows, reaches a maximum and then diminishes as observed in Figure 8.13(a). Additionally, since the observed redshift for X^0 is much stronger than that of the XX transition, this leads to a tuning of the XX binding energy, Δ_{XX}, by more than 1.5 meV. The strong Δ_{XX} dependence in a lateral electric field exhibiting a large tuning range is presented in Figure 8.13(c). Such a prominent tuning range is desirable for removal of the XX binding energy and thus the production of entangled photon pairs near the telecommunications band of 1.55 μm (see Chapter 7). To experimentally realize removal of the biexciton binding energy, the initial binding energy of XX must be smaller than the quantum dot presented here. Tuning of Δ_{XX} is possible via the growth conditions of the nanotemplate

and was shown to depend on dot height for single dots in ridge nanotemplates (see Section 7.5).

In contrast to dots on ridges, the XX electric field dependence for dots in pyramids does not exhibit a blueshift. Instead, the XX shows a very weak redshift. Such an electric field dependence is not expected for an in-plane 2D parabolic potential presented in Chapter's 5 and 6. Thus, by comparison to theoretical calculations, details of the underlying quantum dot potential can be ascertained. Results of the theoretical calculation for a square-like confining potential in the plane of the quantum dot are shown for one direction of the field in Figure 8.13(d). The calculations are carried out in the effective mass approximation and include Coulomb interactions and correlation effects. The PL amplitudes in Figure 8.13(d) are extracted utilizing Fermi's golden rule for the 2D square-like confining potential. Details of the computational method are similar to that of the 2D parabolic confinement potential, which can be found in Chapter 5.

The calculated electric field dependence in Figure 8.13(d) is in excellent qualitative agreement with the observed experimental data. Both the X^0 and XX transitions exhibit a redshift, but with the X^0 transition shifting more strongly than that of the XX. Moreover, both the X^0 and XX quench as the electron and hole are separated via the lateral field. These results suggest that the in-plane confinement potential for a single dot in a pyramid nanotemplate is square-like compared to dots in ridges, which exhibit a parabolic confining potential. Of particular significance is that the X^0 and XX cross at finite field of $F \simeq 10\,\mathrm{kV/cm}$, in which the biexciton binding energy is removed. In comparison to dots in ridges, the XX and X^0 PL transitions cross at $F \simeq 6.5\,\mathrm{kV/cm}$. Thus, it is expected that the biexciton binding energy is removed at

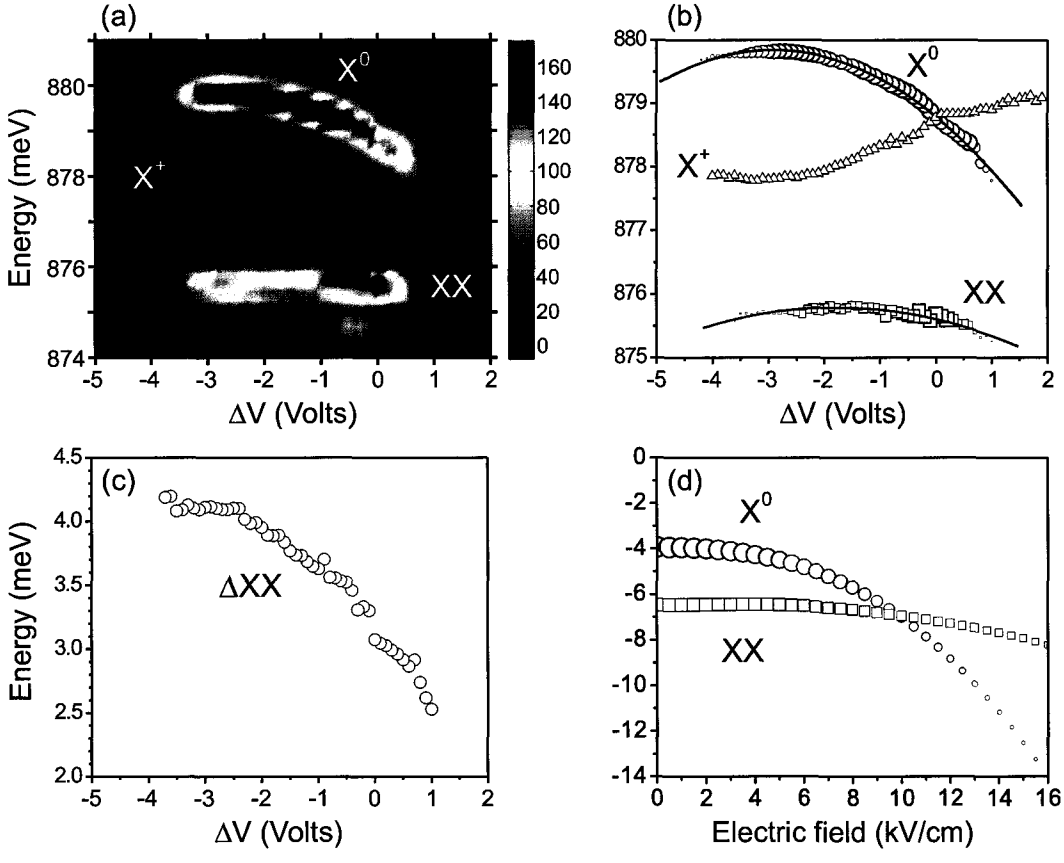

Figure 8.13: (a) Lateral electric field dependence of X^0, and XX in a gated pyramid containing a single, prepositioned quantum dot. XX is multiplied by a factor of 1.5. Scale bar represents PL intensity in counts per second. (b) Peak positions from (a) obtained using a lorentzian line-fitting procedure. The size of the symbols represent the integrated intensity of the X^0 and XX transitions. The faint X^+ line is included for completeness. (c) Tuning of biexciton binding energy, Δ_{XX}, in a lateral electric field over a large energy range ($\sim 1.5\,\text{meV}$). (d) Configuration interaction calculations of X^0 and XX in a lateral electric field using a square-like confinement potential in the plane of the quantum dot. The size of the symbols represent the PL amplitude calculated using Fermi's golden rule.

a higher electric field for dots in pyramidal nanotemplates (larger operating voltage).

Figure 8.13 shows the observed operating voltages for a single quantum dot in a pyramidal nanotemplate. These voltages are approximately a factor of 2 times larger than those observed for single dots in ridge nanotemplates (see Chapter 6). The experimentally observed bias voltages shown here for dots in pyramids are explained by theoretical calculations that suggest the X^0 and XX will quench at higher electric fields as compared to single dots in ridge nanotemplates (see Figure 8.15). However, there is a discrepancy in the experimentally observed electric field (ΔV) for the maximum PL transition energy for both X^0 and XX when compared to theory. In the theoretical calculations, the maximum PL transition energy occurs at the same electric field for both XX and X^0. In contrast, the maximum PL transition energies observed for XX and X^0 in experiment occur at slightly different values of ΔV (electric field). This finding is currently not well understood, although the discrepancy may be due to a small vertical electric field component that arises when the lateral electric field is tuned. Alternatively, microscopic details of the underlying X^0 and XX wavefunctions may attribute to this discrepancy. However, a symmetric in-plane electric field dependence has been observed in other dots, although the tuning range of Δ_{XX} is an order of magnitude smaller. Results from a single quantum dot exhibiting a more symmetric in-plane electric field dependence are presented in Figure 8.14. Similar to Figure 8.13, a non-zero ΔV (electric field) is observed for the maximum PL transition energy in 8.14(a), which is attributed to a built-in electric field resulting from dot misalignment. In this particular dot, the tuning range observed for Δ_{XX} is $160\,\mu$eV (Figure 8.14(c)).

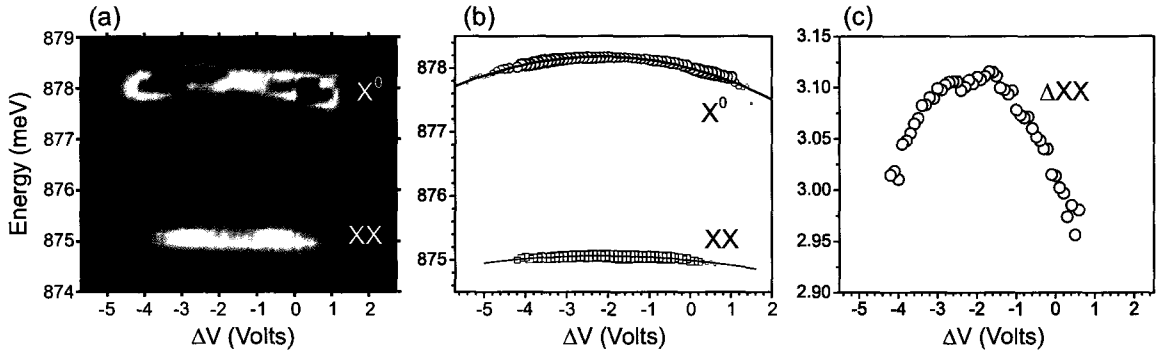

Figure 8.14: Reproducibility of in-plane electric field dependence for a single dot in a pyramid nanotemplate. (a) Electric field dependant PL. Maximum PL intensity in contour plot is 160 counts per second (represented by red). Minimum PL intensity is represented in blue. (b) Extracted peak positions from (a). (c) Tuning range of biexciton binding energy, Δ_{XX}, in a lateral electric field.

8.5.3 Determination of in-plane confinement potential for single dots in pyramid and ridge nanotemplates

The X^0 and XX dependence for the 2D square-like confining potential presented in Figure 8.13 and Figure 8.14 is strikingly different than that obtained for a 2D parabolic confinement potential. The 2D parabolic and square-like confinement potential (alternatively step-like potential in quantum mechanics) are compared in Figure 8.15. In the case of the square-like confinement potential in Figure 8.15(a), the X^0 exhibits a strong redshift, whereas for the parabolic confinement in Figure 8.15(b), the X^0 redshift is very small and is attributed to a stronger compensation of the single particle Stark shift (see Section 6.2.1). In the case of XX, the XX blueshifts for a parabolic dot and shows a very weak dependence for square-like confinement in the plane of the quantum dot. However, in both confinement potentials the physics is the same in that the X^0 and XX optical transitions cross at finite field such that generation of entangled photon pairs is a possibility (see Chapter 7).

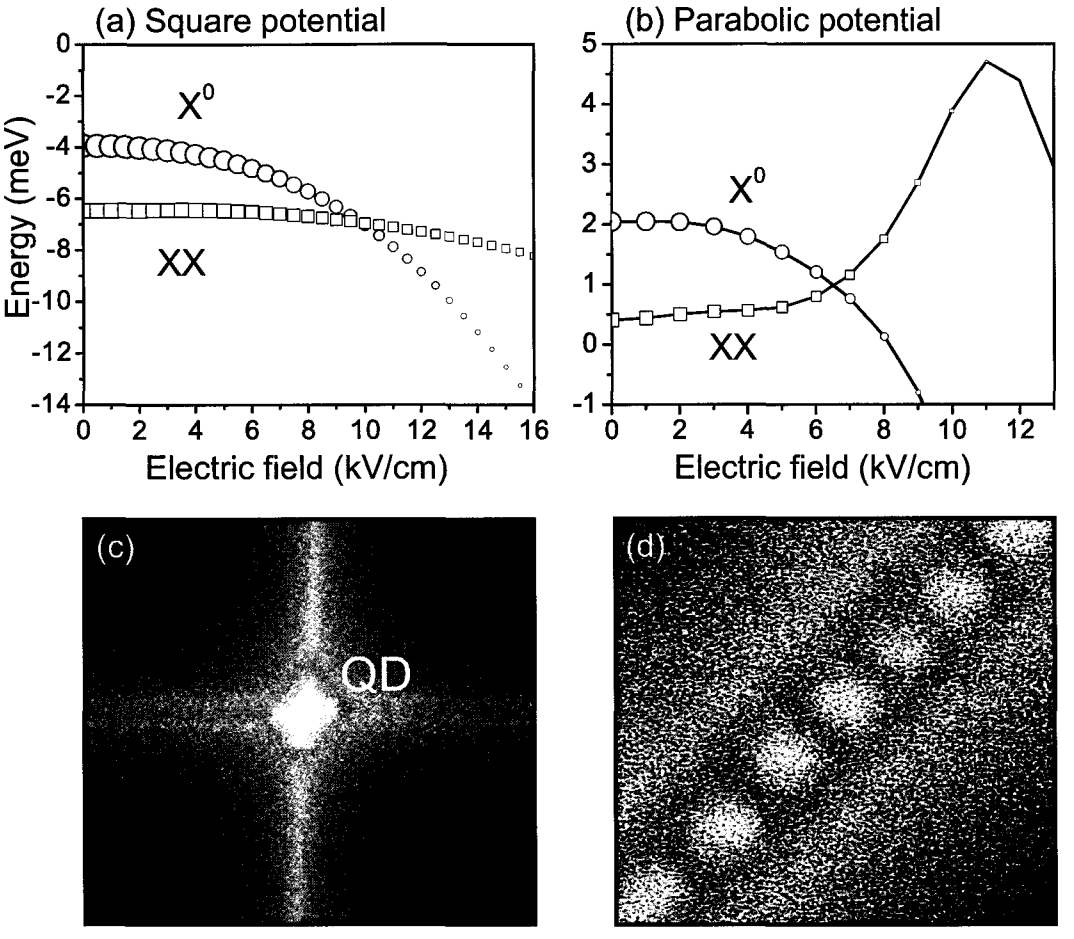

Figure 8.15: Configuration interaction calculations of (a) step-like (square) versus (b) parabolic in-plane confinement potential of the quantum dot. Plan-view SEM images of uncapped nanotemplates containing a (c) single InAs quantum dot at the apex of a InP pyramid nanotemplate and (d) single row of InAs quantum dots at the apex of the InP ridge nanotemplate. The single dot at the apex of the pyramid is square-like, which exhibits a step-like in-plane confinement potential in a lateral electric field. In contrast, dots on the ridge nanotemplate exhibit a circular shape and corresponding 2D parabolic in-plane confinement potential dependence in an electric field. The size of the InAs quantum dots presented here are 30-40 nm.

The electric field dependencies observed in experiment for a single dots on pyramid and ridge nanotemplates is captured by SEM images of uncapped samples shown in Figure 8.15(c) and Figure 8.15(d), respectively. The shape of the single quantum dot at the apex of the pyramid nanotemplate in Figure 8.15(c) is square-like which exhibits a square in-plane confinement potential in a lateral electric field. In contrast, a single dot on the apex of the ridge nanotemplate in Figure 8.15(d) is more circular and corresponds to an observed in-plane parabolic confinement potential in an electric field. Thus, by the observed electric field dependence in experiment, the in-plane quantum dot potential can be theoretically approximated and the shape of the dot inferred.

8.6 Conclusion

In summary, electron number control has been demonstrated via vertical electric fields from a single, deterministically positioned quantum dot emitting in the telecommunications band close to 1.55 μm. In contrast to the well studied InAs/GaAs quantum dot material system, the built-in dipoles of the InAs/InP quantum dots studied in this thesis are from dot apex to base; the strength of the dipole suggesting a uniform dot composition. Uniform dot composition is found to be consistent with independent studies of untemplated InAs/InP quantum dots.

Next, an in-plane lateral electric field is applied across the same quantum dot initialized to observe both the exciton and biexciton simultaneously. Of particular importance for this system is that the biexciton binding energy can be tuned by more than 1.5 meV. Such a prominent tuning range is ideal for removal of the biexciton binding energy and therefore generation of entangled photon pairs. Moreover, from

the observed electric field dependence of the exciton and biexciton, a step-like (square-like) in-plane confinement potential is deduced for the single InAs quantum dot on the InP pyramidal nanotemplate with observed square dot shape by SEM. The observed electric field dependence was compared to dots on ridges that exhibited an in-plane parabolic confinement potential and observed circular dot shape by SEM. Thus, a comparison between an electric field dependence for single dots on ridges versus a single dot at the apex of a pyramidal nanotemplate reveals information on the in-plane confinement potential.

Finally, two-dimensional and three-dimensional calculations for solutions of the Poisson equation were presented in order to understand the electron charging mechanism for single InAs quantum dots embedded in InP pyramidal nanotemplates since this device geometry is not planar as in current devices studied in the literature. The calculations showed that electron charging is possible for metal-semiconductor and metal-oxide-semiconductor devices. Counterintuitive to expectation, the metal-oxide-semiconductor device exhibited a greater effect on single electron charging. Additionally, due to the complexity of the gated pyramid device with four gates around the periphery of the quantum dot, three-dimensional Nextnano calculations are presented which verify the ability to apply an in-plane electric field in any crystal orientation of the quantum dot. In-plane electric field measurements for a single InAs quantum dot in pyramidal nanotemplate suggest that the quantum dot is not exactly in the centre of the top four Schottky gates when compared to three-dimensional Nextnano calculations. A built-in electric field resulting from the aforementioned dot misalignment was confirmed by the observed asymmetry about zero volts bias in the electric field dependence of exciton and biexciton.

The unique preparation strategy presented here to routinely contact a single quantum dot electrically envisions arrays of single spins that can be utilized for quantum information applications, as well as the ability to apply an electric field in any crystal orientation for the generation of entangled photon pairs.

Chapter 9

Conclusion and future work

The work presented in this thesis demonstrates precise control of electrostatic gate positioning around a deterministically positioned single quantum dot. The gates were designed to apply an electric field along the growth direction (vertical electric field) or in-plane of a single quantum dot (lateral electric field). The ability to manipulate such a dot post-growth with an applied electric field was shown to be desirable for applications in quantum information science such as generation of entangled photon pairs and initialization of a single electron spin including its manipulation. Moreover, an applied electric field allows electrical manipulation of the electronic structure of individual dots, thus affecting the optical emission properties of the biexciton-exciton radiative cascade or number of electrons residing in the quantum dot. The InAs quantum dots on InP (InAs/InP) nanotemplates studied in this thesis have the added benefit of a wavelength that can be tuned to the 1300nm and/or 1550nm range, ideal for fibre-based quantum cryptographic systems.

A lateral electric field applied across a single quantum dot demonstrated strong modification of Coulomb interactions of the confined carriers inside the quantum dot. First, the observed Stark shift ($\beta = 0.31\,\mu\text{eV}\ cm^2/kV^2$) of a single exciton involving

an s-shell electron and s-shell hole was shown to be two orders of magnitude less than that expected in a single particle calculation ($\beta = 144\,\mu\text{eV}\ cm^2/kV^2$). The observed compensation of the Stark shift in comparison to a single particle picture is understood through the exponential decay of the electron-hole Coulomb interaction under applied lateral electric field as the electron and hole are separated. Although the ground state exciton Stark shift is expected to be larger in a lateral electric field in comparison to a vertical one, a larger Stark shift is observed for the single excitonic ground state in a vertical field. Here, the observed Stark shift ($\beta = 1.7\,\mu\text{eV cm}^2/\text{kV}^2$) is comparable to a single particle picture ($\beta = 2.1\,\mu\text{eV cm}^2/\text{kV}^2$) for the single InAs/InP quantum dots studied in this thesis. There is no compensation expected in a vertical electric field due to the smaller dot dimensions along the growth direction ($\sim$ 3-5 nm) compared to the lateral direction ($\sim$ 30-40 nm). For these small dot dimensions, the applied field could not efficiently separate the electron and hole in a applied vertical field. Second, in addition to the small observed Stark shift of the ground state exciton, the in-plane electric field leads to the appearance of an excited state involving an s-shell electron and p-shell hole ($s-p$). Finally, a model is developed in collaboration with the Quantum Theory group at the National Research Council that describes the effects of the applied lateral electric field and appearance of the forbidden $s-p$ optical transition. The magnitude of the Stark shift for the $s-p$ transition was found to be in excellent quantitative agreement with theory since the e-h Coulomb interaction is significantly reduced at finite fields and therefore closer to the single particle picture. The observed modification of oscillator strengths for the excitonic transitions and the appearance of a normally forbidden excited state of the neutral exciton are in excellent agreement with many body, configuration-interaction calculations of the

emission spectra from Chapter 5.

The modification of Coulomb interactions of confined carriers inside a single quantum dot is advantageous for the generation of entangled photon pairs. The reduced electron-hole Coulomb interaction in an applied lateral electric field also leads to a reduction in biexciton binding energy and its removal. Since the biexciton is composed of two electron-hole pairs instead of only one, the Stark shift of the biexciton is even more strongly compensated in an applied lateral field compared to the exciton and in some cases even leads to a blue shift. In modeling the dot with a parabolic confinement potential, biexciton blue shifting was predicted compared to the red shifting exciton and was brought into resonance for a critical value of the electric field. In contrast, if the dot was modeled by a square confinement potential, it was expected that the biexciton and exciton exhibit a red shift with the exciton transition shifting more rapidly to lower energies than the biexciton again leading to the crossing of the two transitions. These predictions were observed experimentally for dots on ridge (parabolic confining potential) and pyramidal nanotemplates (square confining potential). Thus, both types of confining potentials demonstrated that it is possible to bring the biexciton and exciton transitions into resonance resulting in removal of the biexciton binding energy.

A scheme that relies on the removal of the biexciton binding energy was presented that overcomes a major issue that the scientific community has been struggling to overcome – the need to remove the anisotropic exchange splitting (AES) of the intermediate states in the biexciton-exciton radiative cascade. Instead, the proposed scheme presented in this thesis is robust to the presence of the AES. Once the binding energy of the biexciton is removed, the cross-colour transitons are degenerate and the

decay path cannot be distinguished. Thus, entangled photon pairs are generated. Removal of the biexciton binding energy was demonstrated for a single dot on a ridge nanotemplate. The major problem for the dots on ridges was the ability to observe both the exciton and biexciton as a function of lateral electric field due to electric field screening. Here it was only possible to observe the exciton before the crossing and biexciton after the crossing. However, it was possible to observe the biexciton and exciton simultaneously in a lateral electric field for dots on pyramidal nanotemplates. In the latter case, electric field screening was reduced since additional gates that controlled the confined charge in the quantum dot also depleted the surrounding quantum dot environment of charges. In these devices, the biexciton binding energy was tuned by a large energy range via the in-plane electric field ($\sim 1.5\,\mathrm{meV}$). Tuning of the biexciton binding energy was also investigated through dot growth. The growth for dots on ridges demonstrated that it was possible to tune the biexciton binding energy over a large energy range ($\sim 7\,\mathrm{meV}$) and through zero – a regime not achieved previously in large dots. The mechanism to remove the biexciton binding energy in large dots was determined to be piezoelectric fields. This finding contrasts that of small dots where the mechanism to remove biexciton energy is reduced correlations (due to decreased number of bound states and increased energy level spacing) and increased repulsive Coulomb interactions between confined carriers.

Finally, single InAs dots in InP pyramidal nanotemplates subject to vertical and lateral electric fields were studied. Precise control of the electron number was demonstrated in a vertical field from a single quantum dot emitting in the telecommunications band close to $1.55\,\mu\mathrm{m}$. The number of electrons was controllably tuned from two excess electrons down to zero. The ability to tune the number of electrons in

the quantum dot promises arrays of initialized spins for quantum information applications. In addition, the electronic dipole of the InAs/InP quantum dots studied in this thesis were investigated. In contrast to the well studied InAs/GaAs quantum dot material system, the built-in dipole of the InAs/InP quantum dots studied in this thesis are from dot apex to base; the strength of the dipole suggesting a uniform dot composition. Uniform dot composition is found to be consistent with independent studies of untemplated InAs/InP quantum dots. On the same quantum dot, the binding energy of the biexciton was tuned over a large energy range ($\sim$ 1.5 meV). Here, it was possible to observe both the biexciton and exciton transitions since the material surrounding the quantum dot could be depleted of charges within this device configuration.

Future work involves investigating the growth of single dots in pyramids such that the biexciton binding energy can be engineered within the tuning range of the applied lateral electric field thus leading to removal of the biexciton binding energy and generation of entangled photon pairs. Additionally, the four gates around the periphery of the quantum dot can be utilized to apply a lateral electric field in any crystal orientation. Various potentials can be investigated that lead to either the removal of biexciton binding energy or fine-structure splitting of the intermediate exciton states. If successful, the nanotemplate deposition technique promises arrays of entangled photon generators for quantum information applications. Such structures, emitting in the 1300nm and/or 1550nm range, are ideal for fibre-based quantum cryptographic systems and are of immense promise for gate controlled, integrated semiconductor entanglement sources for quantum repeater technologies.

Bibliography

[1] P. Michler, editor. *Single Quantum Dots: Fundamentals, Application and New Concepts*, volume 90 of *Topics in Applied Physics.* Springer-Verlag, Berlin, 2003.

[2] R. J. Warburton, C. Schflein, D. Haft, F. Bickel, A. Lorke, K. Karrai, J. M. Garcia, W. Schoenfeld, and P. M. Petroff. Optical emission from a charge-tunable quantum ring. *Nature (London)*, 405:926–929, 2000.

[3] F. Findeis, M. Baier, E. Beham, A. Zrenner, and G. Abstreiter. Photocurrent and photoluminescence of a single self-assembled quantum dot in electric fields. *Appl. Phys. Lett.*, 78(19):2958–2960, 2001.

[4] F. Findeis, M. Baier, A. Zrenner, M. Bichler, G. Abstreiter, U. Hohenester, and E. Molinari. Optical excitations of a self-assembled artificial ion. *Phys. Rev. B*, 63(12):121309, 2001.

[5] M. Baier, F. Findeis, A Zrenner, M. Bichler, and G. Abstreiter. Optical spectroscopy of charged excitons in single quantum dot photodiodes. *Phys. Rev. B*, 64:195326, 2001.

[6] M. Ediger, P. A. Dalgarno, J. M. Smith B. D. Gerardot, R. J. Warburton, K. Karrai, and P. M. Petroff. Controlled generation of neutral, negatively-charged and positively charged excitons in the same single quantum dot. *Appl. Phys. Lett.*, 86:211909, 2005.

[7] M. Ediger, G. Bester, A. Badolato, P. M. Petroff, K. Karrai, A. Zunger, and R. J. Warburton. Peculiar many-body effects revealed in the spectroscopy of highly charged quantum dots. *Nat. Phys.*, 3:774–779, 2007.

[8] M. E. Reimer, W. R. McKinnon, J. Lapointe, D. Dalacu, P. J. Poole, G. C. Aers, D. Kim, M. Korkusiński, P. Hawrylak, and R. L. Williams. Towards scalable gated quantum dots for quantum information applications. *Physica E (Amsterdam)*, 40(6):1790–1793, 2008.

[9] M. E. Reimer, D. Dalacu, J. Lapointe, P. J. Poole, D. Kim, G. C. Aers, W. R. McKinnon, and R. L. Williams. Single electron charging in deterministically positioned InAs/InP quantum dots. *Appl. Phys. Lett.*, 94(1):011108, 2009.

[10] M. E. Reimer, D. Dalacu, J. Lapointe, P. J. Poole, W. R. McKinnon, and R. L. Williams. Non-inverted electron-hole alignment in InAs/InP self-assembled quantum dots. *Phys. Status Solidi B*, 246(4):828–831, 2009.

[11] J. Berezovsky, M. H. Mikkelsen, O. Gywat, N. G. Stoltz, L. A. Coldren, and D. D. Awschalom. Nondestructive optical measurements of a single electron spin in a quantum dot. *Science*, 314:1916–1920, 2006.

[12] M. Atatüre, J. Dreiser, A. Badolato, and A. Imamoglu. Observation of faraday rotation from a single confined spin. *Nat. Phys.*, 3:101–106, 2007.

[13] M. H. Mikkelsen, J. Berezovsky, N. G. Stoltz, L. A. Coldren, and D. D. Awschalom. Optically detected coherent spin dynamics of a single electron in a quantum dot. *Nat. Phys.*, 3:770–773, 2007.

[14] J. Berezovsky, M. H. Mikkelsen, N. G. Stoltz, L. A. Coldren, and D. D. Awschalom. Picosecond Coherent Optical Manipulation of a Single Electron Spin in a Quantum Dot. *Science*, 320(5874):349–352, 2008.

[15] D. Press, T. D. Ladd, B. Zhang, and Y. Yamamoto. Complete quantum control of a single quantum dot spin using ultrafast optical pulses. *Nature (London)*, 456:218–221, 2008.

[16] X. Xu, D. A. Williams, and J. R. A. Cleaver. Splitting of excitons and biexcitons in coupled InAs quantum dot molecules. *Appl. Phys. Lett.*, 86(1):012103, 2005.

[17] H. J. Krenner, M. Sabathil, E. C. Clark, A. Kress, D. Schuh, M. Bichler, G. Abstreiter, and J. J. Finley. Direct observation of controlled coupling in an individual quantum dot molecule. *Phys. Rev. Lett.*, 94(5):057402, 2005.

[18] M. F. Doty, M. Scheibner, I. V. Ponomarev, E. A. Stinaff, A. S. Bracker, , V. L. Korenev, T. L. Reinecke, and D. Gammon. Electrically tunable g factors in quantum dot molecular spin states. *Phys. Rev. Lett.*, 97:197202, 2006.

[19] E. A. Stinaff, M. Scheibner, A. S. Bracker, I. V. Ponomarev, V. L. Korenev, M. E. Ware, M. F. Doty, T. L. Reinecke, and D. Gammon. Optical signatures of coupled quantum dots. *Science*, 311:636–639, 2006.

[20] G. J. Beirne, C. Hermannstdter, L. Wang, A. Rastelli, O. G. Schmidt, and P. Michler. Quantum light emission of two lateral tunnel-coupled (In,Ga)As/GaAs quantum dots controlled by a tunable static electric field. *Phys. Rev. Lett.*, 96:137401, 2006.

[21] Jia-Lin Zhu and Dong Xu. Effective tuning of exciton polarization splitting in coupled quantum dots. *Appl. Phys. Lett.*, 90:261119, 2007.

[22] D. Kim, S. E. Economou, S. C. Badescu, M. Scheibner, A. S. Bracker, M. Bashkansky, T. L. Reinecke, and D. Gammon. Optical spin initialization and nondestructive measurement in a quantum dot molecule. *Phys. Rev. Lett.*, 101(23):236804, 2008.

[23] R. J. Young, S. J. Dewhurst, R. M. Stevenson, P. Atkinson, A. J. Bennett, M. B. Ward, K. Cooper, D. A. Ritchie, and A. J. Shields. Single electron-spin memory with a semiconductor quantum dot. *New J. Phys.*, 9(10):365, 2007.

[24] A. Shields. Semiconductor quantum light sources. *Nat. Photonics*, 1:215–223, 2007.

[25] M. E. Reimer, M. Korkusiński, J. Lefebvre, J. Lapointe, P. J. Poole, G. C. Aers, D. Dalacu, W. R. McKinnon, S. Frédérick, P. Hawrylak, and R. L. Williams. Voltage induced hidden symmetry and photon entanglement generation in a single, site-selected quantum dot. arXiv:0706.1075 (unpublished).

[26] M. E. Reimer, M. Korkusiński, D. Dalacu, J. Lefebvre, J. Lapointe, P. J. Poole, G. C. Aers, W. R. McKinnon, P. Hawrylak, and R. L. Williams. Prepositioned single quantum dot in a lateral electric field. *Phys. Rev. B*, 78(19):195301, 2008.

[27] M. Korkusiński, M. E. Reimer, R. L. Williams, and P. Hawrylak. Engineering photon cascades from multiexciton complexes in a self-assembled quantum dot by a lateral electric field. *Phys. Rev. B*, 79(3):035309, 2009.

[28] D. Dalacu, M. E. Reimer, S. Frédérick, D. Kim, J. Lapointe, P. J. Poole, G. C. Aers, R. L. Williams, W. R. McKinnon, M. Korkusiński, and P. Hawrylak. Directed self-assembly of single quantum dots for telecommunication wavelength optical devices. *Laser Photonics Rev.*, pages 1–17, 2009.

[29] D. Chithrani, R. L. Williams, J. Lefebvre, P. J. Poole, and G. C. Aers. Optical spectroscopy of single, site-selected, InAs/InP self-assembled quantum dots. *Appl. Phys. Lett.*, 84(6):978–980, 2004.

[30] J. Lefebvre, P. J. Poole, J. Fraser, G. C. Aers, D. Chithrani, and R. L. Williams. Self-assembled InAs quantum dots on InP nano-templates. *J. Cyrstal Growth*, 234(2-3):391–398, 2002.

[31] M. H. Baier, E. Pelucchi, E. Kapon, S. Varoutsis, M. Gallart, I. Robert-Philip, and I. Abram. Single photon emission from site-controlled pyramidal quantum dots. *Appl. Phys. Lett.*, 84(5):648–650, 2004.

[32] H. Z. Song, T. Usuki, S. Hirose, K. Takemoto, Y. Nakata, N. Yokoyama, and Y. Sakuma. Site-controlled photoluminescence at telecommunication wavelength from InAs/InP quantum dots. *Appl. Phys. Lett.*, 86(11):113118, 2005.

[33] S. Kiravittaya, A. Rastelli, and O. G. Schmidt. Self-assembled InAs quantum dots on patterned GaAs(001) substrates: Formation and shape evolution. *Appl. Phys. Lett.*, 87(24):243112, 2005.

[34] J. M. Benoit, L. Le Gratiet, G. Beaudoin, A. Michon, G. Saint-Girons, R. Kuszelewicz, and I. Sagnes. Nanoepitaxy of InAs/InP quantum dots by metalorganic vapor phase epitaxy for 1.55 μm emitters. *Appl. Phys. Lett.*, 88(4):041113, 2006.

[35] D. L. Huffaker, C. P. Hains, N. Nuntawong, Y. C. Xin, P. S. Wong, L. Xue, S. R. J. Brueck, and L. Lester. Temperature-dependent photoluminescence from patterned InAs quantum dots formed using metalorganic chemical vapor epitaxy. *J. Appl. Phys.*, 99(3):033503, 2006.

[36] T. Ujihara, Y. Yoshida, W. S. Lee, and Y. Takeda. Size uniformity of InAs dots on mesa-structure templates on (001) InP substrates grown by droplet metal-organic vapor phase epitaxy method. *Appl. Phys. Lett.*, 89(8):083110, 2006.

[37] T. Hsieh, J. Chyi, H. Chang, W. Chen, T. Hsu, and W. Chang. Single photon emission from an InGaAs quantum dot precisely positioned on a nanoplane. *Appl. Phys. Lett.*, 90(7):073105, 2007.

[38] O. G. Schmidt, editor. *Lateral Alignment of Epitaxial Quantum Dots.* Springer, Berlin, 2007.

[39] P. Atkinson, S. Kiravittaya, M. Benyoucef, A. Rastelli, and O. G. Schmidt. Site-controlled growth and luminescence of InAs quantum dots using in situ Ga-assisted deoxidation of patterned substrates. *Appl. Phys. Lett.*, 93(3):101908, 2008.

[40] W. Sheng and P. Hawrylak. Atomistic theory of electronic and optical properties of InAs/InP self-assembled quantum dots on patterned substrates. *Phys. Rev. B*, 72(3):035326, 2005.

[41] N. Gisin and R. Thew. Quantum communication. *Nat. Photonics*, 1:165–171, 2007.

[42] K. Kowalik, O. Krebs, A. Lemaitre, S. Laurent, P. Senellart, P. Voisin, and J. A. Gaj. Influence of an in-plane electric field on exciton fine structure in InAs-GaAs self-assembled quantum dots. *Appl. Phys. Lett.*, 86(4):041907, 2005.

[43] R. J. Young, R. M. Stevenson, A. J. Shields, P. Atkinson, K. Cooper, D. A. Ritchie, K. M. Groom, A. I. Tartakovskii, and M. S. Skolnick. Inversion of exciton level splitting in quantum dots. *Phys. Rev. B*, 72(11):113305, 2005.

[44] R. M. Stevenson, R. J. Young, P. Atkinson, K. Cooper, D. A. Ritchie, and A. J. Shields. A semiconductor source of triggered entangled photon pairs. *Nature (London)*, 439:179–182, 2006.

[45] N. Akopian, N. H. Lindner, E. Poem, Y. Berlatzky, J. Avron, D. Gershoni, B. D. Gerardot, and P. M. Petroff. Entangled photon pairs from semiconductor quantum dots. *Phys. Rev. Lett.*, 96(13):130501, 2006.

[46] A. Greilich, M. Schwab, T. Berstermann, T. Auer, R. Oulton, D. R. Yakovlev, M. Bayer, V. Stavarache, D. Reuter, and A. Wieck. Tailored quantum dots for entangled photon pair creation. *Phys. Rev. B*, 73(4):045323, 2006.

[47] B. D. Gerardot, S. Seidl, P. A. Dalgarno, R. J. Warburton, D. Granados, J. M. Garcia, K. Kowalik, O. Krebs, K. Karrai, A. Badolato, and P. M. Petroff. Manipulating exciton fine structure in quantum dots with a lateral electric field. *Appl. Phys. Lett.*, 90(4):041101, 2007.

[48] K. Kowalik, O. Krebs, A. Lemaître, B. Eble, A. Kudelski, P. Voisin, S. Seidl, and J. A. Gaj. Monitoring electrically driven cancellation of exciton fine structure in a semiconductor quantum dot by optical orientation. *Appl. Phys. Lett.*, 91(18):183104, 2007.

[49] M. M. Vogel, S. M. Ulrich, R. Hafenbrak, P. Michler, L. Wang, A. Rastelli, and O. G. Schmidt. Influence of lateral electric fields on multiexcitonic transitions and fine structure of single quantum dots. *Appl. Phys. Lett.*, 91(5):051904, 2007.

[50] R. Hafenbrak, S. M. Ulrich, P. Michler, L. Wang, A. Rastelli, and O. G. Schmidt. Triggered polarization-entangled photon pairs from a single quantum dot up to 30 K. *New J. Phys.*, 9(9):315, 2007.

[51] R. Hafenbrak, S. M. Ulrich, L. Wang, A. Rastelli, O. G. Schmidt, and P. Michler. Single entangled photon pair emission from an InGaAs/GaAs quantum dot up to temperatures of 30 K. *Phys. Status Solidi C*, 439:1–6, 2008.

[52] D. Bimberg, M. Grundmann, and N.N. Ledentsov. *Quantum Dot Heterostructures*. John Wiley and Sons, Inc., Chichester, 1999.

[53] P. Grangier, B. Sanders, and J. Vuckovic (editors). Focus on single photons on demand. *New J. Phys.*, 6:1367–2630, 2004.

[54] J. Volz, M. Weber, D. Schlenk, W. Rosenfeld, J. Vrana, K. Saucke, C. Kurtsiefer, and H. Weinfurter. Observation of entanglement of a single photon with a trapped atom. *Phys. Rev. Lett.*, 96:030404, 2006.

[55] J. Volz, M. Weber, D. Schlenk, W. Rosenfeld, C. Kurtsiefer, and H. Weinfurter. An atom and a photon. *Laser Phys.*, 17:1007–1016, 2007.

[56] M. Hijlkema, B. Weber, H. P. Specht, S. C. Webster, and A. Kuhn. A single-photon server with just one atom. *Nat. Phys.*, 3:253–255, 2007.

[57] W. Rosenfeld, F. Hocke, F. Henkel, M. Krug, J. Volz, M. Weber, and H. Weinfurter. Towards long-distance atom-photon entanglement. *Phys. Rev. Lett.*, 101(26):260403, 2008.

[58] C. Kittel. *Introduction to Solid State Physics.* Wiley, New York, 1996.

[59] P. Y. Yu and M. Cardona. *Fundamentals of Semiconductors.* Springer, Berlin, 2001.

[60] L. He, G. Bester, and A. Zunger. Strain-induced interfacial hole localization in self-assembled quantum dots: Compressive InAs/GaAs versus tensile InAs/InSb. *Phys. Rev. B*, 70(23):235316, 2004.

[61] M. Gong, K. Duan, C. Li, R. Magri, G. A. Narvaez, and L. He. Electronic structure of self-assembled InAs/InP quantum dots: Comparison with self-assembled InAs/GaAs quantum dots. *Phys. Rev. B*, 77:045326, 2008.

[62] A. Wojs, P. Hawrylak, S. Fafard, and L. Jacak. Electronic structure and magneto-optics of self-assembled quantum dots. *Phys. Rev. B*, 54(8):5604–5608, 1996.

[63] P. Hawrylak. Excitonic artificial atoms: Engineering optical properties of quantum dots. *Phys. Rev. B*, 60(8):5597–5608, 1999.

[64] M. Bayer, G. Ortner, O. Stern, A. Kuther, A. A. Gorbunov, A. Forchel, P. Hawrylak, S. Fafard, K. Hinzer, T. L. Reinecke, S. N. Walck, J. P. Reithmaier, F. Klopf, and F. Schäfer. Fine structure of neutral and charged excitons in self-assembled In(Ga)As/(Al)GaAs quantum dots. *Phys. Rev. B*, 65(19):195315, 2002.

[65] S. Raymond, S. Studenikin, A. Sachrajda, Z. Wasilewski, S. J. Cheng, W. Sheng, P. Hawrylak, A. Babinski, M. Potemski, G. Ortner, and M. Bayer. Excitonic energy shell structure of self-assembled InGaAs/GaAs quantum dots. *Phys. Rev. Lett.*, 92:187402, 2004.

[66] A. Babinski, M. Potemski, S. Raymond, J. Lapointe, and Z. R. Wasilewski. Emission from a highly excited single InAs-GaAs quantum dot in magnetic fields: An excitonic fock-darwin diagram. *Phys. Rev. B*, 74(15):155301, 2006.

[67] M. Korkusiński. *Correlations in semiconductor quantum dots.* PhD thesis, University of Ottawa, 2004.

[68] R. L. Williams, G. C. Aers, P. J. Poole, J. Lefebvre, D. Chithrani, and B. Lamontagne. Controlling the self-assembly of InAs/InP quantum dots. *J. Cyrstal Growth*, 223(3):321–331, 2001.

[69] J. H. Davies. *The Physics of Low-Dimensional Semiconductors.* Cambridge University Press, Cambridge, 1998.

[70] G. Bester, S. Nair, and A. Zunger. Pseudopotential calculation of the excitonic fine structure of million-atom self-assembled $In_{1-x}Ga_xAs$/GaAs quantum dots. *Phys. Rev. B*, 67(16):161306, 2003.

[71] L. G. C. Rego, P. Hawrylak, J. A. Brum, and A. Wojs. Interacting valence holes in p-type SiGe quantum disks in a magnetic field. *Phys. Rev. B*, 55(23):15694–15700, 1997.

[72] S. Cortez, O. Krebs, P. Voisin, and J. M. Gérard. Polarization of the interband optical dipole in InAs/GaAs self-organized quantum dots. *Phys. Rev. B*, 63(23):233306, 2001.

[73] W. Langbein, P. Borri, U. Woggon, V. Stavarache, D. Reuter, and A. D. Wieck. Control of fine-structure splitting and biexciton binding in $In_xGa_{1x}As$ quantum dots by annealing. *Phys. Rev. B*, 69(19):161301, 2004.

[74] E. Molinari U. Hohenester. Role of coulomb correlations in the optical spectra of semiconductor quantum dots. *Phys. Status Solidi B*, 221(1):19–24, 2000.

[75] G. A. Narvaez and P. Hawrylak. Effects of electron-electron interactions on excitonic absorption in charged self-assembled quantum dots. *Phys. Rev. B*, 61(20):13753–13762, 2000.

[76] M. Grundmann, J. Christen, N. N. Ledentsov, J. Böhrer, D. Bimberg, S. S. Ruvimov, P. Werner, U. Richter, U. Gösele, J. Heydenreich, V. M. Ustinov, A. Yu. Egorov, A. E. Zhukov, P. S. Kop'ev, and Zh. I. Alferov. Ultranarrow luminescence lines from single quantum dots. *Phys. Rev. Lett.*, 74(20):4043–4046, 1995.

[77] D. Gammon, E. S. Snow, B. V. Shanabrook, D. S. Katzer, and D. Park. Fine structure splitting in the optical spectra of single GaAs quantum dots. *Phys. Rev. Lett.*, 76(16):3005–3008, 1996.

[78] E. Dekel, D. Gershoni, E. Ehrenfreund, D. Spektor, J. M. Garcia, and P. M. Petroff. Multiexciton spectroscopy of a single self-assembled quantum dot. *Phys. Rev. Lett.*, 80(22):4991–4994, 1998.

[79] Y. Toda, S. Shinomori, K. Suzuki, and Y. Arakawa. Near-field magneto-optical spectroscopy of single self-assembled InAs quantum dots. *Appl. Phys. Lett.*, 73(4):517–519, 1998.

[80] M. Bayer, O. Stern, P. Hawrylak, S. Fafard, and A. Forchel. Ultranarrow luminescence lines from single quantum dots. *Nature (London)*, 405:923–926, 2000.

[81] F. Findeis, A. Zrenner, G. Böhm, and G. Abstreiter. Optical spectroscopy on a single InGaAs/GaAs quantum dot in the few-exciton limit. *Solid State Commun.*, 114(4):227 – 230, 2000.

[82] D. V. Regelman, E. Dekel, D. Gershoni, W. V. Schoenfeld, and P. M. Petroff. Dynamics of excitons in single semiconductor quantum dots probed by time-resolved optical spectroscopy. *Phys. Status Solidi B*, 224(2):343–348, 2001.

[83] D. Kim, J. Lefebvre, J. Lapointe, M. E. Reimer, J. Mckee, P. J. Poole, and R. L. Williams. Optical spectroscopy of single, planar, self-assembled InAs/InP quantum dots. *Phys. Status Solidi C*, 3(11):3840–3843, 2006.

[84] J. Singh. *Physics of Semiconductors and Their Heterostructures.* McGraw-Hill, New York, 1993.

[85] I. N. Stranski and L. Von Krastanow. *Abhandlungen der Mathematisch-Naturwissenschaftlichen Klasse. Akademie der Wissenschaften und der Literatur in Mainz*, 146:797, 1939.

[86] P. J. Poole, J. McCaffrey, R. L. Williams, J. Lefebvre, and D. Chithrani. Chemical beam epitaxy growth of self-assembled InAs/InP quantum dots. *J. Vac. Sci. Technol. B*, 19(4):1467–1470, 2001.

[87] P. J. Poole, R. L. Williams, J. Lefebvre, and S. Moisa. Using As/P exchange processes to modify InAs/InP quantum dots. *J. Cyrstal Growth*, 257(1-2):89–96, 2003.

[88] S. Frédérick. *Microcavity Designs for an InAs/InP Quantum Dot Fibre-Compatible Single Photon Source.* PhD thesis, University of Ottawa, 2008.

[89] S. Rodt, R. Heitz, A. Schliwa, R. L. Sellin, F. Guffarth, and D. Bimberg. Repulsive exciton-exciton interaction in quantum dots. *Phys. Rev. B*, 68(3):035331, 2003.

[90] D. Sarkar, H. P. van der Meulen, J. M. Calleja, J. M. Becker, R. J. Haug, and K. Pierz. Exciton fine structure and biexciton binding energy in single self-assembled InAs/AlAs quantum dots. *J. Appl. Phys.*, 100(2):023109, 2006.

[91] C. Dal Savio, K. Pierz, G. Ade, H. U. Danzebrink, E. O. Göbel, and A. Hangleiter. Optical study of single InAs on $In_{0.12}Ga_{0.88}As$ self-assembled quantum dots: biexciton binding energy dependence on the dots size. *Appl. Phys. B*, 84(1):317–322, 2006.

[92] J. J. Finley, A. D. Ashmore, A. Lemaître, D. J. Mowbray, M. S. Skolnick, I. E. Itskevich, P. A. Maksym, M. Hopkinson, and T. F. Krauss. Charged and neutral exciton complexes in individual self-assembled $In(Ga)As$ quantum dots. *Phys. Rev. B*, 63(7):073307, 2001.

[93] Q. Wu, R. D. Grober, D. Gammon, and D. S. Katzer. Excitons, biexcitons, and electron-hole plasma in a narrow 2.8-nm $GaAs/Al_xGa_{1-x}As$ quantum well. *Phys. Rev. B*, 62(19):13022–13027, 2000.

[94] G. Bacher, R. Weigand, J. Seufert, V. D. Kulakovskii, N. A. Gippius, A. Forchel, K. Leonardi, and D. Hommel. Biexciton versus exciton lifetime in a single semiconductor quantum dot. *Phys. Rev. Lett.*, 83(21):4417–4420, 1999.

[95] M. Wimmer, S. V. Nair, and J. Shumway. Biexciton recombination rates in self-assembled quantum dots. *Phys. Rev. B*, 73(16):165305, 2006.

[96] K. Brunner, G. Abstreiter, G. Böhm, G. Tränkle, and G. Weimann. Sharp-line photoluminescence and two-photon absorption of zero-dimensional biexcitons in a GaAs/AlGaAs structure. *Phys. Rev. Lett.*, 73(8):1138–1141, 1994.

[97] H. Kamada, H. Ando, J. Temmyo, and T. Tamamura. Excited-state optical transitions of excitons and biexcitons in a single $In_xGa_{1-x}As$ quantum disk. *Phys. Rev. B*, 58(24):16243–16251, 1998.

[98] S. Ritter, P. Gartner, N. Baer, and F. Jahnke. Anomalous stark effect in semiconductor quantum dots. *Phys. Rev. B*, 76:165302, 2007.

[99] C. Pryor. Quantum wires formed from coupled InAs/GaAs strained quantum dots. *Phys. Rev. Lett.*, 80(16):3579–3581, 1998.

[100] M. Korkusiński and P. Hawrylak. Electronic structure of vertically stacked self-assembled quantum disks. *Phys. Rev. B*, 63(19):195311, 2001.

[101] P. W. Fry, I. E. Itskevich, D. J. Mowbray, M. S. Skolnick, J. J. Finley, J. A. Barker, E. P. O'Reilly, L. R. Wilson, I. A. Larkin, P. A. Maksym, M. Hopkinson, M. Al-Khafaji, J. P. R. David, A. G. Cullis, G. Hill, and J. C. Clark. Inverted electron-hole alignment in InAs-GaAs self-assembled quantum dots. *Phys. Rev. Lett.*, 84:733–736, 2000.

[102] J. Seufert, M. Obert, M. Scheibner, N. A. Gippius, G. Bacher, A. Forchel, T. Passow, K. Leonardi, and D. Hommel. Stark effect and polarizability in a single CdSe/ZnSe quantum dot. *Appl. Phys. Lett.*, 79(7):1033–1035, 2001.

[103] E. S. Moskalenko, M. Larsson, W. V. Schoenfeld, P. M. Petroff, and P. O. Holtz. Carrier transport in self-organized InAs/GaAs quantum-dot structures studied by single-dot spectroscopy. *Phys. Rev. B*, 73(15):155336, 2006.

[104] A. K. Ekert. Quantum cryptography based on bell's theorem. *Phys. Rev. Lett.*, 67(6):661–663, 1991.

[105] N. Gisin, G. Ribordy, W. Tittel, and H. Zbinden. Quantum cryptography. *Rev. Mod. Phys.*, 74(1):145–195, 2002.

[106] N. Gisin and R. Thew. Quantum communication. *Nat. Photonics*, 1:165–171, 2007.

[107] R. Ursin, F. Tiefenbacher, T. Schmitt-Manderbach, H. Weier, T. Scheidl, M. Lindenthal, B. Blauensteiner, T. Jennewein, J. Perdigues, P. Trojek, B. Omer, M. Furst, M. Meyenburg, J. Rarity, Z. Sodnik, C. Barbieri, H. Weinfurter, and A. Zeilinger. Entanglement-based quantum communication over 144 km. *Nat. Phys.*, 3:481–486, 2007.

[108] E. Knill, R. Laflamme, and G. J. Milburn. A scheme for efficient quantum computation with linear optics. *Nature (London)*, 409:46–52, 2001.

[109] C. H. Bennett, G. Brassard, C. Crépeau, R. Jozsa, A. Peres, and W. K. Wootters. Teleporting an unknown quantum state via dual classical and Einstein-Podolsky-Rosen channels. *Phys. Rev. Lett.*, 70(13):1895–1899, 1993.

[110] P. G. Kwiat, K. Mattle, H. Weinfurter, A. Zeilinger, A. V. Sergienko, and Y. Shih. New high-intensity source of polarization-entangled photon pairs. *Phys. Rev. Lett.*, 75(24):4337–4341, 1995.

[111] E. Moreau, I. Robert, L. Manin, V. Thierry-Mieg, J. M. Gérard, and I. Abram. Quantum cascade of photons in semiconductor quantum dots. *Phys. Rev. Lett.*, 87(18):183601, 2001.

[112] O. Benson, C. Santori, M. Pelton, and Y. Yamamoto. Regulated and entangled photons from a single quantum dot. *Phys. Rev. Lett.*, 84(11):2513–2516, 2000.

[113] R. J. Young, R. M. Stevenson, P. Atkinson, K. Cooper, D. A. Ritchie, and A. J. Shields. Improved fidelity of triggered entangled photons from single quantum dots. *New J. Phys.*, 8(2):29, 2006.

[114] S. Rodt, A. Schliwa, K. Pötschke, F. Guffarth, and D. Bimberg. Correlation of structural and few-particle properties of self-organized InAs/GaAs quantum dots. *Phys. Rev. B*, 71(15):155325, 2005.

[115] R. Seguin, A. Schliwa, S. Rodt, K. Pötschke, U. W. Pohl, and D. Bimberg. Size-dependent fine-structure splitting in self-organized InAs/GaAs quantum dots. *Phys. Rev. Lett.*, 95(25):257402, 2005.

[116] N. Chauvin, B. Salem, G. Bremond, G. Guillot, C. Bru-Chevallier, and M. Gendry. Size and shape effects on excitons and biexcitons in single InAs/InP quantum dots. *J. Appl. Phys.*, 100(7):073702, 2006.

[117] O. Stier, R. Heitz, A. Schliwa, and D. Bimberg. Shape and composition effects on excitons and biexcitons in quantum dots. *Phys. Status Solidi A*, 190:477–484, 2002.

[118] J. E. Avron, G. Bisker, D. Gershoni, N. H. Lindner, E. A. Meirom, and R. J. Warburton. Entanglement on demand through time reordering. *Phys. Rev. Lett.*, 100(12):120501, 2008.

[119] G. Pfanner, M. Seliger, and U. Hohenester. Entangled photon sources based on semiconductor quantum dots: The role of pure dephasing. *Phys. Rev. B*, 78(19):195410, 2008.

[120] V. Stavarache, D. Reuter, A. D. Wieck, M. Schwab, D. R. Yakovlev, R. Oulton, and M. Bayer. Control of quantum dot excitons by lateral electric fields. *Appl. Phys. Lett.*, 89(12):123105, 2006.

[121] E. Tsitsishvili. Fine structure of exciton levels in strained quantum dots. *Phys. Status Solidi B*, 228(3):671–683, 2001.

[122] V. Cerletti, W. A. Coish, O. Gywat, and D. Loss. Recipes for spin-based quantum computing. *Nanotechnology*, 16(4):R27–R49, 2005.

[123] D. Loss and D. P. DiVincenzo. Quantum computation with quantum dots. *Phys. Rev. A*, 57(1):120–126, 1998.

[124] M. Kroutvar, Y. Ducommun, D. Heiss, M. Bichler, D. Schuh, G. Abstreiter, and J. J. Finley. Optically programmable electron spin memory using semiconductor quantum dots. *Nature (London)*, 432:81–84, 2004.

[125] J. R. Petta, A. C. Johnson, J. M. Taylor, E. A. Laird, A. Yacoby, M. D. Lukin, C. M. Marcus, M. P. Hanson, and A. C. Gossard. Coherent Manipulation of Coupled Electron Spins in Semiconductor Quantum Dots. *Science*, 309(5744):2180–2184, 2005.

[126] F. H. L. Koppens, C. Buizert, K. J. Tielrooi, I. T. Vink, K. C. Nowack, T. Meunier, L. P. Kouwenhoven, and L. M. K. Vandersypen. Driven coherent oscillations of a single electron spin in a quantum dot. *Nature (London)*, 442:766, 2006.

[127] K. C. Nowack, F. H. L. Koppens, Yu. V. Nazarov, and L. M. K. Vandersypen. Coherent Control of a Single Electron Spin with Electric Fields. *Science*, 318(5855):1430–1433, 2007.

[128] A. J. Ramsay, S. J. Boyle, R. S. Kolodka, J. B. B. Oliveira, J. Skiba-Szymanska, H. Y. Liu, M. Hopkinson, A. M. Fox, and M. S. Skolnick. Fast optical preparation, control, and readout of a single quantum dot spin. *Phys. Rev. Lett.*, 100(19):197401, 2008.

[129] D. Heiss, V. Jovanov, M. Bichler, G. Abstreiter, and J. J. Finley. Charge and spin readout scheme for single self-assembled quantum dots. *Phys. Rev. B*, 77(23):235442, 2008.

[130] F. Jelezko, T. Gaebel, I. Popa, M. Domhan, A. Gruber, and J. Wrachtrup. Observation of coherent oscillation of a single nuclear spin and realization of a two-qubit conditional quantum gate. *Phys. Rev. Lett.*, 93(13):130501, 2004.

[131] C. Dion, P. Desjardins, N. Shtinkov, M. D. Robertson, F. Schiettekatte, P. J. Poole, and S. Raymond. Intermixing during growth of InAs self-assembled quantum dots in InP: A photoluminescence and tight-binding investigation. *Phys. Rev. B*, 77(7):075338, 2008.

[132] M. Borgström, L. Samuelson, W. Seifert, A. Mikkelsen, L. Ouattara, and E. Lundgren. Spontaneous InAs quantum dot nucleation at strained InP/GaInAs interfaces. *Appl. Phys. Lett.*, 83(23):4830–4832, 2003.

[133] J. J. Finley, M. Sabathil, P. Vogl, G. Abstreiter, R. Oulton, A. I. Tartakovskii, D. J. Mowbray, M. S. Skolnick, S. L. Liew, A. G. Cullis, and M. Hopkinson. Quantum-confined stark shifts of charged exciton complexes in quantum dots. *Phys. Rev. B*, 70(20):201308, 2004.

[134] J. A. Barker and E. P. O'Reilly. Theoretical analysis of electron-hole alignment in InAs-GaAs quantum dots. *Phys. Rev. B*, 61(20):13840–13851, 2000.

[135] M. D. Robertson, J. C. Bennett, A. M. Webb, J. M. Corbett, S. Raymond, and P. J. Poole. The determination of the size and shape of buried InAs/InP quantum dots by transmission electron microscopy. *Ultramicroscopy*, 103:205–219, 2005.

[136] M. Borgström, L. Samuelson, W. Seifert, A. Mikkelsen, L. Ouattara, and E. Lundgren. Spontaneous InAs quantum dot nucleation at strained InP/GaInAs interfaces. *Appl. Phys. Lett.*, 83:4830–4832, 2003.

[137] M. Grundmann, O. Stier, and D. Bimberg. InAs/GaAs pyramidal quantum dots: Strain distribution, optical phonons, and electronic structure. *Phys. Rev. B*, 52(16):11969–11981, 1995.